UNIVERSITY OF CALIFORNIA SAN DIEGO

Engineering of *Ex Vivo* Tissue Models Towards Enabling Point-of-Care Functional Oncology

A dissertation submitted in partial satisfaction of the requirements for the degree Doctor of Philosophy

in

Doctor of Philosophy in Bioengineering

by

Michael Hu

Committee in Charge:

Professor Prashant Mali, Chair
Professor David Cheresh
Professor Adam Engler
Professor Esther Kwon
Professor Yingxiao Wang

2022

The dissertation of Michael Hu is approved, and it is acceptable in quality and form for publication on microfilm and electronically.

University of California San Diego

2022

DEDICATION

To – Jessica, Cooper, and Charlie – who supported me as I began the work that culminated in this manuscript, and to – Emily – who supported me as I brought that work to a close.

To – Nancy – who stood by my side and encouraged me to continue during the moments that I struggled the most.

To – Krystal – who dedicated her time and effort, both inside and outside of the lab to making my work possible.

To – Linda – who committed herself to my vision and worked tirelessly to help me achieve it; who provided me with unwavering support, both physical and mental, even when she herself felt overwhelmed; who always did more than what was asked of her.

TABLE OF CONTENTS

LIST OF ABBREVIATIONS

AFM: Atomic Force Microscopy

BSA: Bovine Serum Albumin

CCK8: Cell-Counting-Kit 8

CRISPR: Clustered Regularly Interspaced Short Palindromic Repeats

CRISPRko: CRISPR Knockout

DMEM: Dulbecco's Modified Eagle Medium

DNA: Deoxyribonucleic Acid

ECM: Extracellular Matrix

EGM-2: Endothelial Growth Media 2

FBS: Fetal Bovine Serum

FDR: False-Discovery Rate

GelMA: Gelatin Methacryloyl

GFP: Green Fluorescent Protein

gRNA : Guide RNA

HA: Hyaluronic Acid

hESC: Human Embryonic Stem Cell

hMSC: Human Mesenchymal Stem Cell

HUVEC: Human Umbilical Vein Endothelial Cell

iPSC: Induced Pluripotent Stem Cell

LFC: Log_2Fold Change

MEM: Minimum Essential Media

MOI: Multiplicity of Infection

NC: NeuroCult Medium

NSG: NOD-SCID Gamma

OCT: Optimal Cutting Temperature Compound

PBS: Phosphate Buffered Saline

PCR: Polymerase Chain Reaction

PDX: Patient-Derived Xenograft

PEG: Poly(Ethylene Glycol)

PEGDA: Poly(Ethylene Glycol) Diacrylate

PLA: Poly(Lactic Acid)

PVA: Poly(Vinyl Alcohol)

RNA: Ribonucleic Acid

sgRNA: Single Guide RNA

SOC: Super Optimal Broth with Catabolite Repression

LIST OF FIGURES

LIST OF TABLES

ACKNOWLEDGEMENTS

I would like to acknowledge Professor Prashant Mali for his support both as my advisor and as the chair of my committee. He has guided me through over half a decade of research work, and I would not have accomplished half of what I have managed without his support.

I would also like to acknowledge both Professor Adam Engler and Professor Robert Wechsler-Reya, whose labs provided resources that made key portions of my work possible.

The Introduction contains excerpts of material from Advances in CRISPR-Cas Based Genome Engineering as it appears in Current Opinion in Biomedical Engineering Volume 1, 2017. I, as the dissertation author, was one of two primary co-authors of this paper, with the full authors list being: Dhruva Katrekar, Michael Hu, and Prashant Mali.

Chapter 1, in full, is material that appears in Facile Engineering of Long-Term Culturable Ex Vivo Vascularized Tissues Using Biologically Derived Matrices as it appears in Advanced Healthcare Materials Volume 7, 2018. I, as the dissertation author, was the primary author of this paper, with the full authors list being: Michael Hu, Amir Dailamy, Xin Yi Lei, Udit Parekh, Daniella McDonald, Aditya Kumar, and Prashant Mali.

Chapters 2 and 3, in full, are material that appears in Integrated genome and tissue engineering enables screening of cancer vulnerabilities in physiologically relevant perfusable ex vivo cultures as it appears in Biomaterials Volume 280, 2022. I, as the dissertation author, was the primary author of this paper, with the full authors list being: Michael Hu, Xin Yi Lei, Jon Larson, Melissa McAlonis, Kyle Ford, Daniella McDonald, Krystal Mach, Jessica Rusert, Robert Wechsler-Reya, and Prashant Mali.

Chapter 4, in part, is currently being prepared for submission for publication of the material. I, as the dissertation author, am one of three primary authors of this work, with the full authors list being: Michael Hu, Daniella McDonald, and Prashant Mali.

VITA

2015	Systems Engineer, Fresenius Kabi
2016	Bachelor of Science, Northwestern University
2017 – 2018	Teaching Assistant, University of California San Diego
2017 – 2020	National Heart Lung and Blood Institute Predoctoral Fellow
2020	Masters of Science, University of California San Diego
2022	Doctor of Philosophy, University of California San Diego

Publications

Hu, M., Lei, X.Y., Larson, J.D., McAlonis, M., Ford, K., McDonald, D., Mach, K., Rusert, J., Wechsler-Reya, R., Mali, P., 2022. Integrated genome and tissue engineering enables screening of cancer vulnerabilities in physiologically relevant perfusable ex vivo cultures. *Biomaterials* 280, 121276.

Moreno, A.M., Alemán, F., Catroli, G.F., Hunt, M., **Hu, M.**, Dailamy, A., Pla, A., Woller, S., Palmer, N., Parekh, U., McDonald, D., Roberts, A., Goodwill, V., Dryden, I., Hevner, R., Delay, L., Goncalves dos Santos, G., Yaksh, T., Mali, P., 2021. Long-lasting analgesia via targeted in situ repression of Nav1.7 in mice. *Sci. Transl. Med.* 13, eaay9056.

McDonald, D., Wu, Y., Dailamy, A., Tat, J., Parekh, U., Zhao, D., **Hu, M.**, Tipps, A., Zhang, K., Mali, P., 2020. Defining the Teratoma as a Model for Multi-lineage Human Development. *Cell* 183, 1402-1419.e18.

Hu, M., Dailamy, A., Lei, X.Y., Parekh, U., McDonald, D., Kumar, A., Mali, P., 2018. Facile Engineering of Long-Term Culturable Ex Vivo Vascularized Tissues Using Biologically Derived Matrices. *Adv. Healthcare Mater.* 7, 1800845.

Yeh, C., **Hu, M**., Shull, K., 2018. Oxygen Inhibition of Radical Polymerizations Investigated with the QCM. *Macromolecules*, 51.

Katrekar, D., **Hu, M**., Mali, P., 2017. Advances in CRISPR-Cas based genome engineering. *Curr. Op. in Biomed. Eng*. 1, 78–86.

Fields of Study

Major Field: Bioengineering

Professor Prashant Mali

ABSTRACT OF THE DISSERTATION

Engineering of *Ex Vivo* Tissue Models Towards Enabling Point-of-Care Functional Oncology

by

Michael Hu

Doctor of Philosophy in Bioengineering

University of California San Diego, 2022

Professor Prashant Mali, Chair

Abstract

A fundamental issue in cancer therapeutics that has inhibited treatment progress is the lack of patient-specific models for both discovery and evaluation. Recent advances in sequencing technologies and molecular biology have enabled personalized treatment plans for patients guided by molecular profiling. However, success has been limited by the lack of phenotypic validations of genotype-sourced data. The development of CRISPR screening technologies offers a means of simultaneously identifying and functionally validating potential therapeutic targets to address this, but screens have largely been conducted in 2D cell culture conditions, with applications in more complex models being minimal thus far. As such, we focused on using tissue engineering technologies to construct a more physiologically accurate model, then integrating it with CRISPR

screening technologies to enable cancer screening and validation in physiologically relevant systems. We began by developing a 3D-printing technique to engineer tissue constructs from biologically-derived materials and an evacuable poly(vinyl alcohol) (PVA) vascular scaffold. The result was a perfusable tissue construct that could be sustained *ex vivo* while enabling recapitulation of biological tumors and organs. We then further optimized the system to enable perfusion at physiological flow rates to achieve dense cultures of breast cancer cells, and then successfully applied a large-scale CRISPR screen, the first in a perfused tissue model. Utility of the model was explored further by tuning it to allow for the culture of patient-derived xenograft (PDX) cells, followed by thorough characterization and integration with a CRISPR knockout library containing only therapeutically-actionable drug targets to emulate a point-of-care diagnostics scenario. Results indicated that our engineered systems better represented *in vivo* biology compared to existing models, and also showed greater reproducibility than PDX mouse models of cancer. Understanding the clear importance of the material environment, we then proceeded to apply this knowledge towards organotypic engineering in a teratoma context, using specific material blends to promote differentiation of pluripotent stem cells towards certain lineages during teratoma development. Overall, our body of work and results highlight the importance and applicability of a multidisciplinary approach, with the integration of tissue and genetic engineering yielding greater avenues for biological discovery.

Introduction

Presently, the deaths of one in seven people globally can be attributed to cancer[1], and there are over 16.9 million living Americans with a history of the disease[2], resulting in an estimated economic burden of over $94 billion[3]. One of the fundamental problems accompanying this issue is the difficulty of identifying viable therapeutics. Beyond pipeline issues such as the low rate of translational success for oncology drugs to begin with[4], advances in genomics technologies has revealed that the nature of cancer varies widely across patients[5–7]. As such, there has been a recent push to shift from the classical drug-to-disease model to more personalized approaches, where individual treatments are chosen on a patient-by-patient basis based on predicted responsiveness[8,9], with a particular focus on the use of next-generation sequencing technologies.

To date, several clinical trials have been conducted in which targeted sequencing, whole exome-sequencing, transcriptomic profiling, or other similar techniques have been applied to obtain patient-specific molecular profiles on which an actionable therapeutic target can be identified[10–15]. However, results so far indicate that in non-randomized trials, relatively low proportions of patients showed responsiveness to the personalized treatments[10–12,15], and in a randomized trial, patients provided with a precision-guided treatment plan showed no significant difference in outcome compared to controls[13]. While a variety of potential causes have been proposed, one particularly significant factor could be that genotype data alone is insufficient to reliably choose a treatment, and as such, reliable functional validations are needed[16–19].

The need for functional validation models in cancer therapeutics is a well-understood problem, and significant work has gone into developing new approaches to

address these issues over the last decade. In particular, CRISPR-Cas9 technologies have become relevant due to advances in DNA sequencing techniques that, when coupled with array based synthesis technologies, have enabled generation of large pools of gRNA libraries that can be used to conduct large-scale knockout screens. This allows for perturbation and phenotypic analysis of thousands of genes simultaneously, allowing not only for functional validations, but also for discovery of potential targets, particularly in the case of cancer[20–30]. For instance, genome scale CRISPR-Cas9 libraries have enabled high-throughput screening of cancer cells to identify genes that confer drug resistance[31], as well as genes that are essential for cellular function[32]. Beyond that, researchers have characterized the role of p53 and ERα-bound enhancers in their native context by making use of a gRNA pool targeting their respective binding sites in enhancer regions[33], further expanding the applicability of Cas9 to non-coding genome sequences.

Despite its potential though, application of CRISPR screening technologies in a personalized medicine context would come with many challenges. Many CRISPR screens have been conducted in 2D monolayer culture[20,24,27,28,34–36], as well as in animal models[37–40]. However, accurate identification and functional validation of personalized therapeutic targets would require the use of patient-derived tissue, of which only an extremely small amount would be available from a biopsy. Traditional 2D monolayer culture would be extremely difficult, typically requiring conditional reprogramming[17], and resulting in selective pressures and loss of many phenotypic properties[41]. Xenograft mouse models offer a more physiologically accurate alternative, but significant differences still exist between human and animal models at the genetic, molecular, and cellular level[42,43], and engrafted tumors often require a multi-month growth period[17,44,45],

which in the specific case of a clinical setting, is non-viable. These issues are well-understood, and as such, there has been a recent push to enable CRISPR screening in 3D systems to account for behavioral differences in a more biologically accurate environment[29,30,46,47].

To this end, efforts have been made over the last several decades to develop 3D *in vitro* models of cell culture, with hopes that they will better mimic human biology[48]. The simplest model of 3D cell culture is growth in a biocompatible 3-dimensional matrix. A large assortment of biomaterials have been developed and characterized for this purpose, both natural and synthetic. Natural materials include biologically-sourced polymers such as collagen, fibrin, and hyaluronan, along with plant-derived components such as alginate and cellulose, and a number of commercially available extracellular matrix (ECM) products such as lrECM and Matrigel[49]. Synthetic materials are generally biocompatible polymers such as polypeptides, poly(lactic acid) (PLA), poly(lactic-co-glycolytic acid), poly(ethylene glycol), and an assortment of functionalized variants[50]. While this approach is an extremely straightforward method to introduce a 3D environment, it is highly limited in scale due to nutrient diffusion limitations[51] and the lack of vascularization. For this reason, the various biomaterials that have been developed have been incorporated into more complex methods of 3D culture.

One of these is the use of organoid technologies, which offers a more advanced method of recapitulating the 3D cell microenvironment. Classical organoid formation typically requires differentiating stem cells down a specific lineage, and subsequently allowing for self-organization into an organ-like structure. Through this method, many groups have generated facsimiles of various tissues including gut, brain, kidney, and liver.

Moreover, these organoids often recapitulate many organ-specific functions[52–56]. For instance, growth of intestinal stem cells in Matrigel yielded self-organized intestinal organoids able to be transplanted into mice[53], and growth of liver progenitor cells in Matrigel resulted in liver organoids exhibiting biliary ductal identities[57]. Further refinement of organoid culturing techniques have allowed researchers to develop cancer tissue-specific organoids, often recapitulating many phenotypes of the original tissue[44,58–62]. Despite this, in the context of therapeutic discovery and validation, organoids encounter the same problem of scale, which limits analytical throughput, as well as lack of controlled spatial ordering, and inability to easily co-culture[54–56].

Another method is the use of organ-on-a-chip technologies, which combine biomaterials with microfabrication technologies to generate microfluidic systems capable of supporting a variety of cell and organoid cultures. Tissue types modeled using these devices include liver, lung, cancer, brain, gut, heart, and blood vessels among others[63,64]. Moreover, increased complexity can be introduced by linking multiple organ-on-a-chip platforms to mimic the interactions between *in vivo* tissues[63]. However, while the microfluidic nature of this system addresses the need for active flow, the platform is limited in scale entirely by design, and its complex technical nature restricts it to low-throughput applications[65,66]. Furthermore, while biological materials can be introduced into such systems[67], the environment is largely composed of synthetic polymers.

The last method for discussion is 3D bioprinting, in which biologically active 3D structures are fabricated through layer-by-layer deposition. Because the devices used for bioprinting are able to print with microscale resolutions, it is possible to pattern multiple cell types or materials, and construct tissue environments with extremely high spatial

precision[68,69]. Furthermore, this spatial control enables the introduction of vasculature within the printed structures[68,70–73]. In spite of this, there are a number of distinct limitations of the methodology. In order to be extruded from most 3D bioprinters, a material typically needs to possess shear-thinning properties as well as a certain degree of mechanical stability during the process. These compatibility requirements have limited most published studies to a very narrow range of materials[68,69]. Moreover, the 3D printing process itself is significantly more complex than the other methods described thus far, both in terms of equipment needs, and the imaging and setup needed to guide the design of the bioprinted tissue, providing a barrier of entry for many non-specialized researchers.

Thus, with the existing state of 3D-cell culture in mind, we made it our goal to engineer and thoroughly characterize an *ex vivo* tissue model that addressed the existing shortcomings. We then proceeded to optimize the system for use in conjunction with genetic screening technologies as well as patient-derived xenograft (PDX) models, thereby enabling physiologically relevant studies to be conducted, and providing a proof-of-concept for use in a point-of-care patient-specific treatment scenario.

Acknowledgements

The Introduction contains excerpts of material from Advances in CRISPR-Cas Based Genome Engineering as it appears in Current Opinion in Biomedical Engineering Volume 1, 2017. I, as the dissertation author, was one of two primary co-authors of this paper, with the full authors list being: Dhruva Katrekar, Michael Hu, and Prashant Mali.

Chapter 1: Engineering Long-Term Culturable Ex Vivo Vascularized Tissues from Biologically-Derived Matrices

1.1 Abstract

Recent advances in tissue engineering and 3D bioprinting have enabled construction of cell-laden scaffolds and matrix constructs containing perfusable vascular networks. Although these methods partially address the traditional nutrient-diffusion limitations present in engineered tissues, they are still restricted in both the viable vascular geometries they produce, and the spectrum of matrix materials they are compatible with. To address this, we engineered tissue constructs via 3D printing evacuable scaffolds of free-standing poly(vinyl alcohol) (PVA) coupled with incorporation of biologically derived matrices. The ease of printability combined with the biocompatible and water-soluble nature of PVA, allowed for easily repeatable generation of complex vascular patterns. Additionally, we also optimized compatibility with highly biologically relevant matrix materials including Matrigel, which were thus far not readily usable in bioprinted constructs. Here, we confirm the ability of this approach to produce long-term (>8 weeks) perfusable vascular networks, capable of simultaneously sustaining cocultures of multiple cell types. We further demonstrate the ability of the approach to generate vascularized matrices capable of sustaining excised tumor fragments *ex vivo* over multiple weeks, and to produce hybrid patterns allowing for proximal co-culture of vasculature and epithelial cell-lined lumens in close proximity, thereby enabling *ex vivo* recapitulation of gut-like systems. Taken together, the methodology is versatile with broad applicability, and importantly simple to use, enabling ready applicability in many research

settings. We believe this technique has the potential to significantly accelerate progress in engineering and study of *ex vivo* organotypic tissue constructs.

1.2 Introduction

Engineered tissue constructs have historically been promoted as a potential source of organ and tissue transplants[74,75]. More recently, there has also been increased exploration in non-clinical applications, such as elucidating mechanisms of cell-cell and cell-matrix interactions[76], modeling disease pathologies[77], and accelerating drug discovery and screening[78,79]. Regardless of the intended use however, the construction and applicability of engineered tissues is limited by scaling, as nutrient diffusion limitations caused by the lack of vascularization restricts tissue survival to thicknesses on the scale of a few hundred micrometers[80].

Much effort has gone into addressing this diffusion limitation, and among the various techniques used, 3D printing has experienced significant success, due to the precise spatial control it grants during the fabrication process, along with ease of use and ability to rapidly modify geometries to enable on-demand fabrication[68,75,81]. Many variants of the technique involve deposition of cell-laden hydrogels in specific patterns[81–89] using natural materials such as alginate[83–85,87,89], gelatin[82,83,87,88], hyaluronic acid[88], and decellularized ECM[83,90], as well as synthetic polymers that include PCL[86], PLCL[86], and PEG[81,87,88] among others. The result is cellularized lattices, which may or may not be vascularized, but possess high surface area to volume ratios to increase nutrient accessibility. An alternative approach is the formation of a perfusable cellularized construct by using an evacuable fugitive ink to produce a vascular channel within a

polymerized matrix[71–73,83]. Variants of this technique have been achieved using inks composed of materials such as Pluronics F127[71], gelatin[72], and carbohydrate glass[73], with matrices composed of various biocompatible materials, including gelatin, fibrin, collagen, and alginate. However, their use in generating vascular geometries more complex than 2D patterns or simple 3D grids has not been well-explored[71–73]. In addition, because of their material properties, most fugitive inks are compatible with only a small selection of matrix materials. For instance, Pluronics F127 solutions liquify at low temperatures[91,92], making them difficult to use with materials such as collagen and Matrigel that require such temperatures when casting. Similarly, gelatin inks are incompatible with transglutaminase, a cross-linking enzyme commonly used to generate scaffolds from materials including collagen, gelatin, hyaluronic acid, and albumin[93–96].

Here in this first chapter, we present a methodology of generating biologically-derived tissue constructs containing vascular channels of complex 3D geometries via 3D printing of poly(vinyl alcohol) (PVA). PVA is known to be biocompatible[97–99], and is usable with several deposition techniques, including selective laser sintering and fused filament printing[100–102]. In the context of cell culture, it has been used primarily as a matrix component to form porous, cell-laden hydrogels[103,104], or to form biocompatible hydrogels via stereolithography[97,100]. More recently, PVA has also been applied as an evacuable scaffold to generate vascularized matrices, though material-compatibility has been limited thus far to gelatin[98,99]. By utilizing the water-solubility of PVA with its ability to be printed into a variety of free-standing geometries, we expanded upon its usability by encapsulating it within and evacuating it from a wide range of systematically optimized biologically derived matrices to produce complex perfused tissue structures. Notably, the

methodology is both highly simple and easily reproducible, thereby making it accessible in many research settings. As such, the technique has the potential to significantly accelerate progress in tissue engineering.

1.3 Methods

1.3.1 Printing Methodology

1.3.1.1 3D Printing of Silicone Holders and Pump Setup

Long-term perfusion of the tissue constructs was achieved using a 3-component system consisting of a media reservoir, a flow-chamber, and a peristaltic pump (Watson Marlow 205U), all connected via silicone tubing (McMaster Carr ⅛ OD Platinum 2000 Silicone). Flow-chambers were constructed via extrusion-printing of silicone (Dow Corning Toray Sylgard SE1700) on glass, and contained inlet and outlet ports leading to the pump and media reservoirs[71].

1.3.1.2 3D Printing of Free-Standing PVA Structures

All geometries of interest were designed in Autodesk Inventor and exported to the Ultimaker Cura software. Structures were then printed using the Ultimaker^3 with a 0.4 mm printhead at speeds between 10 – 35 mm/s. PVA deposited was obtained directly from Ultimaker as a 2.85 mm diameter solid-state filament with a 3860 MPa tensile modulus and a density of 1.23 g/cm^3. Prior to use, PVA structures were sterilized via UV radiation.

1.3.1.3 Generating 3D Vascularized Constructs

A detailed example of the process is described in Appendix 1.7.2. Briefly, stock solutions of all materials were prepared prior to matrix formulation. Type A porcine skin gelatin (Sigma-Aldrich) was added to water (15 wt/vol%), dissolved overnight at 70 °C, brought to a pH of 7.4 using NaOH solution, and passed through a 0.22 um filter (Millipore). Solutions were stored long-term at 4 °C, and warmed to 37 °C prior to use. $CaCl_2$ (250 mM) was prepared as a stock solution in dPBS and stored at room-temperature. Thrombin (Sigma-Aldrich) was prepared as a stock solution (500 U/mL), aliquoted, stored at -20 °C, and warmed to 4 °C prior to use[71]. Matrigel (Corning) was purchased and had reported protein concentrations between 8 - 11 mg/mL. Solutions of both bovine plasma fibrinogen (Millipore) and transglutaminase (MooGloo) were prepared immediately before use by dissolving in 37 °C dPBS at respective concentrations of 100 mg/mL and 50 mg/mL.

Production of vascularized constructs required inserting a PVA-printed structure into the silicone holders with direct contact points at the inlet and outlet, then encapsulating within the formulated matrix. Matrices composed of Matrigel and fibrin were formulated using Matrigel (5 mg/mL), fibrinogen (10 mg/mL), transglutaminase (2 mg/mL), $CaCl_2$ (2.5 mM), and thrombin (2 U/mL), with remaining volume composed of cell-containing media. Matrices composed of Matrigel, gelatin, and fibrin were formulated from gelatin (1.5 wt%/mL), Matrigel (4 mg/mL), and all other components identical to those above. In either case, all components save Matrigel and thrombin were mixed at 37 °C and allowed to incubate for 30 minutes, after which both Matrigel and thrombin were rapidly added. The solution was mixed well, then poured into the silicone holders, and

allowed to gelate at 37 °C. Gelation occurred over 1 and 2.5 hours respectively for matrices with and without gelatin. Following gelation, PVA was evacuated via perfusion of warm media (**Figure 1.1B**), and the construct was perfused with media at approximately 10 - 12 rpm. After several hours of perfusion, human umbilical vein endothelial cells (HUVECs) were resuspended at a concentration of 10 x 10^6 cells/mL and injected into the vascular channel. Constructs were incubated for 30 minutes on either side, then left overnight without flow to allow for HUVEC adhesion. Flow was then reintroduced to remove non-adhering HUVECs from the channel.

Introduction of dense vascular beds within the constructs largely used the same procedure. However, prior to encapsulation, PVA thread (Solvron, Nitivy Co. 62T Type SS) was wrapped around the PVA scaffold (**Figure 1.1E**) and heat-sealed using a standard cauterizing pen.

1.3.2 Cell Culture

HUVECs and human mesenchymal stem cells (hMSCs) used in the study were obtained from Lonza, and were used until passages 12 and 10 respectively. HUVECs were cultured in either EGM-2 (Lonza) or EndoGRO-LS (Millipore), while hMSCs were cultured in MSCGM (Lonza) or MSCEM (Millipore). MDA-MB-231, MCF7, and Caco-2 cells were obtained from ATCC, and were respectively cultured in DMEM supplemented with 10% FBS and 2 mM L-Glutamine and EMEM (ATCC) supplemented with 20% FBS.

1.3.3 Animal Work

To generate tumors, GFP-transduced MDA-MB-231 cells were injected subcutaneously into the dorsal flanks of NOD-SCID mice. 5 x 10^5 cells were injected in a Matrigel (5 mg/mL) solution (200 µL)[105,106], then allowed to grow over approximately 10 weeks before being excised. All protocols conducted using mice were conducted with approval from IACUC UCSD.

1.3.4 Data Collection

1.3.4.1 Atomic Force Microscopy (AFM) Measurements

Hydrogel stiffness was measured by AFM as described[107]. Nanoindentations were performed using a pyrex-nitride probe with a pyramid tip (spring constant ~0.04 N/m, 35º half-angle opening, NanoAndMore USA Corporation, cat # PNP-TR) connected to a MFP-3D Bio Atomic Force Microscope (Oxford Instruments) mounted on a Ti-U fluorescent inverted microscope (Nikon Instruments). After calibration using a glass slide, samples were loaded on the AFM, submersed in phosphate buffered saline (PBS), and indented at a velocity of 2 µm/s with a trigger force of 2 nN. To ensure reproducibility, 3 force maps of ~20 force measurements were performed over a 90 µm x 90 µm region per gel. In addition, measurements were made for three separate gels per condition. Elastic modulus was calculated based on a Hertz-based fit using a built-in code written in the Igor 6.34A software.

1.3.4.2 Imaging

Widefield fluorescent and brightfield microscopy images were obtained using the Leica DMi8. Confocal images were obtained using the Zeiss 880 Airyscan Confocal.

1.3.4.3 Vascular Permeability Measurements

FITC-labeled 70 kDa dextran was flowed through channels either with or without a coating of HUVECs at a rate of 20 μL/min, and allowed to diffuse over 3 minutes to obtain an initial fluorescence measure. This rate was then reduced to 5 μL/min for the next 30 minutes, with fluorescent images taken every 5 minutes. Permeability was calculated in accordance with Equation (1)[71,72,108].

$$P = \frac{1}{I_i - I_b}\left(\frac{I_f - I_i}{t_f - t_i}\right)\frac{d}{4} \quad (1)$$

Here, I_b represents the mean background fluorescence present prior to the addition of dextran, I_i and I_f represent the mean fluorescence at initial and final timepoints, and d represents the diameter of the channel. All image processing was performed using ImageJ.

1.3.4.4 Immunohistochemistry

A detailed example of the immunostaining procedure for the printed constructs is described in Appendix 1.7.3. Briefly, for all immunostaining, printed constructs were extracted from holders, fixed in paraformaldehyde (4%) for 1 hour, washed with 3 rinses of PBS for 1 hour each, and blocked overnight using a solution of BSA (1%) and Triton-X100 (0.125%) in PBS. Constructs were then subject to a 24-hour incubation with primary

antibodies in blocking buffer, an overnight wash with blocking buffer, a 24-hour incubation with secondary antibodies in blocking buffer, and an overnight wash with PBS.

Tissue fragments were either extracted from the matrix, or left in the matrix before being embedded in OCT and frozen in a slurry of dry ice in acetone. Blocks were stored long-term at -80 °C. Fragments were then sectioned into 14 μm slices and mounted on gelatin-coated slides for imaging.

1.3.5 Statistical Analysis

Statistical analysis was conducted using the GraphPad Prism 7 software, and graphical data is displayed as a mean ± standard deviation overlayed on individual data points. All data was analyzed using a two-tailed t-test with Welch's correction, and a p-value of <0.05 was considered to be statistically significant.

1.4 Results and Discussion

1.4.1 Printing 3D Vascularized Constructs Using Free-Standing PVA Scaffolds

An overall schematic of our printing methodology is outlined in **Figures 1.1A** and **1.1B**. In the first series of studies we assessed the viability of using PVA as a sacrificial vascular scaffold. PVA was confirmed to completely dissolve in media within a 1-hour time-frame (**Figure 1.1C**), likely attributed to its water-soluble chemistry (**Figure 1.1A**). Next, to assess swelling properties within a hydrogel environment, 0.7 mm diameter linear PVA scaffolds were printed, embedded within a matrix of 7.5% porcine gelatin and 10 mg/mL fibrin, and then incubated at 37 °C for between 20 - 80 minutes before being evacuated with warm media. Results indicated that minimal to no swelling occurred within

20 minutes, and structures were able to gradually swell to twice their original diameter over 80 minutes (**Figure 1.1D**). Finally, we confirmed the versatility of the approach via the ability to readily construct a range of viable vascular geometries embedded within a hydrogel matrix of 7.5% porcine gelatin and 10 mg/mL fibrin, which could in turn be evacuated successfully using warm media (**Figure 1.1E**), leaving behind the desired vascular lumens.

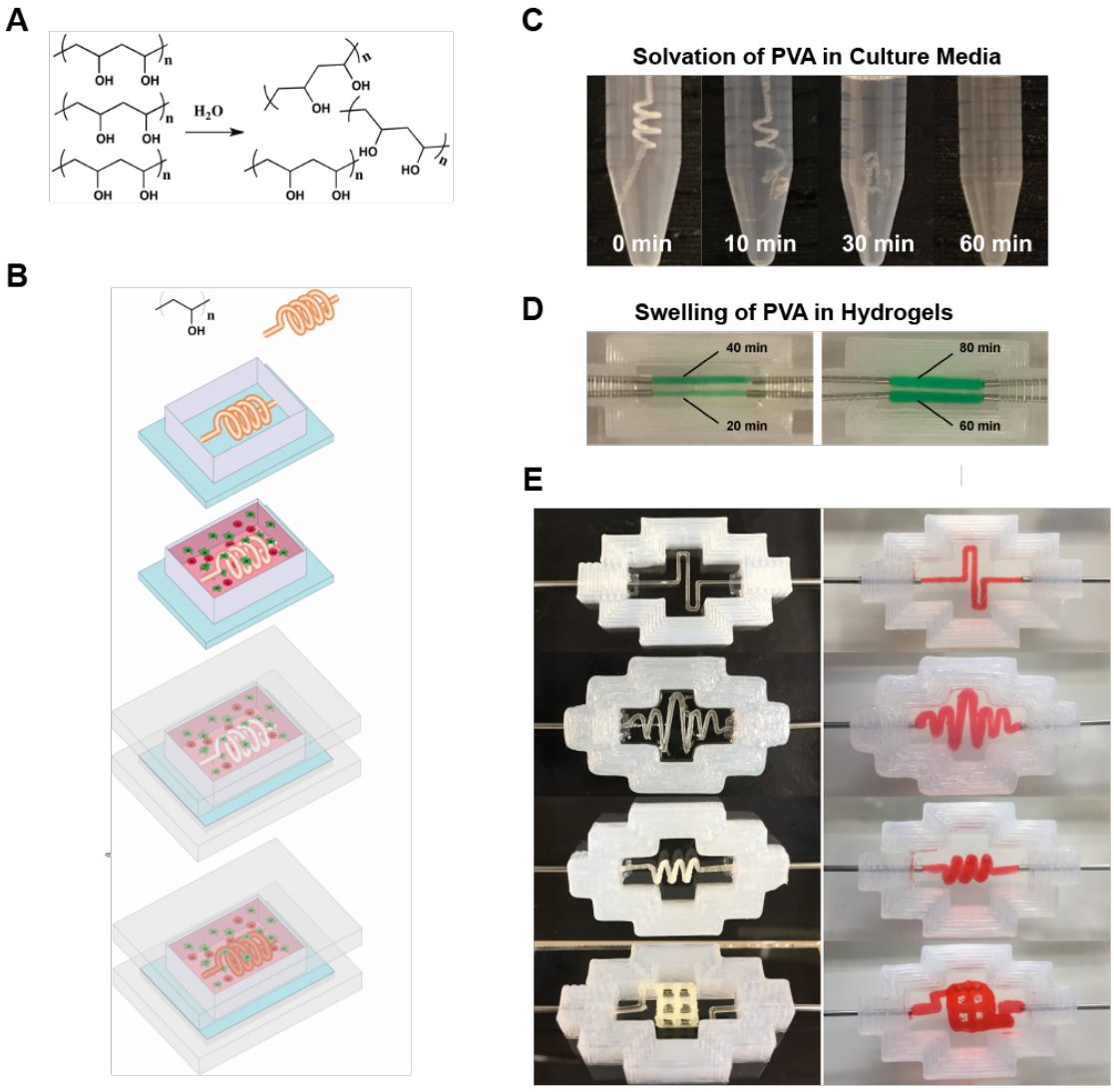

Figure 1.1: Printing 3D vascularized constructs using PVA scaffolds. (A) Chemical structure of PVA and solvation in water. **(B)** Schematic representation of the vascularized construct manufacturing procedure. A PVA scaffold of desired geometry is printed and inserted into a silicone holder. The PVA scaffold is then encapsulated within a matrix formulation of desired composition. The matrix formulation is allowed to gelate and simultaneously, the PVA scaffold slowly dissolves. The structure is then sealed using an acrylic base and lid, and the scaffold is evacuated using warm media. Following evacuation, the resulting lumen can be seeded with endothelial or epithelial cells. **(C)** Timecourse images showing solvation of PVA in room temperature media over 60 minutes. **(D)** Images demonstrating swelling of PVA in a matrix of 7.5 wt% gelatin and 10 mg/mL fibrin. PVA scaffolds were allowed 20, 40, 60, or 80 minutes to solvate prior to evacuation, resulting in channels of different diameters. **(E)** Examples of 2D and 3D geometries that can be printed and evacuated using PVA. Images on the left show the PVA structures prior to evacuation, and images on the right show the perfused channels following evacuation. Scaffolds in this figure were encapsulated within a matrix of 7.5 wt% gelatin and 10 mg/mL fibrin.

When applied to living cells, we also confirmed the presence of PVA within cell culture media had no negative impact on the growth of either HUVECs or MDA-MB-231 cells (**Figures 1.2A and 1.2C**). To assess viability, we used the CCK8 reagent, and towards this validated the correlation between CCK8 absorbance readouts and cell numbers in the context of our studies (**Figure 1.2B**).

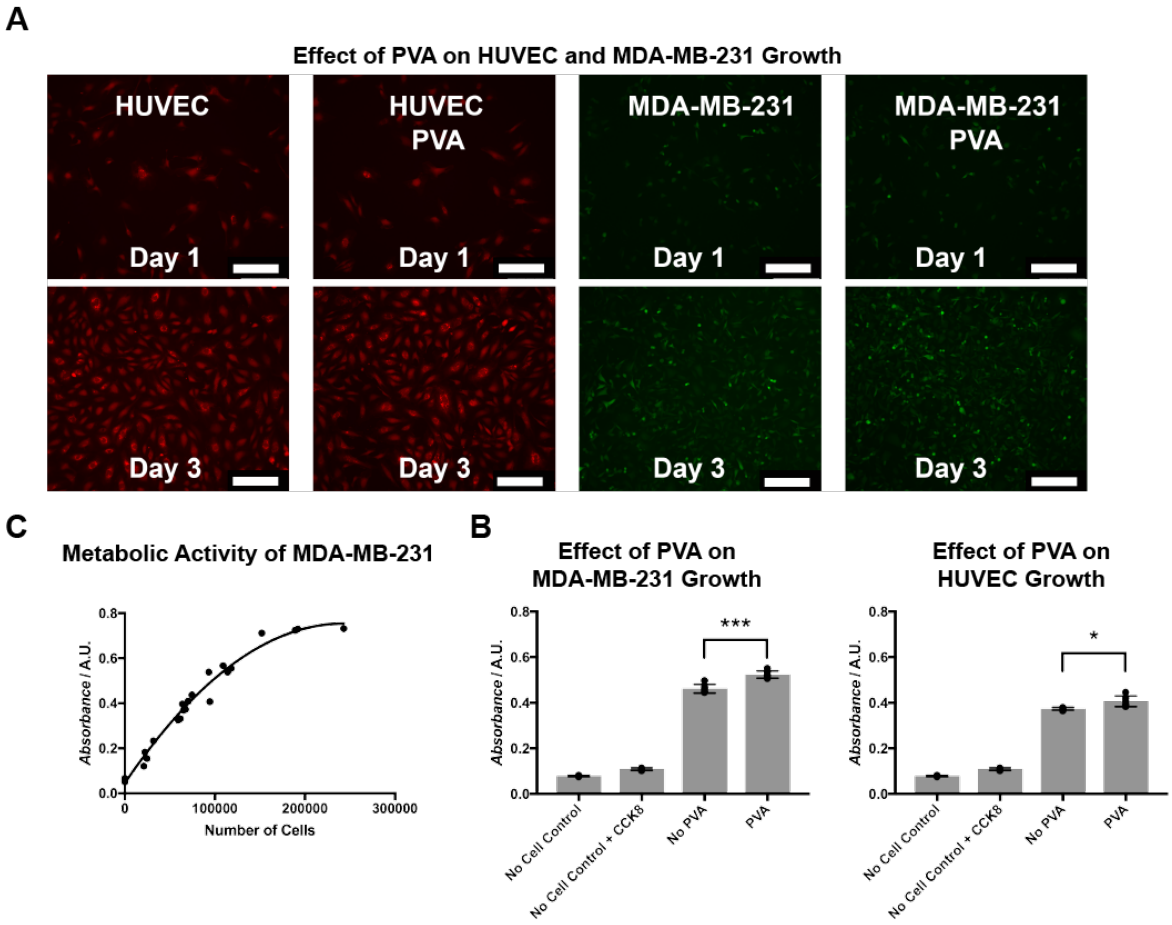

Figure 1.2: Effect of PVA on Cell Growth and Viability. (A) Fluorescent images showing growth of mCherry-labeled HUVECs (left) and GFP-labeled MDA-MB-231 cells (right) grown in 2D culture in media with or without PVA dissolved at a concentration of 500 mg/mL. Scale bars: 250 μm. **(B)** Absorbance measurements of MDA-MB-231 cells obtained using a CCK8 assay. Numerical cell quantities were obtained using a cell counter, and results validate the use of the method as a quantification of cell growth of cell number. **(C)** Effect of PVA on cell growth shown via absorbance measurements of HUVECs (left) and MDA-MB-231 cells (right) grown in 2D culture in media with or without PVA dissolved at a concentration of 500 mg/mL (n = 4 with P-values *P<0.05 and ***P<0.001).

Subsequently, we constructed vascularized constructs using 5 mg/mL Matrigel and 10 mg/mL fibrin matrices seeded with human mesenchymal stem cells (hMSCs) followed by seeding of HUVECs within the residual channels (post evacuation of PVA structures) and perfusion over multiple days. Results indicated that HUVECs adhered even with complex channel geometries (**Figure 1.3A**) and formed a monolayer around the lumen (**Figure 1.3C**). Endothelial barrier functionality was confirmed via perfusion and permeability measurements of FITC-conjugated 70 kDa dextran (**Figure 1.3B**). Fixation and staining of HUVECs with mouse monoclonal anti-CD34 (Thermofisher) and rabbit monoclonal anti-VE-Cadherin (Cell Signaling Technologies) indicated that they expressed proper endothelial lineage markers and formed adherens junctions[109] within 10 days (**Figure 1.3D**). In addition, staining of hMSCs cultured within the matrix using mouse monoclonal anti-CD105 (Thermofisher) and Alexa-594 phalloidin (Thermofisher) confirmed viability and maintenance of cell potency[110] (**Figure 1.3E**).

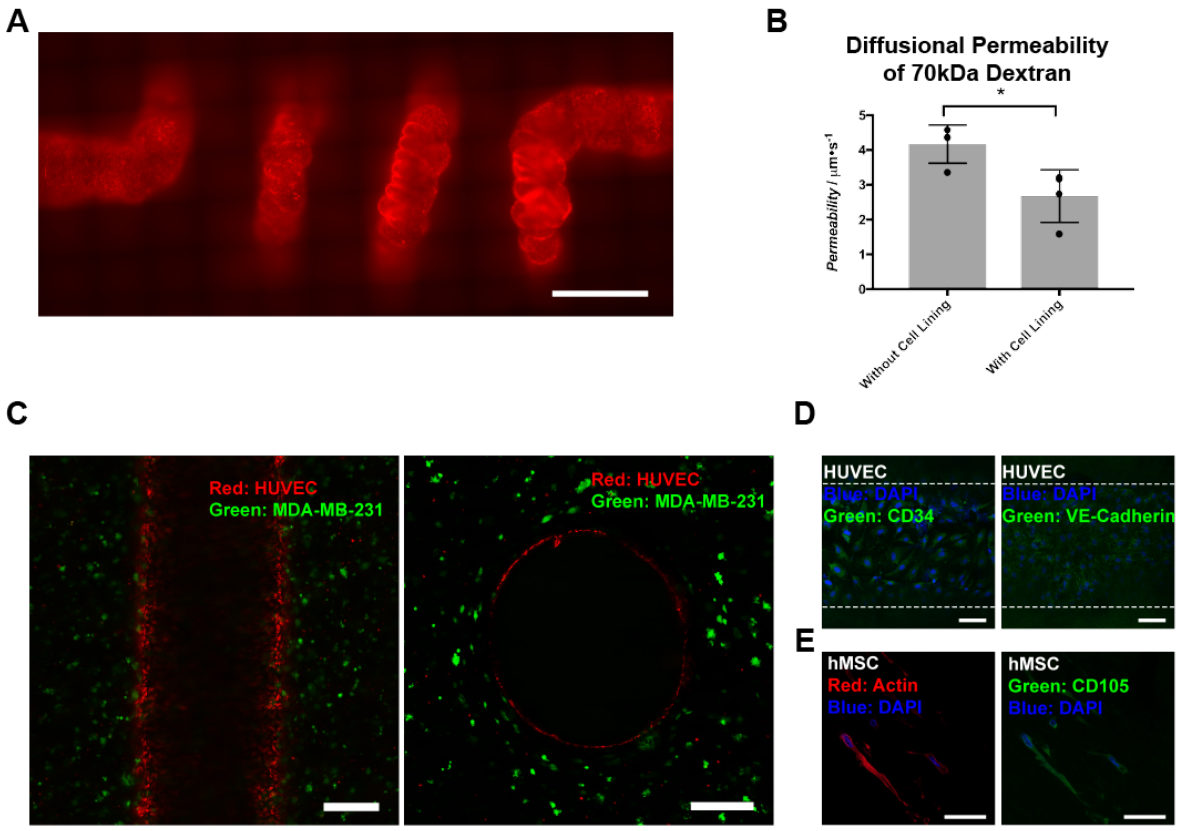

Figure 1.3: Optimization and characterization of printing 3D vascularized constructs using PVA scaffolds. (A) Fluorescent image of a 3D spiral-shaped channel seeded with mCherry-labeled HUVECs. Scale bars: 2mm. **(B)** Barrier properties of endothelial cells demonstrated with a comparison of diffusional permeability for channels with (right) and without (left) a lining of HUVECs. Values were obtained by perfusing 70 kDa FITC-dextran through the channels over 30 minutes (n = 3 with P-value *P<0.05). **(C)** Fluorescent images of a longitudinal (left) and cross-section (right) of a vascular channel formed from PVA. The matrix stroma contains GFP-labeled MDA-MB-231 cells, and the channel lumen is seeded with mCherry-labeled HUVECs. Scale bars: 400 μm. **(D)** Immunostains of HUVECs seeded in the lumens formed following evacuation of PVA scaffolds. Blue shows DAPI, while green shows CD34 (left) and VE-cadherin (right). Scale bars: 100 μm. **(E)** Immunostains of hMSCs encapsulated within the matrices of vascularized constructs, and sustained via perfusion over 10 days. Blue shows DAPI, red shows actin, and green shows CD105. Scale bars: 50 μm.

Beyond introducing a single main vascularized channel to a matrix construct, we also assessed the viability of adding a dense and fine vascular bed. This was accomplished by wrapping water-soluble PVA-based thread (Solvron, Nitivy Co. 62T Type SS) around the main PVA scaffold (**Figure 1.4A and 1.4B**) prior to encapsulation. Because of increased fluid flow resistance exhibited by the pathways containing Solvron

(100-400 μm diameter channels) in comparison to the main PVA channel, clearing of the former took place over multiple days following endothelial seeding. Results showed that seeded HUVECs migrated into the channel tracks left behind by evacuated Solvron, creating microvasculature capable of linking different portions of the primary vascular network (**Figure 1.4C**), with functionality confirmed via flow of 70 kDa FITC-dextran. Taken together, PVA based sacrificial structures enable facile construction of vascularized tissue constructs with diverse programmable 3D geometries and channel dimensions ranging from 100-1000 μm.

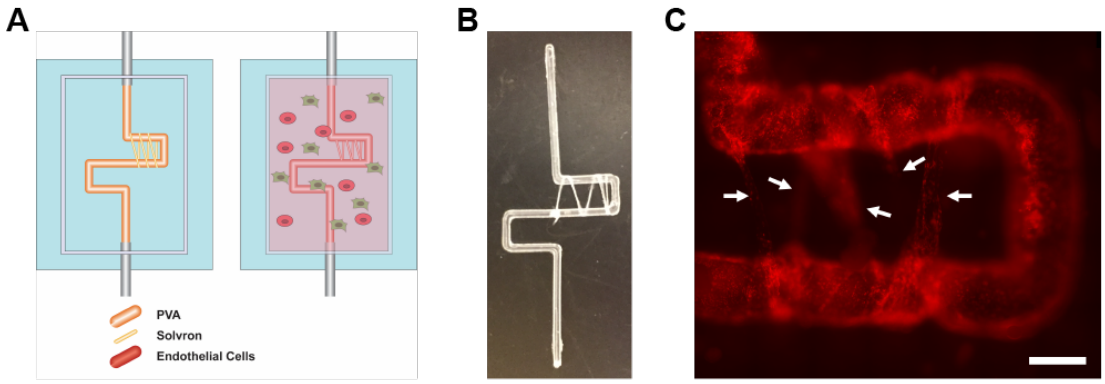

Figure 1.4: Increasing Vascular Density via PVA Threads. (A) Schematic representation of dense vascular bed induction procedure. A PVA scaffold of desired geometry is printed and wrapped with PVA (Solvron) threads, before being encapsulated and dissolved. Over time, Solvron threads also dissolve, resulting in narrow channels into which endothelial cells may migrate. **(B)** A PVA scaffold partially wrapped with Solvron thread. **(C)** Fluorescent images of mCherry-labeled HUVECs migrating into narrow channels left by evacuated Solvron. Scale bars: 1 mm.

1.4.2 Development of an Optimally Cell-Compatible Matrix

We next sought to design a matrix environment suitable for high cell growth and promotion of diverse cellular responses while compatible with maintaining the structural stability necessary for evacuation of PVA and long-term perfusion. In this regard, previous studies have extensively made use of synthetic matrices. However, with a goal to

increase similarities to the *in vivo* microenvironment, we primarily explored biological matrices such as collagen, fibrin[71,72], and Matrigel[111,112].

Towards this, we first examined the compatibility of our methodology with a range of matrix materials that include fibrin, gelatin, collagen, and Matrigel. Specifically, PVA scaffolds of a square wave geometry were printed, embedded in, and evacuated from matrices of varied compositions (**Figure 1.5A**), confirming viability of use.

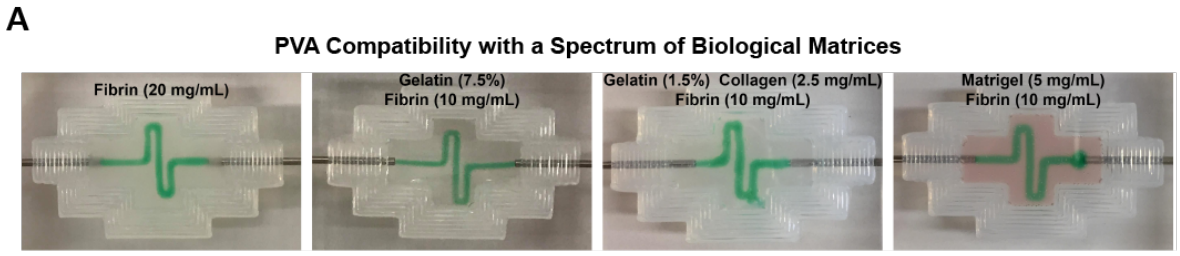

Figure 1.5. Evaluating material compatibility of PVA. (A) Images indicating successful evacuation of PVA from matrices composed of various biological materials.

To assess the impact of the introduction of Matrigel on cell growth and viability, two breast cancer epithelial cell lines (MDA-MB-231 and MCF7) were encapsulated in matrices of varied composition and grown over 10 days. All matrices contained 10 mg/mL fibrin, along with gelatin, Matrigel, or a blend of the two (**Figure 1.6A**). Average hydrogel stiffness, as measured via AFM, showed less than 1 kPa variation across all gelatin-containing conditions, while a significant reduction in stiffness was observed in the absence of gelatin (**Figure 1.7A**). Growth over time was qualitatively confirmed via fluorescent microscopy (**Figure 1.6B**), and quantitative measurements of metabolic activity were obtained using the CCK8 reagent (**Figures 1.6C and 1.6D**). Results indicated that the presence of Matrigel significantly increased cell growth, both with and without gelatin, which we believe can be attributed to the various biological basement

membrane components contained within it[113]. Lower absorbance from MCF7 cells can be explained by their relatively slower growth rate compared to MDA-MB-231 cells.

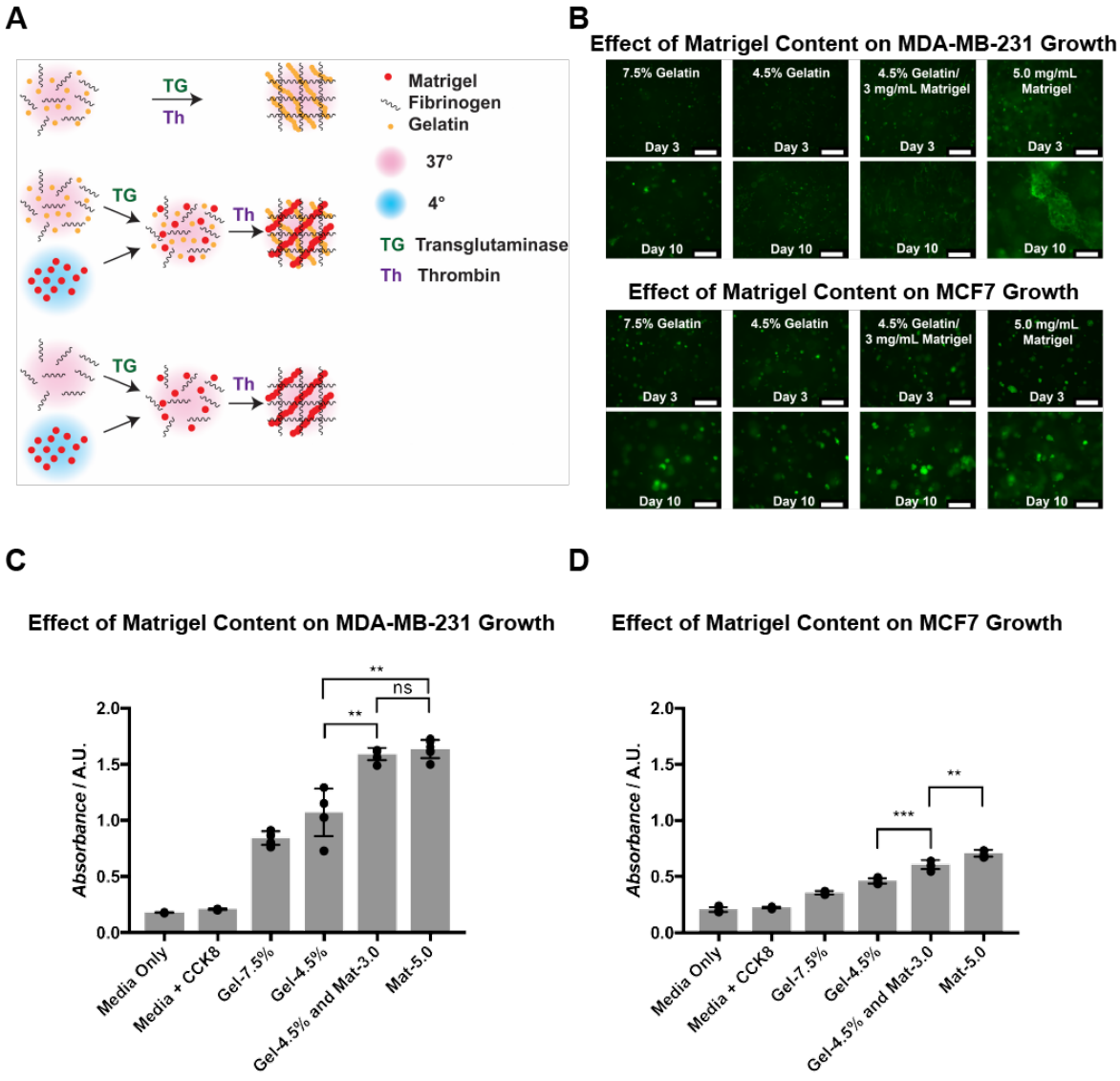

Figure 1.6. Development of optimally cell-compatible constructs based on biologically derived matrix materials (I). (A) Schematic representation of the materials-testing procedure. Gelatin/fibrin matrices were formulated by mixing both components with transglutaminase, then polymerizing with thrombin at 37 °C. Matrigel/fibrin and gelatin/Matrigel/fibrin blended matrices were formulated by mixing all components except Matrigel with transglutaminase at 37 °C, then adding Matrigel and polymerizing with thrombin. Matrigel was maintained at 4 °C, while all other components were maintained at 37 °C during the procedure. **(B)** Fluorescent images showing growth of GFP-labeled MDA-MB-231 cells and MCF-7 cells in matrices of various compositions. Scale bars: 250 μm. **(C-D)** Absorbance measurements of MDA-MB-231 cells and MCF-7 cells grown in matrices of various compositions, obtained using a CCK8 assay (n = 4 with P-values **P<0.01 and ***P<0.001)

An identical experiment was conducted with hMSCs to assess the effect on the stromal cells, with the duration increased to 20 days to account for a slower rate of growth. Both quantitative (**Figure 1.7B**) and qualitative (**Figure 1.7C**) results mirrored those of the breast cancer epithelial cells.

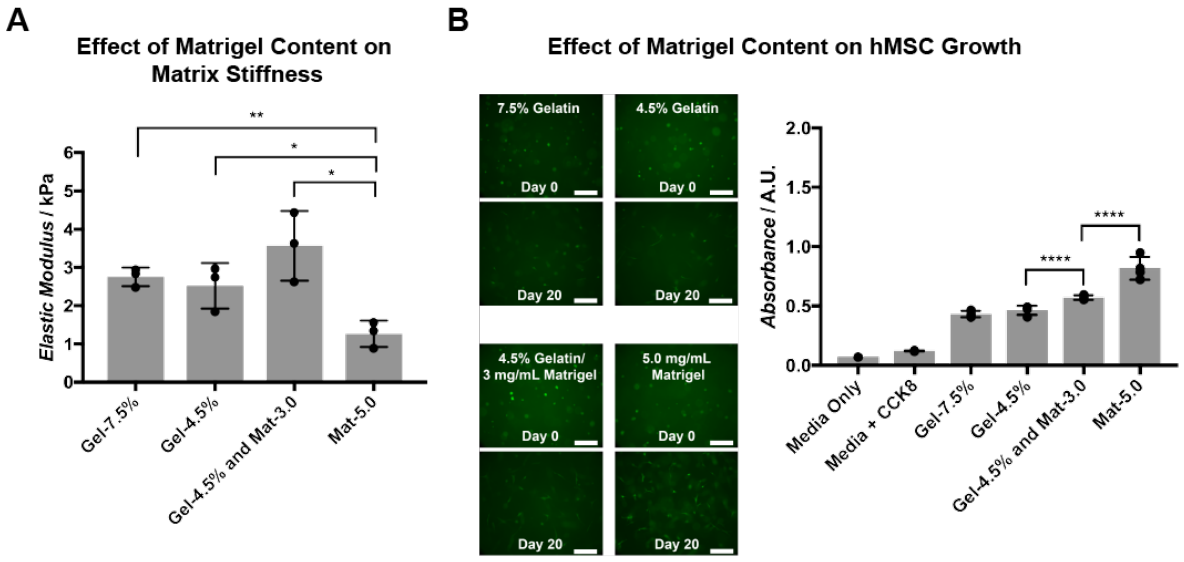

Figure 1.7: Optimization and characterization of cell-compatible constructs based on biologically derived matrix materials (II). (A) Elastic moduli of matrices of various compositions as measured via AFM (n = 3 with P-values *P<0.05 and **P<0.01). **(B)** Fluorescent images and absorbance measurements of hMSCs grown in matrices of various compositions, obtained using a CCK8 assay (n = 4 with P-values **P<0.01 and ***P<0.001). Scale bars: 250 μm.

In addition to designing an ideal matrix environment, we also optimized media conditions that would allow for co-culturing of multiple cell types, specifically in this case, endothelial cells within the channel and tumor cells within the stroma. Cells were grown in media formulations containing varying amounts of DMEM, FBS, L-glutamine, and EGM-2 (Lonza). Control media for MDA-MB-231 cells and HUVECs were DMEM supplemented with 10% FBS and 2 mM L-glutamine, and EGM-2 respectively. Both qualitative results (**Figures 1.8A and 1.8B**) and quantitative results (**Figures 1.8C and 1.8D**) indicated that a 50/50 mixture of EGM-2 and DMEM supplemented with 20% FBS

and 4 mM L-glutamine maximized growth of MDA-MB-231 cells while producing no significant effect on the growth of HUVECs compared to controls in EGM-2 only.

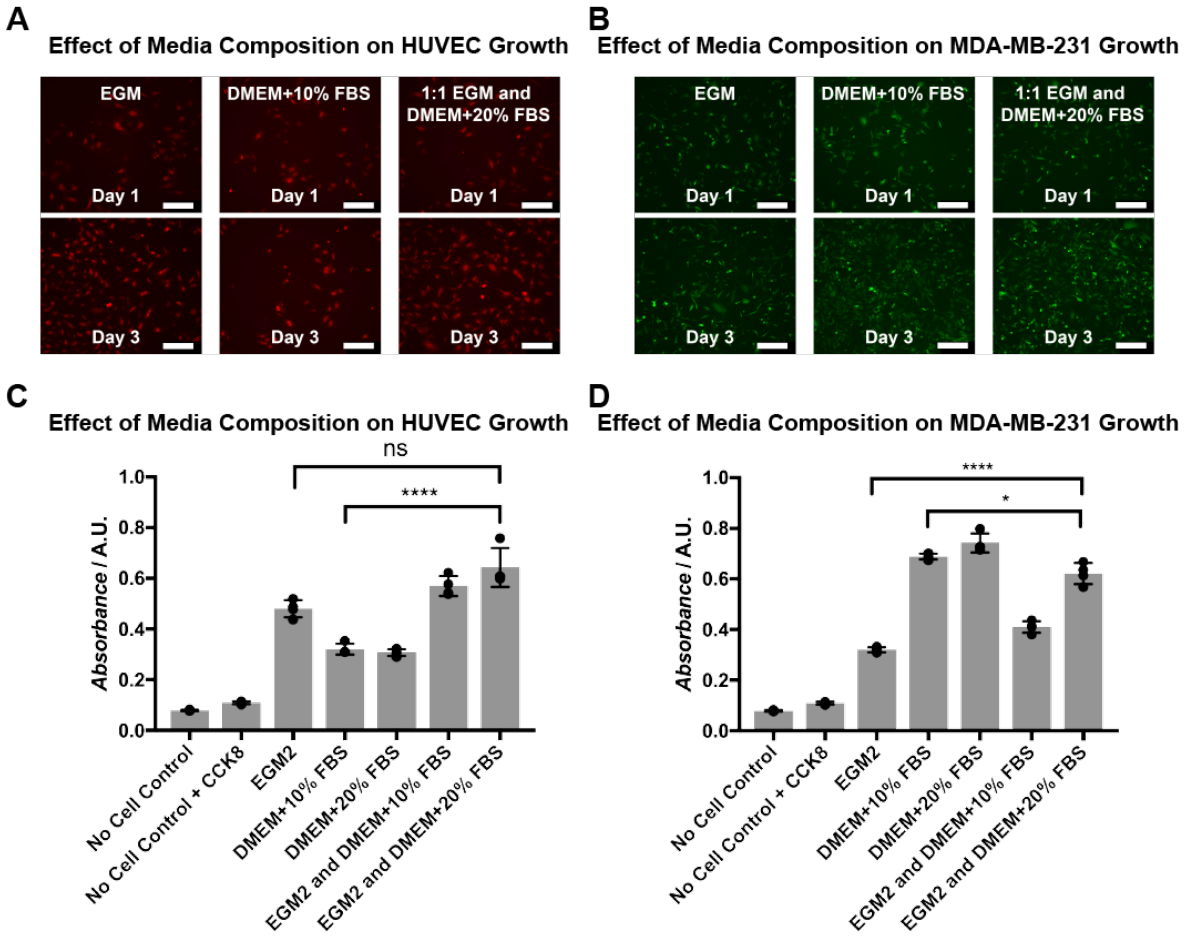

Figure 1.8: Optimization and characterization of media formulations for cell co-culturing. (A - B) Fluorescent images showing optimization of media compositions for coculture of HUVECs and MDA-MB-231 cells. HUVEC and MDA-MB-231 cell growth in controls of EGM2 and DMEM supplemented with 10% FBS and 2 mM L-glutamine is compared with growth in the optimal formulation. Scale bars: 250 μm. **(C - D)** Quantitative confirmation of results from the previous figures (n = 4 with P-values *P<0.05 and ****P<0.0001). Absorbance from the CCK8 assay shows relative growth in different media formulations, with overall results indicating that a 1:1 mixture of EGM2 and DMEM supplemented with 20% FBS and 4 mM L-glutamine allows for optimal HUVEC growth while minimally compromising MDA-MB-231 growth. Notably, all DMEM is supplemented with either 10% FBS and 2 mM L-glutamine, or 20% FBS and 4 mM L-glutamine.

Having established a robust system for engineering long-term culturable vascularized constructs based on biologically derived matrices we next focused on

evaluating the system in the contexts of two distinct application scenarios to highlight the methodologies broad applicability. Specifically, in the first we explored the ability of the engineered vascularized tissue to sustain embedded biopsied tumor pieces long-term in a fully *ex vivo* setting. In the second, we expanded the system's capabilities to engineer hybrid vascular systems supporting flow of distinct biological fluids, specifically focusing on engineering an *ex vivo* vascularized gut-like system.

1.4.3 Application of the Methodology to In Vitro Tumor Sustenance

To examine the feasibility of using the vascularized matrix to sustain tumor tissue *ex vivo*, tumors were grown from GFP MDA-MB-231 cells in NOD-SCID mice, excised, fragmented, and embedded in either a vascularized tissue construct, or non-vascularized matrices of equal thickness (**Figures 1.9A-C**). Both vascularized and non-vascularized conditions used matrices of 10 mg/mL fibrin and 5 mg/mL Matrigel, and were seeded with hMSCs, which are known to have essential roles in the stromal microenvironment[114]. Vascularized tissue constructs were continuously perfused with fresh media, changed every 2 days, while non-vascularized tissue constructs had fresh media added twice a day. In both conditions, the previously-identified optimum media formulation was used (1:1 mixture of EGM2 and DMEM supplemented with 20% FBS and 4 mM L-glutamine). After 21 days, half of the tumor fragments of all conditions were excised and cell viability was measured using the CCK8 reagent (**Figure 1.9D**).

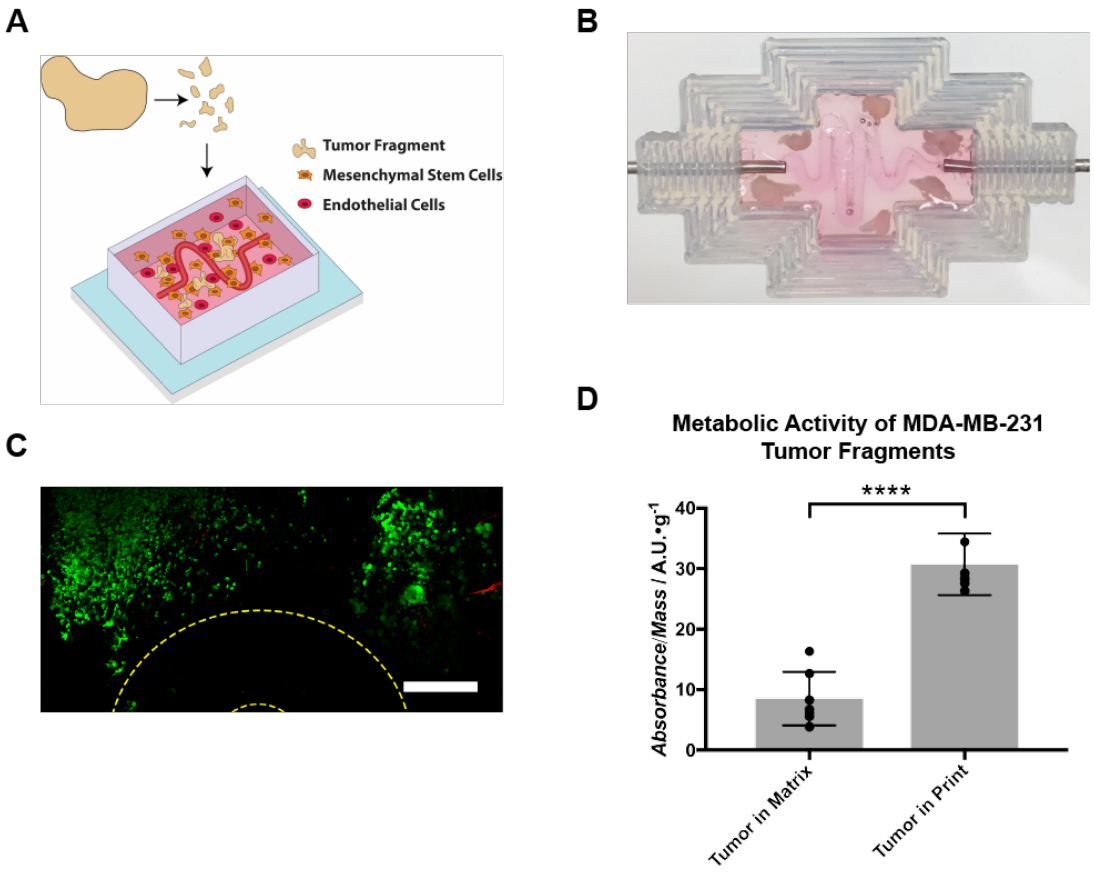

Figure 1.9: Applications of the methodology. In vitro tumor sustenance. (A) Schematic showing the process by which MDA-MB-231 tumors grown in mice were excised, fragmented, and encapsulated within a vascularized construct, before being perfused over multiple weeks. **(B)** Image showing tumor fragments encapsulated within a vascularized construct with a sinusoidal geometry. **(C)** Fluorescent confocal images of GFP-labeled MDA-MB-231 tumor fragments after 24 days of perfusion within a vascularized construct. The location of the vascular channel is outlined in yellow. Because of the thickness and positioning of the tumor fragments, capturing the vascular channel and tumor fragments within the same plane was not possible. Scale bars: 300 μm. **(D)** Absorbance measurements of MDA-MB-231 tumor fragments sustained over 24 days while encapsulated in either a static matrix, or a perfused vascularized construct. Measurements were obtained with a CCK8 assay. To account for the variability introduced by tumor fragments of different sizes, all measurements were normalized with respect to mass (n = 6 with P-value ****P<0.0001).

The remaining tumor fragments were embedded in OCT, cryosectioned, mounted, and imaged directly (**Figures 1.10A – 1.10C**). Confocal images of perfused tumor fragments prior to extraction indicated that they were viable and living in dense tissue clusters after 21 days, and the results of CCK8 measurements confirmed significantly higher viability of fragments embedded in perfused constructs compared to non-perfused

matrices. This was further reinforced by results of post-sectioning GFP expression. In this context, greater expression of GFP in sectioned tissue represented greater proportions of surviving cells at the time of extraction and freezing, and images indicate that although degrees of cell death and loss of tissue integrity occurs in both perfused (**Figure 1.10C**) and static (**Figure 1.10B**) conditions, a significantly greater proportion of cells under perfused conditions appear to have survived.

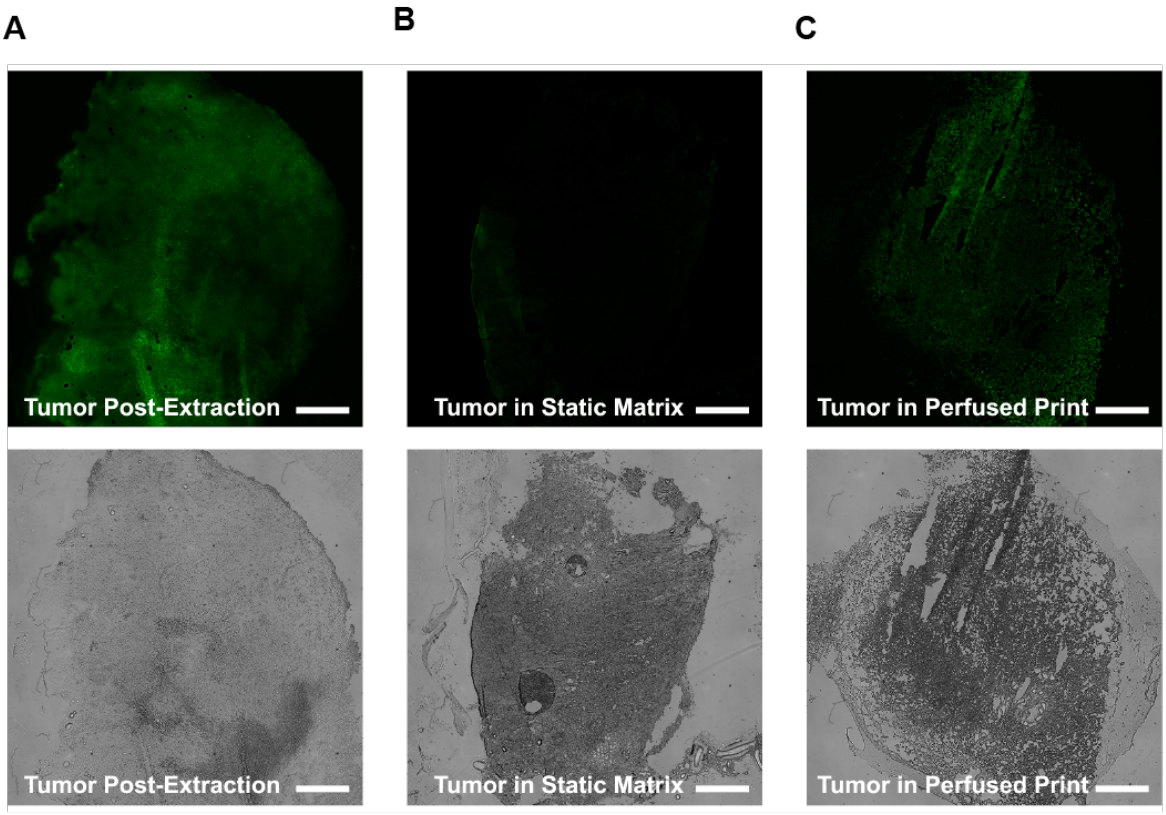

Figure 1.10: Characterization of applications of the methodology. In vitro tumor sustenance. (A - C) Fluorescent (top) and brightfield (bottom) images of MDA-MB-231 tumor fragment prior to fixation. The images respectively represent tumor fragments that were embedded in OCT and cryosectioned immediately after excision **(A)**, and tumor fragments embedded and cryosectioned only after being sustained in either a static matrix culture **(B)** or a perfused vascularized construct **(C)** for 21 days. Scale bars: 500 μm.

1.4.4 Application of the Methodology to Generating Hybrid Vascularized Systems

Following confirmation of the system's ability to maintain tissue viability *ex vivo*, we next applied it to generate a hybrid vascularized organ system *in vitro*. Here a modified lumenal geometry was designed consisting of a linear channel surrounded by a spiral. The central channel was seeded with Caco-2 intestinal epithelial cells, while the outer spiral was seeded with HUVECs, generating a system mimicking a vascularized gut (**Figures 1.11A and 1.11B**).

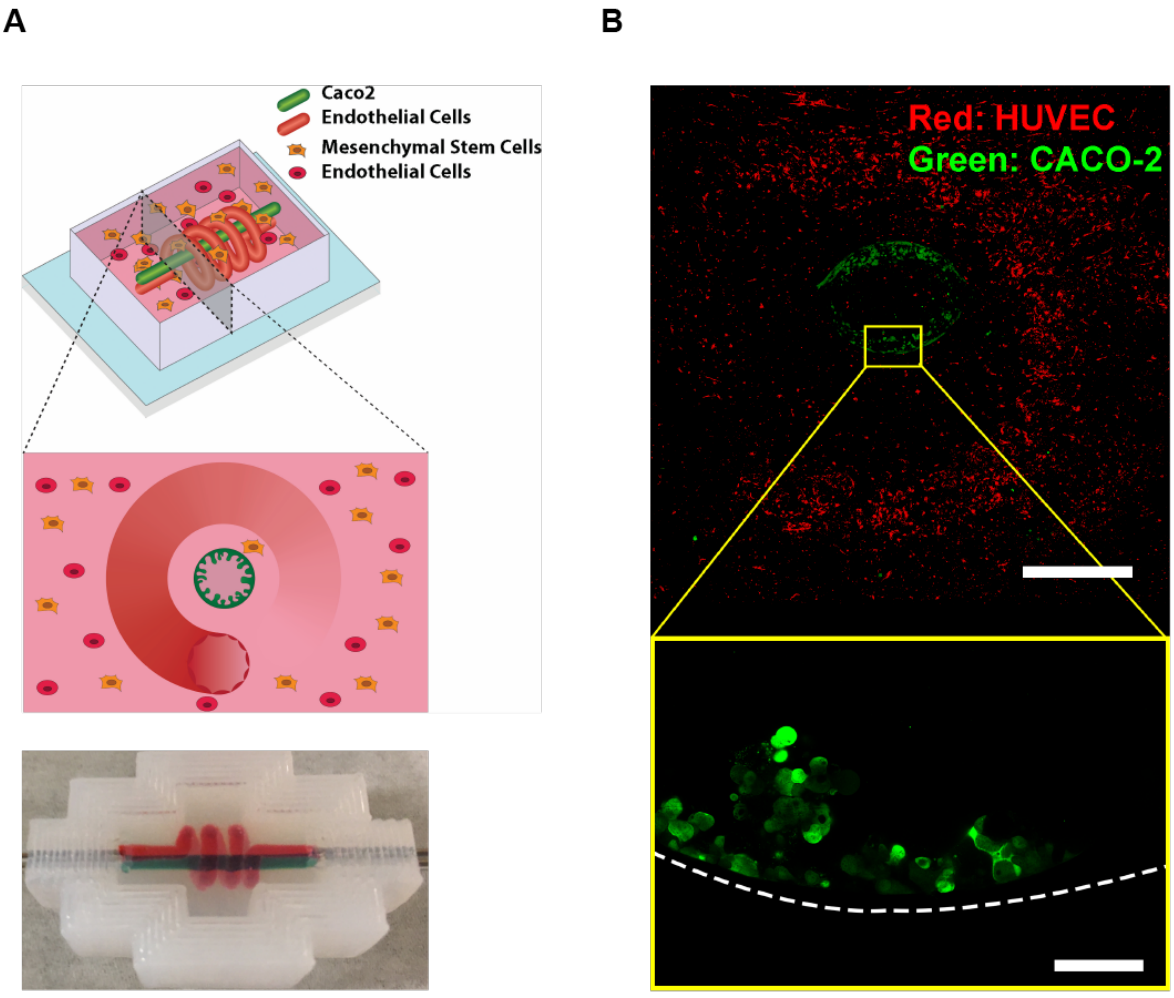

Figure 1.11: Applications of the methodology. Hybrid vascularized systems. (A) Image of a multi-channel construct generated by encapsulating and evacuating more than one PVA scaffold within a single matrix, along with a schematic diagram of a gut-organoid constructed by creating multiple lumens in a single matrix, designed to imitate endothelial and epithelial cocultures. The outer lumen is a 3D spiral, and is seeded with endothelial cells. The inner lumen is a channel and is seeded with gut epithelial cells. **(B)** Fluorescent confocal images of GFP-labeled Caco-2 cells and mCherry-labeled HUVECs seeded respectively within an inner linear channel and an outer spiral channel of a vascularized construct. The top image shows a cross-sectional view of the construct. The bottom image shows a close-up of the Caco-2 cells, indicating formation of finger-like protrusions. Scale bars: 1 mm (top) and 100 μm (bottom).

Prior to the hybrid system, we examined the ability of the perfused construct to sustain an *in vitro* gut model by seeding evacuated channels with GFP Caco-2 cells, and then subjecting them to either static culture or perfusion over 12 days. Confocal fluorescent microscopy revealed the arrangement of a confluent Caco-2 layer on the

channel interiors in both cases. However, perfusion resulted in the formation of 3-dimensional protrusion-like arrangements, while static culture did not (**Figure 1.12A**). Immunostaining was performed using rabbit monoclonal anti-Na^+/K^+ ATPase (Thermofisher) and Alexa-594 phalloidin (Thermofisher), confirming the presence of F-actin-coated borders, as well as Na^+/K^+ ATPase transporters within the aforementioned projections (**Figure 1.12B**). When extended to the hybrid system, this behavior was maintained, with Caco-2 cells still expressing villus-like morphology, and endothelial cells forming a channel around them (**Figure 1.11B**), with a minimum separation distance of less than 200 um. Together, these results indicate the viability of supporting cocultures of epithelial and endothelial cells, each with a unique microenvironment, in extremely close proximity.

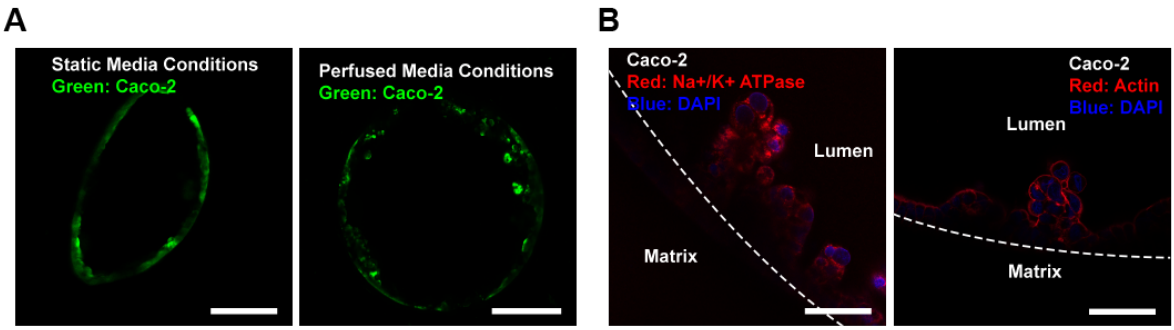

Figure 1.12: Characterization of applications of the methodology. Hybrid vascularized systems. (A) Fluorescent confocal images of cross-sections of matrix constructs containing lumens seeded with GFP-labeled Caco-2 cells. Constructs were either sustained via static culture (left) or perfused at 12 µL/min (right) over 12 days. Caco-2 cells in the unperfused construct show monolayer morphology similar to 2D culture, while Caco-2 cells in the perfused construct arrange into finger-like protrusions. Scale bars: 200 µm (left) and 400 µm (right). **(B)** Fluorescent confocal images showing immunostains of Caco-2 cells seeded within the lumen of a matrix construct and perfused over 12 days. Blue shows DAPI, while red shows either Na^+/K^+ ATPase (left) or actin (right). Scale bars: 50 µm.

1.5 Conclusions

In summary, 3D printing of PVA coupled with use of biologically derived matrices enables a robust and reproducible methodology for generating highly functional vascularized tissue constructs. Within this chapter, we developed an engineered tissue model that contained a vascular channel seeded with primary endothelial cells, and was capable of sustaining both cells and tissue fragments long-term. In addition, we demonstrated the viability of creating co-cultures of Caco-2 gut epithelial cells with primary endothelial cells that mimicked *in vivo* gut-like organization patterns. As a whole, we believe that our technique offers a method to create highly complex tissue models that can be used to study biological phenomenon. Moreover, because of the simplicity of the technique, it is highly accessible in many research settings, and as such, has the potential to significantly accelerate progress in tissue engineering.

1.6 Acknowledgements

Chapter 1, in full, is material that appears in Facile Engineering of Long-Term Culturable Ex Vivo Vascularized Tissues Using Biologically Derived Matrices as it appears in Advanced Healthcare Materials Volume 7, 2018. I, as the dissertation author, was the primary author of this paper, with the full authors list being: Michael Hu, Amir Dailamy, Xin Yi Lei, Udit Parekh, Daniella McDonald, Aditya Kumar, and Prashant Mali.

1.7 Appendix

1.7.1 Preparation of Stock Gelatin Solution

Described below is an example of a preparation method for a stock gelatin solution at approximately 150 mg/mL.

1. Add 10 mL of PBS to a 15 mL centrifuge tube.
2. Slowly add 1.5g of lyophilized gelatin to the PBS.
3. Place centrifuge tube on thermomixer at 70°C for 12 hours.
4. Remove centrifuge tube from thermomixer and allow to cool to approximately 37°C. Do not allow it to cool further, or the entire solution will gelate.
5. Use pH meter and 1 M NaOH to adjust the pH of the gelatin solution to 7.5.
    a. This should take approximately 100 uL of 1M NaOH for 10 mL of gelatin solution.
6. Return gelatin solution to thermomixer and warm to 70°C again.
7. Filter gelatin solution with Steriflip Filter (EMD Millipore).
    a. This must be done while Gelatin is warm to avoid premature gelation.
8. Store stock gelatin solution at 4°C.

1.7.2 Preparation of Perfused Printed Construct

Described below is an example of a preparation method for a perfused printed construct formulated from a 1 mL matrix solution composed of 10 mg/mL fibrin, 4 mg/mL Matrigel, and 10 mg/mL gelatin.

Preparation of Matrigel, Gelatin, and Thrombin

1. Remove the Matrigel needed from -20°C at least 1 hour before starting the preparation and place on ice.
2. Remove stock 150 mg/mL gelatin solution from -4°C at least 1 hour before starting the preparation, and place at 37°C.
3. Remove stock 500 U/mL thrombin solution from -20°C and place on ice.

Preparation of 100 mg/mL Stock Fibrinogen Solution

4. Warm sterile dPBS (usually in TC fridge) to 37°C in water bath or incubator.
5. Obtain a sterile 1.5 mL vial, and weigh empty while closed.
6. Measure out 10 mg fibrinogen in a sterile operating environment
7. Rapidly add 100 uL warmed dPBS to fibrinogen and gently tap vial until every portion of the fibrinogen is wetted by the dPBS. Do NOT pipette the solution.
8. Incubate Fibrinogen at 37°C for 30 minutes, or until fully dissolved.

Preparation of 50 mg/mL Stock Transglutaminase Solution

9. Obtain a sterile 1.5 mL vial, and weigh empty while closed.
10. Measure out 5 mg transglutaminase in a sterile operating environment.
11. Add 100 uL warmed dPBS to transglutaminase and mix with pipette until dissolved into cloudy solution

12. Incubate at 37°C until fully dissolved.

Preparation of PVA Structures in Silicone Chips

13. Obtain sterile PVA vascular structures and place inlet and outlet ends into the metal perfusion channels in the silicone chip.

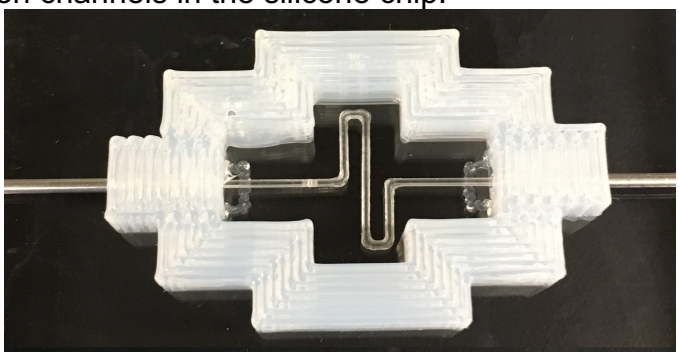

Figure 1.13: Example of a PVA structure prior to encapsulation and evacuation.

14. Gently insert solid metal rods of equal diameter to the inner diameter of the inlet and outlet metal perfusion channels until they come into contact with the PVA structures. The purpose of this is to prevent air pockets from forming.

Matrix Preparation

Matrigel should be kept on ice to prevent gelation. The order by which the components are added in this case is important. Gelatin and Matrigel have opposite temperature-responsive geling behavior, and must be kept separated.

15. Aliquot 400 uL Matrigel into 1.5 mL centrifuge tube.
16. Add 384 uL warmed media into 1.5 mL centrifuge tube.
17. Add 66 uL of warmed stock gelatin solution into warmed media.
18. Add 10 uL of 250 mM calcium chloride solution to warmed media.
19. Add 40 uL of stock transglutaminase solution to warmed media.
20. Add 100 uL of stock fibrinogen solution to warmed media.
21. Mix very well by pipetting at least 10 times.
22. Incubate for 20 minutes or more at 37°C to allow for transglutaminase to crosslink gelatin for optical clarity.
23. Harvest and spin down all cells of interest to be encapsulated within the matrix.
24. Add 2 uL of thrombin stock solution to the Matrigel solution and mix well.
25. Rapidly add the warmed media and matrix solution prepared in Steps 16 – 21 to the Matrigel and thrombin solution. Mix by pipetting at least 5 times.
26. Re-suspend all cells in complete matrix solution such that they will be resuspended at concentrations desired.
27. Pour Solution into silicone chips, over the PVA structures.
28. Let the chip sit for 5 minutes at room temperature, then place in 37°C for 20 – 30 minutes. At the end of this, the entire system should be gelated, and the PVA scaffold should have melted.

Evacuation of Sacrificial PVA Vasculature

29. Small portions of the PVA will remain isolated from the aqueous environment of the gelating matrix due to being inside the metal perfusion channels. Use the solid metal rods inserted in Step 14 to carefully and slowly push those portions of PVA forward, into the rest of the melted PVA.
30. Allow incubation for another 15 – 30 minutes.
31. During the incubation period, media for perfusion culture should be warmed to 37°C.
32. Fill 1 set of tubing with warm media. If necessary, sterilize with ethanol beforehand.
33. Remove samples from incubator.
34. Seal samples in an acrylic holder plate if not already sealed.
35. Remove solid metal rods from printed construct, taking care to make sure other parts of construct are not disturbed.
36. Link printed construct with perfusion pump tubing, and slowly perfuse with warm media to evacuate the melted PVA.
37. Perfuse for 5 minutes or more to ensure that all remaining PVA is removed.

Optional Endothelialization Step

1. Allow printed constructs to perfuse for at least several hours before initiating endothelialization.
2. Harvest and spin down Endothelial Cells.
3. Re-suspend cells such that they can be delivered to the matrix at concentrations desired. For endothelial cells, the desired concentration is ~5 - 10 x 10^6 cells/mL.
4. Use 200 mL pipette to VERY slowly inject endothelial cell solution into matrix.
5. Let sit 1 hr to allow Endothelial Adhesion.
6. Turn upside down for 1 hr to allow Endothelial Adhesion to other side.
7. Let sit 6 – 12 hrs (overnight preferred).
8. Begin perfusion with EGM.

1.7.3 Immunostaining of Printed Tissue Constructs

Described below is a series of steps that may be used to immunostain printed tissue constructs without the need for frozen or paraffin sectioning.

Blocking Buffer Preparation
Blocking buffer is prepared as a 1% BSA in PBS, with 0.125% Triton-X100 solution supplemented for permeabilization.

To prepare 7.5 mL of blocking buffer, add 1 mL of 7.5% fractionated BSA and 93.75 uL of 10% Triton-X solution to approximately 6.4 mL of PBS.

Immunostaining
1. Place fragments of tissue construct in a cell culture well (usually a 24 well-plate)
2. Aspirate all media from the wells.
3. Wash well once with PBS.
4. Add 4% paraformaldehyde and let incubate at room temperature for approximately 2 hours for every 1 cm thickness of the gel fragment. Thinner gels require less time.
5. Wash 3 times by adding PBS, allowing 30 – 45 minutes of incubation at room temperature, and then aspirating the PBS.
6. Add 500 uL blocking buffer to well (1% BSA and 0.125% Triton-X100 solution) and let incubate overnight at 4°C.
7. Aspirate blocking buffer.
8. Dilute primary antibody in blocking buffer (usually a 1:100 or 1:200 ratio) and add to well.
9. Incubate at 4°C overnight.
10. Wash 3 times with blocking buffer by adding buffer, waiting 30 – 45 minutes, then aspirating and replacing.
11. Add blocking buffer and let incubate at 4°C for at least 12 hours.
12. Dilute secondary antibody in PBS with 0.5% Bovine Serum Albumin and 0.125% Triton-X100 solution and add to well.
13. Let incubate at 4° C in dark overnight.
14. Wash 4 times with blocking buffer by adding buffer, waiting 30 – 45 minutes, then aspirating and replacing.
15. Add blocking buffer and let incubate at 4°C for at least 12 hours.

Optional Component for Staining of Nuclei.
Incubation and wash times may vary depending on the thickness of the tissue construct being stained. Thicker structures will require greater incubation and wash times.
1. Add 200 uL of diluted DAPI solution to the well.
2. Incubate at room temperature for 5 - 10 minutes.
3. Wash 3 times with PBS by adding PBS, allowing 10 – 20 minutes of incubation at room temperature in the dark, and then aspirating the PBS.

Chapter 2: Apply Engineered Tissue Models as a System to Enable Genetic Screens in Physiologically Relevant Settings

2.1 Abstract

Genetic screens are powerful tools for both resolving biological function and identifying potential therapeutic targets, but require physiologically accurate systems to glean biologically useful information. In this chapter, we enable genetic screens in physiologically relevant *ex vivo* cancer tissue models by integrating CRISPR-Cas-based genome engineering and biofabrication technologies. We first present a novel method for generating perfusable tissue constructs, and validate its functionality by using it to generate three-dimensional perfusable dense cultures of cancer cell lines. Results of cultures generated by our method are compared to existing 2D, 3D, and *in vivo* models by transcriptomic profiling, and using this system we enable large-scale CRISPR screens in perfused tissue cultures. Our results reveal differences across *in vitro* and *in vivo* cancer model systems, and highlight the utility of programmable tissue engineered models as a platform for screening technologies.

2.2 Introduction

The last decade has seen a number of advances in tissue engineering and biofabrication techniques that have facilitated the development of tissue and cancer models that better mimic living tissues in both structural organization and biological function[52,63,115–119]. While much of this progress is dedicated towards regenerative medicine[115,120,121], engineered tissues have also seen increased use as an avenue for therapeutic discovery[52,63,117,118,122,123]. At the most fundamental level, organoid

technologies expand upon existing cell culture techniques by incorporating 3D cell-cell interactions to recapitulate certain organ-specific functions[52,117,124–126]. Organ-chip technologies often incorporate organoid models, but further introduce elements of flow[63,118,127,128] and allow for reproduction of many biological phenomena such as tissue-tissue interface development[63,118,129,130], and cancer metastasis[63,118,131]. Meanwhile, advances in lithography[121,132], 3D printing[71,82,121,133–136], and induced neovascularization[120,137,138] have made it possible to generate perfusable networks of increasing complexity with high degrees of spatial control. Additionally, these advances have allowed for the construction of tissue models from a variety of natural and synthetic materials that are more representative of their biological counterparts in both scale[82,139] and cell density[135,140].

In parallel, there have been efforts to develop and optimize high-throughput analytic technologies such as RNAi[20,21,141] and CRISPR-based genetic perturbation screening[22,23,37,40,46,47,142–145] in order to systematically identify genetic vulnerabilities, with a prominent focus on cancer. In particular, CRISPR-screens have become an important method by which this is accomplished[20–30]. However, the majority of screens have been conducted either in 2D[20,24,27,28,34–36] or in animal models[37], and there has been a recent push to enable them in 3D systems to account for behavioral differences in a more biologically accurate environment[29,30,46,47]. Although the scale of many 3D-printed tissue constructs gives them the potential to be integrated with high-throughput screening technologies, they have rarely been used in this space. To this end, we further optimize our previously-described tissue engineering methodologies to allow for manufacturing of densely-cellularized engineered cancer models *ex vivo*, and integrate it with CRISPRko

screening technologies to assess its application in cancer diagnostics. Characterization studies indicated our model more closely mimicked *in vivo* conditions compared to existing methods of cell culture, and results of a Kinome-wide CRISPR screen suggest potential applicability in both fundamental research and translational use.

2.3 Methods

2.3.1 Printing Methodology

2.3.1.1 3D Printing of Silicone Holders and Long-Term Perfusion

Construction and long-term perfusion of flow chambers were accomplished as previously described[146]. Briefly, perfusion culture utilized a 3-component system consisting of a media reservoir, a flow chamber constructed via extrusion-printed silicone (Dow Corning Toray Sylgard SE1700), and a peristaltic pump (Watson Marlow 205U).

2.3.1.2 Spheroidal and Condensed Bud Cultures

Spheroids of MDA-MB-231 cells were formed by distributing cells into 96-well low-adhesion plates (Corning) at approximately 30,000 cells per well. Each well formed a single spheroid, allowed to condense over 72 hours before harvesting. To form condensed buds, individual wells of 48-well plates were first coated with Matrigel (5 mg/mL). Then, approximately 30,000 MDA-MB-231 cells, 30,000 HUVECs, and 7500 hMSCs were distributed into each well, and allowed to condense over 72 hours before harvesting. To harvest spheroids, wells were gently pipetted twice with a P1000 pipette to dislodge and collect the spheroid. To harvest condensed buds, a P1000 pipette tip was cut near the tip to increase the opening diameter, and used to gently pipette to dislodge

and collect the bud. Spheroids or condensed buds were then collected with media into a single centrifuge tube, allowed to settle, and then had media removed by gentle pipetting.

2.3.1.3 Preparation of Perfusable Tissue Constructs

Free-standing PVA structures were designed as previously described[146]. Briefly, geometries of interest were designed in AutoDesk Inventor, exported to the Ultimaker Cura software, and printed using the Ultimaker^3 from solid PVA filaments (Ultimaker).

A detailed description of the preparation methodology can be found in Appendix 2.7.1. Briefly, matrix solutions were prepared as previously described[146]. Matrices were formulated with Matrigel (4 mg/mL), fibrinogen (7.5 mg/mL), gelatin (10 mg/mL), transglutaminase (2 mg/mL), $CaCl_2$ (2.5 mM), and thrombin (2 U/mL). Briefly, stock solutions of gelatin, $CaCl_2$, and thrombin were prepared prior to formulation. Type A porcine skin gelatin (Sigma-Aldrich) was dissolved overnight in water (15 wt/vol %) at 70 °C, buffered to pH 7.4 using 1 M NaOH, passed through a 0.22 mm filter (Millipore), and stored at 4 °C. $CaCl_2$ was dissolved at 250 mM in Dulbecco's phosphate buffered saline (dPBS), and Thrombin (Sigma-Aldrich) was prepared at 500 U/mL, aliquoted, and stored at -20 °C. Solutions of both bovine plasma fibrinogen (Millipore) and transglutaminase (MooGloo) were dissolved in dPBS at 37 °C immediately prior to use, and at respective concentrations of 100 mg/mL and 50 mg/mL. During formulation, all components except Matrigel and thrombin were mixed and incubated at 37 °C for 20 minutes, after which Matrigel and thrombin were rapidly added. The solution was mixed, used to resuspend cells, poured into silicone single-chamber holders, and allowed to gelate over 1.5 hours. PVA was then evacuated via perfusion of warm media. For printed constructs perfused

at low flow rates (15 mL/min), perfusion was initiated immediately. For printed constructs perfused at high flow rates (>500 mL/min), the cured constructs were removed from single-chamber holders, and transferred to dual-chamber holders prior to perfusion (**Figure 2.1A**).

Endothelialization of printed constructs was achieved by resuspending HUVECs at a concentration of 5 x 10^6cells/mL, then injecting them into the lumen. Constructs were incubated for 30 minutes on either side, and left overnight to allow for adhesion before reintroducing flow.

2.3.2 Cell Culture

HUVECs and hMSCs used in the study were obtained from Lonza, and were each used until passage 10. HUVECs were cultured in EGM-2 (Lonza), and hMSCs were cultured in mesenchymal stem cell growth medium (MSCGM) (Lonza). MDA-MB-231 cells were obtained from ATCC and were cultured in DMEM supplemented with 10% FBS and 2 mM L-Glutamine. HEK293T cells were obtained from ATCC and were cultured in DMEM supplemented with 10% FBS.

2.3.3 Animal Work

$Rag2^{-/-};gc^{-/-}$ immunodeficient mice used for orthotopic breast cancer models were maintained in animal facilities at the Powell-Focht Bioengineering Hall at the University of California San Diego. All experiments were performed in accordance with national guidelines and regulations, and with the approval of animal care and use committees at

Sanford Burnham Prebys Medical Discovery Institute and the University of California San Diego.

2.3.4 Model Growth

2.3.4.1 2D, 3D, and In Vivo Culture of MDA-MB-231 Cells

MDA-MB-231 cells were harvested and distributed into 2D monolayer culture, static matrix, perfused print, or orthotopic mammary tumor conditions, and allowed to grow over 4 weeks. Perfused prints were prepared as previously described in a blend of Matrigel (4 mg/mL), fibrinogen (7.5 mg/mL), and gelatin (10 mg/mL). Cells selected for prints were distributed into low-adhesion 96-well plates (Corning) with approximately 30,000 cells per well. Spheroids were allowed to congregate for 72 hours, after which they were harvested and encapsulated within their respective growth environments along with hMSCs at respective densities of 1×10^6 cells/mL and 2.5×10^5 cells/mL. Perfused prints prepared in the absence of hMSCs or HUVECs were prepared identically, but without the addition of hMSCs and with no endothelialization. Static matrices were prepared identically, but without the subsequent perfusion. Cells selected for orthotopic tumor conditions were resuspended in a 1:1 mixture of Matrigel and EGM-2, and were injected either into the mammary fat pad[147] of female anesthetized $Rag2^{-/-};gc^{-/-}$ immunodeficient mice.

2.3.5 Model Analysis

2.3.5.1 Cell Density Calculations

For cell density comparisons, wet mass values for matrices, prints, and tumor fragments were obtained using a mass balance. Cells were then isolated from their matrix environments using a combination of Dispase II solution and the Miltenyi Tumor Dissociation Kit as described previously. Living cells were then counted using the Trypan Blue assay, and density was calculated based on the number of living cells and the final wet mass for each replicate.

2.3.5.2 Spreading Analysis

MDA-MB-231 cells were harvested and encapsulated in static matrices on a glass cover-slip-bottomed plate (MakTek), either with or without the addition of hMSCs. Matrices were prepared as a blend of Matrigel (4 mg/mL), fibrinogen (7.5 mg/mL), and gelatin (10 mg/mL). Cells were encapsulated at densities of 1×10^6 cells/mL for MDA-MB-231, and 2.5×10^5 cells/mL for hMSCs. Cells were grown in static matrix culture for 6 days, after which they were either imaged directly via confocal microscopy, or fixed, stained for F-actin, and then imaged. For quantitative elongation and spreading analysis, length and width measurements of individual cells were obtained in ImageJ.

2.3.5.3 Actin Staining

To stain for F-actin, matrices containing MDA-MB-231 cells were fixed in paraformaldehyde (4%) for 1 h, washed with three rinses of PBS for 30 min each, and blocked overnight using a solution of bovine serum albumin (BSA) (1%) and Triton-X100

(0.125) in PBS. Constructs were then subject to an overnight incubation with Alexa-594 phalloidin (Thermofisher) in blocking buffer at 4 °C, followed by an overnight wash with PBS.

2.3.5.4 Imaging

Widefield fluorescent microscopy images were obtained using the Leica DMi8 microscope at 10X magnification with a resolution of 0.1118 mm. Confocal images were obtained using the Zeiss 880 Airyscan Confocal.

2.3.6 Genetic and Transcriptomic Analysis

2.3.6.1 Extraction of RNA from MDA-MB-231 Cells for Transcriptomic Analysis

Snap-frozen cells had RNA extracted directly using the RNeasy Kit (Qiagen). Matrices were cut into <1 mm pieces, resuspended in Dispase II solution, and placed on a shaker at 60 rpm at 37 °C for 1 hour. The solution was then centrifuged at 300g for 5 minutes and supernatant was removed. The remaining cells and matrix fragments were then resuspended in a digestion solution provided by the Miltenyi Tumor Dissociation Kit and placed on a shaker at 60 rpm at 37 °C for 1 hour. To collect cells following all matrix digestions, solutions were centrifuged at 300g for 5 minutes, and supernatant was aspirated. RNA was then extracted using the RNeasy Kit.

Following RNA extraction, approximately 500 ng of RNA from each condition was used to synthesize cDNA using the NEBNext poly(A) mRNA Magnetic Isolation Module (New England Biosystems). Libraries were then constructed and indexed using the NEBNext Ultra II RNA Library Prep Kit (New England Biosystems) and NEB Multiplex

Primers. The final product was purified using 1.0x Ampure XP beads, pooled in equal ratios, and sequenced using the NovaSeq with either paired end 250 bp reads or paired end 100 bp reads.

2.3.6.2 Kinome-Wide CRISPR Knockout Screen

The Brunello Human Kinome CRISPR Knockout Library[148] (Addgene 75314) was transformed into Stbl4 chemically competent Escherichia coli (Invitrogen), which were subsequently incubated overnight at 37 °C in 100 mL of carbenicillin (50 mg/mL). Plasmid DNA was then extracted with a QIAprep Spin Maxiprep Kit (Qiagen).

To create individual validation constructs, the LentiCRISPR v2 plasmid[145] (Addgene 52961) was digested via BSMB1, and individual guide sequences were inserted by Gibson assembly. Resulting plasmids were transformed into Stbl3 chemically competent Escherichia coli, which were plated on carbenicillin (50 mg/mL) LB plates and incubated for 18 hours at 37 °C. Colonies were individually transferred into 5 mL of carbenicillin (50 mg/mL), and plasmid DNA was extracted with a Qiaprep Spin Miniprep Kit (Qiagen). A detailed description of the methodology can be found in Appendix 2.7.3.

To produce lentivirus particles, 36 mL of Lipofectamine 2000 (Life Technologies) was added to 1.5 mL of Opti-MEM (Life Technologies), while 3 mg of pMD2.G (Addgene 12259), 12 mg of pCMV delta R8.2 (Addgene 12263), and either 12 mg of the pooled vector library or 9 mg of a single guide construct were added to a separate 1.5 mL of Opti-MEM. Both solutions were incubated for 5 minutes at room temperature, after which they were mixed and allowed to incubate for an additional 30 minutes. This final transfection solution was added dropwise to a 15 cm tissue culture dish of HEK 293T cells at

approximately 60% confluency prior. Notably, a single solution of this composition was used to transfect a single 15 cm dish. Supernatant was collected after 48 and 72 hours, filtered through 0.45 mm Steriflip filters (Millipore), and concentrated using Amicon Ultra-15 centrifugal ultrafilters (Millipore). Final viral solutions were aliquoted and stored long-term at -80 °C. A detailed description of the methodology can be found in Appendix 2.7.2.

For viral transduction, MDA-MB-231 cells were grown to approximately 30% confluency on 15 cm tissue culture dishes, and supplemented with medium containing polybrene (8 mg/mL, Millipore) and enough viral particles to produce a 0.3 MOI. After 24 hours, medium was replaced. After an additional 24 hours, selection was initiated by supplementing medium with puromycin (4 mg/mL, Millipore). Selection was allowed to continue for 24 hours, after which cells were harvested and distributed into one of seven conditions. Replicates for each condition contained a minimum of 3 million cells each to achieve approximately 1000-fold library coverage. Cells selected for cell culture conditions were passaged immediately onto tissue culture plates. Cells selected for orthotopic tumor conditions were resuspended in a 1:1 mixture of Matrigel and EGM-2, and were respectively injected into the mammary fat pad[147] of anesthetized $Rag2^{-/-};gc^{-/-}$ immunodeficient mice. Cells selected for perfused print conditions were distributed into low-adhesion 96-well plates (Corning) with approximately 30,000 cells per well. Spheroids were allowed to congregate for 72 hours, after which spheroids selected for static matrix or either of two perfused print conditions were harvested and encapsulated within their respective growth environments.

2.3.6.3 Extraction and Processing of gDNA for Screen Analysis

Genomic DNA was directly extracted from cell culture samples via the DNeasy Blood and Tissue Kit (Qiagen). For perfused print and tumor samples, cells were first isolated from their matrix environments. Matrices or tissue were cut into < 1 mm fragments, then resuspended in Dispase II solution (Millipore) and incubated at 37 °C on a shaker at 60 rpm for 1.5 hours. The solution was then centrifuged for 5 minutes at 300g, supernatant was aspirated, and the remaining cells and matrix fragments were resuspended in the digestion solution provided by the Miltenyi Tumor Dissociation Kit (Miltenyi Biotec) and incubated at 37 °C on a shaker at 60 rpm for 1.5 hours. The solution was then centrifuged for 5 minutes at 300g, and supernatant was aspirated. DNA was then extracted from the remaining cells via the DNeasy Blood and Tissue Kit (Qiagen).

Guide RNA sequences were amplified using Kapa Hifi HotStart polymerase (Roche). Primer sequences used for the amplification can be found in Appendix 2.7.4.An approximately 350 bp fragment was amplified in the PCR 1 reaction using primers containing the Illumina adaptor sequences, with input quantities achieving 1000-fold coverage. Of note, conditions without enough cells or DNA to account for a minimum 500-fold coverage were not processed further. Amplicons were purified using the PCR Purification Kit (Qiagen), and 50 ng of product was transferred to the PCR 2 reaction. Amplicons from the knockout library samples were indexed using either NEBNext Single Index Oligos for Illumina (New England Biosystems) or NEBNext Multiplex Oligos for Illumina kit (New England Biosystems). The final product was purified using 1.2x volume of Ampure XP beads, mixed in equal ratios, and sequenced on either the HiSeq4000 or NovaSeq with single end 75 bp reads or paired end 100 bp reads respectively. Amplicons

from validation samples were indexed using NEBNext Multiplex Oligos for Illumina kit (New England Biosystems). The final product was purified using 1.0x volume of Ampure XP beads, mixed in equal ratios, and sequenced on the NovaSeq with paired end 250 bp reads.

2.3.7 Computational Analysis

2.3.7.1 Computational Analysis of Kinome-Wide Knockout Library Data

For 250 bp runs, raw reads within FASTQ files were trimmed to 100bp to remove any 3' adapter sequences. Reads were aligned to both reference genomes HG38 and mm10 using STAR[149], and mouse read contamination was removed using XenofilteR[150]. Read counts were generated by mapping to reference transcriptome GenCode v33 using FeatureCounts. Read counts were normalized in DESeq2 both across all samples for a given gene using the geometric mean, and within each sample using the median. Relative expression profiles and differentially expressed gene lists were subsequently generated using the DESeq2 pipeline. Hierarchical clustering between replicates was performed based on the average distance in relative expression levels of all expressed genes across replicates. Principal component analysis was performed using relative expression levels of all genes across replicates. Enriched and depleted pathways were identified using Metascape[151]. Differentially expressed genes with both |Zscore| > 1.5 and FDR < 0.1 were input into Metascape, and pathway lists were restricted to terms within the Gene Ontology Biological Process domain.

2.3.7.2 Comparison to DepMap Data

The raw readcount file and guide map (DepMap Public 19Q3) associated with the AVANA dataset was downloaded from the DepMap website. Genome-wide data for two experimental replicates for MDA-MB-231 cells was processed in MAGeCK and compared to plasmid data to calculate gene-level log_2fold changes. Log_2fold change data for all genes overlapping with those of the Brunello Human Kinome CRISPR Knockout Library was then extracted and compared to equivalent data from our week 3 samples. The resulting correlational comparison was used to calculate a coefficient of determination.

2.3.7.3 Statistical Analysis

Statistical parameters (mean, standard deviation) for all data shown in bar graphs were processed using GraphPad Prism v7.0. Direct statistical comparisons where indicated were conducted using a two-sided t-test. Samples used in the data are biological replicates. Hierarchical clustering for RNA-seq data was performed in R using the DESeq2, stats, genefilter, and pheatmap packages. Clustering was performed using the Pearson Correlation as the measure of distance, and the Average Distance as the method. Principal component analysis for both RNA-seq and CRISPR screening data was performed in R using the Stats package. For CRISPR screening data, all log_2fold measurements were normalized as Z-scores prior to analysis. Correlational comparisons, linear regressions, and calculations of coefficients of determination (R^2) for all CRISPR screening datasets was performed in MATLAB.

2.4 Results and Discussion

2.4.1 Perfused MDA-MB-231 tumor models show greater similarities to in vivo tumors compared to 2D cell culture and static 3D culture

While CRISPRko screens are useful in a cancer-therapeutic context, they have traditionally been conducted in 2D monolayer culture[20–30], which often fails to replicate many features of tumor biology[152]. As such, we sought to engineer a tissue construct that would allow for multi-week support of model tumor systems *ex vivo*, as well as promote growth at a scale that would permit large-scale genetic screening. In the previous chapter, we developed a methodology for creating a system that allowed for multi-week *ex vivo* support, but was limited in its degree of promoting growth, due to limitations in flow rate. A modified workflow for the fabrication of perfused tissue constructs is outlined in **Figure 2.1A**. Specifically, first a sacrificial poly(vinyl alcohol) (PVA) scaffold is printed in a desired geometry and inserted into a silicone holder. A cell-loaded matrix generated from biologically-derived materials[146] is then used to encapsulate the scaffold. The matrix formulation is allowed to gelate, while the PVA scaffold slowly dissolves. A lumen is then formed via evacuation of the dissolved PVA scaffold using warm media. At this stage, the construct is perfusable, but is also sealed on all four sides. Next, to allow for higher flow rates, the construct is removed from the holder, and placed within an open chamber into which excess fluid can flow before being channeled through an outlet. This format makes it possible to sustain flow rates exceeding 1 mL/min, inducing physiological shear stresses exceeding 1 dyne/cm^2. Furthermore, the higher pressure generated from the higher flow rates can introduce interstitial flow into the system, emulating what is also seen in tumor tissues, and enables perfusion of the surroundings of the construct in

addition to direct perfusion of the lumen. Indeed a direct comparison between lower (15 μL/min) and higher (1 mL/min) flow rates resulted in a ten-fold increase in the growth of MDA-MB-231 breast cancer cells over the course of 15 days (**Figure 2.1B).**

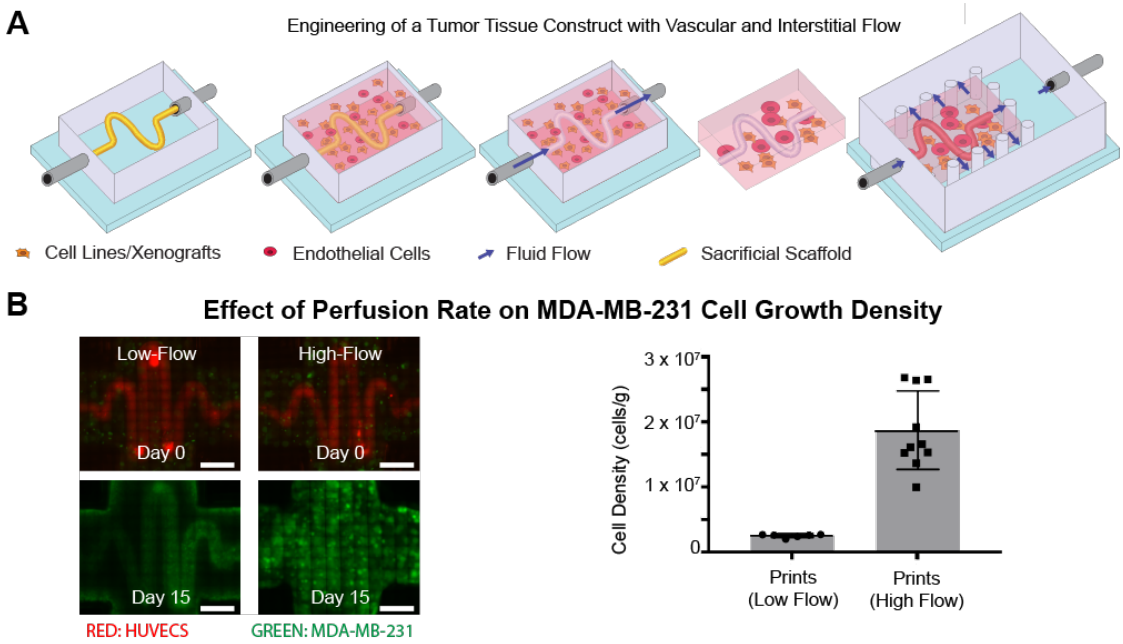

Figure 2.1: 3D-Printing of Perfused Tissue Constructs. (A) Schematic representation of the perfusable construct manufacturing procedure. A PVA scaffold of desired geometry is printed and inserted into a silicone holder. The PVA scaffold is then encapsulated within a matrix formulation of desired composition. The matrix formulation is allowed to gelate and simultaneously, the PVA scaffold slowly dissolves. The scaffold is then evacuated using warm media. At this stage, the construct can be perfused, though nutrients will be distributed only by diffusion. The construct is then removed from the holder, and placed into the chamber of a larger silicone construct that allows for open perfusion on all sides. At this stage, interstitial flow may be introduced, and perfusion is possible around as well as within the construct. **(B)** Fluorescent images (left) showing the growth of GFP-labeled MDA-MB-231 cells in matrices at low flow rates without interstitial flow (15 uL/min) and high flow rates with interstitial flow (500 uL/min). Scale bars: 2 mm. Cell density counts (right) for MDA-MB-231 cells in matrices at low flow rates (n = 6) and high flow rates (n = 10). Error bars show standard deviation.

We next optimized media and loading conditions to allow for co-culture of MDA-MB-231 cells with human umbilical vein endothelial cells (HUVECs) and human mesenchymal stem cells (hMSCs) serving as pericytes. In particular, hMSCs are known to play a role in shaping the tumor microenvironment and promoting key characteristics such as proliferation and motility[153]. MDA-MB-231 cells, HUVECs, and hMSCs were

grown in a variety of media conditions containing DMEM, EGM-2, MSCGM, or mixtures of DMEM with either medium, all supplemented with FBS. Qualitative images and quantitative measurements via the CCK8 reagent (**Figure 2.2A-C**) both indicated that growth in EGM-2 with 10% FBS would allow for co-culture with HUVECs and hMSCs without negatively impacting MDA-MB-231 growth.

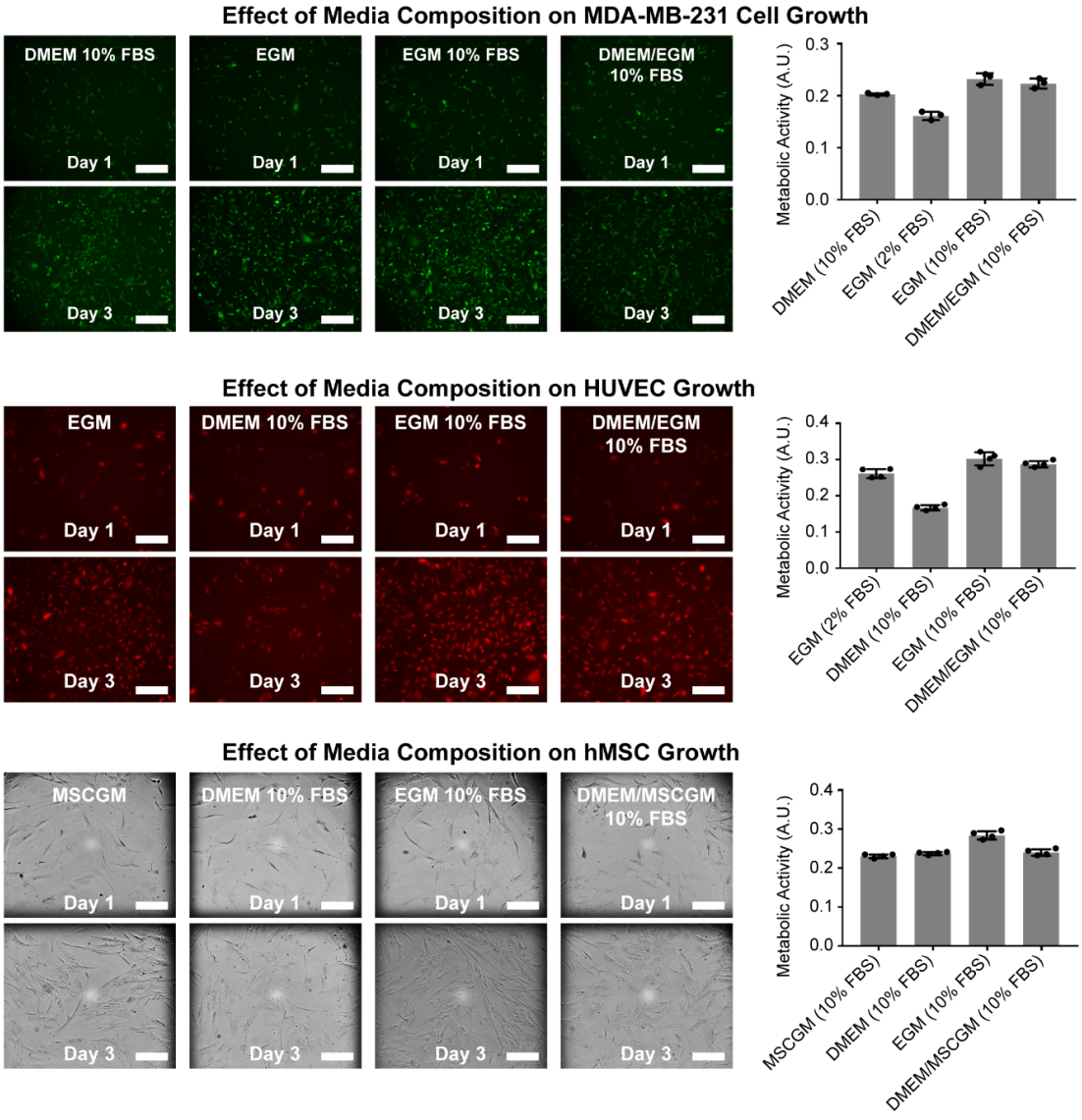

Figure 2.2: Optimization of culture conditions for an ex vivo model of breast cancer. Widefield microscopy images (left) and metabolic activity measurements (right) of **(A)** GFP-labeled MDA-MB-231 cells, **(B)** HUVECs, and **(C)** hMSCs, grown under various media compositions. Scale bars: 250 μm (n = 3). Error bars show standard deviation.

To assess the impact of hMSCs on the proliferative and migratory capacity, MDA-MB-231 cells were cultured in the presence of hMSCs at a 4:1 ratio over 6 days, and examined for spreading and elongated morphologies, both known indicators of the cytoskeletal remodeling associated with increased migratory behavior[154]. MDA-MB-231 cells cultured with hMSCs showed greater degrees of spreading morphology (**Figure 2.3A**) compared to controls, with individual cells displaying more elongated morphologies (**Figure 2.3B**), confirmed with confocal images (**Figure 2.3C**) and visualization of F-actin distribution **(Figure 2.3D**). To determine optimal 3D loading conditions, MDA-MB-231 cells were encapsulated in perfused prints either alone as spheroids or with HUVECs and hMSCs as condensate organoid buds[126] (**Figure 2.3E**). After 10 days of culture, qualitative images suggested significantly greater growth when loaded as spheroids (**Figure 2.3F**).

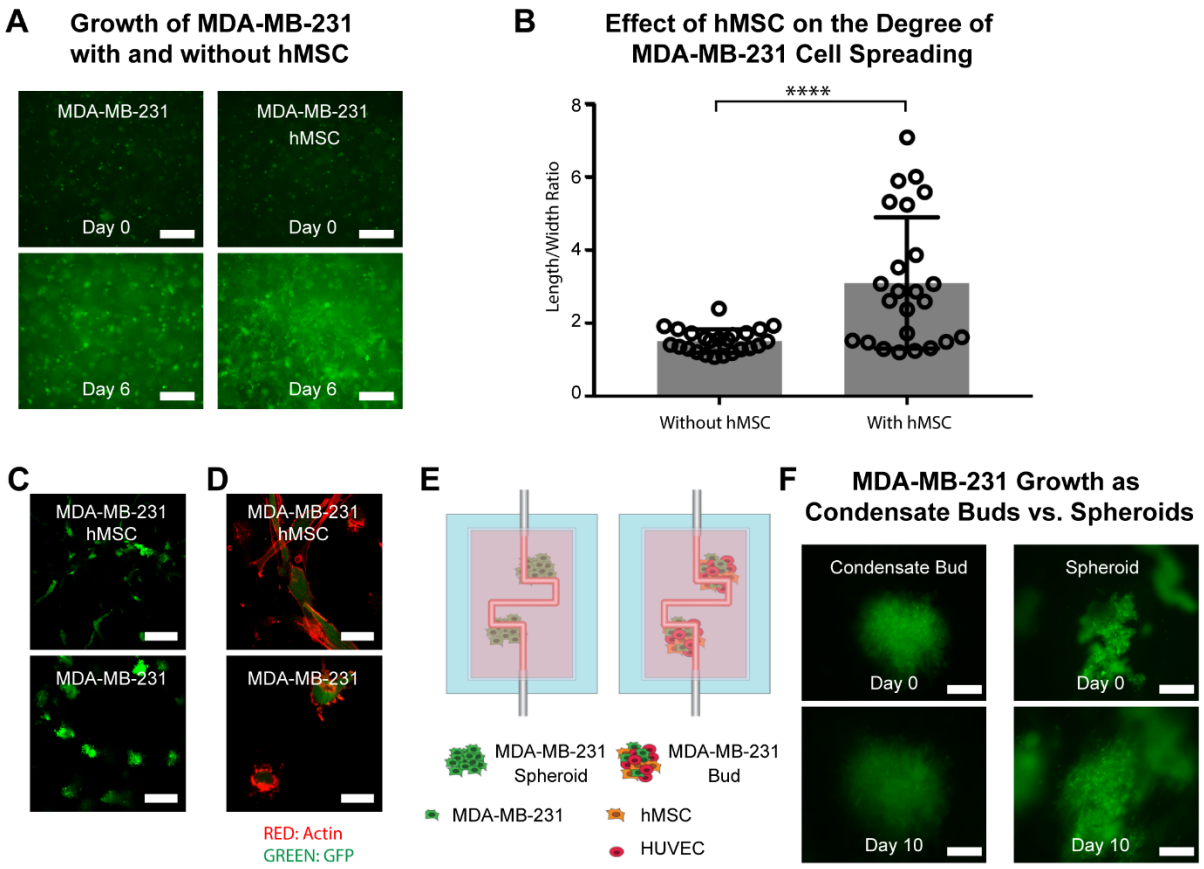

Figure 2.3: Analysis of the effects of mesenchymal stem cells and encapsulation conditions. (A) Fluorescent widefield images comparing spreading behavior of GFP-labeled MDA-MB-231 cells when grown in 3D with and without hMSCs. Scale bars: 250 um. **(B)** Measurement of MDA-MB-231 cell spreading as a ratio of cell length and width, with and without the presence of hMSCs. **(C)** Confocal images comparing spreading behavior of GFP-labeled MDA-MB-231 cells when grown in 3D with and without hMSCs. Scale bars: 80 um. **(D)** Confocal images showing actin distribution in MDA-MB-231 cells when growth in 3D with and without hMSCs. Scale bars: 30 um. **(E-F)** Schematic diagram showing experimental setup for, and fluorescent images comparing relative growth of GFP-labeled MDA-MB-231 cells when encapsulated within perfused printed constructs as either lone spheroids, or condensate organoid buds with HUVECs and hMSCs.

To assess the ability of the optimized system to emulate the *in vivo* tumor environment, we next performed a gene expression analysis comparing MDA-MB-231 cells grown *in vivo* to those grown in 2D monolayer culture, 3D static matrix culture, and our perfused tissue constructs (**Figure 2.4A**). Towards this, MDA-MB-231 cells were grown over a period of 4 weeks in orthotopic MDA-MB-231 mammary tumors, 2D cell

culture, static matrices, or perfused printed constructs, after which RNA was extracted. Of note, because of potential transcriptomic interference from HUVECs and hMSCs present alongside the MDA-MB-231 cells in perfused culture, additional perfused prints were prepared without either cell type present. Transcriptomic profiles were generated through bulk-RNA sequencing, followed by STAR alignment[149] and analysis with the DESeq2 pipeline[155]. Hierarchical clustering was performed across all expressed genes across the four conditions, and showed closer alignment of tumors and perfused print conditions compared to both static matrices and 2D cell culture (**Figure 2.4B**).

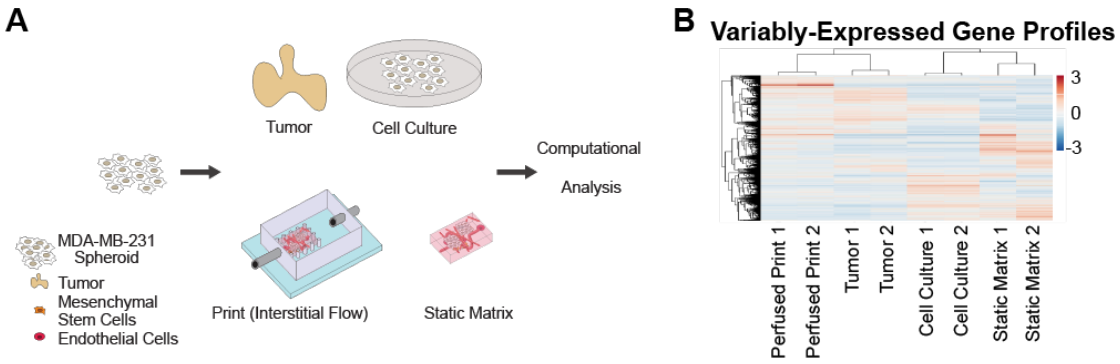

Figure 2.4: Transcriptomic Profiling of MDA-MB-231 Tumor Models. (A) Schematic representation of MDA-MB-231 culture conditions. MDA-MB-231 cells are distributed across four conditions: 2D-cell culture, static matrices, perfused printed constructs, and tumors in mice injected orthotopically in the mammary fat pad. Conditions are sustained over 2 weeks, after which RNA is extracted, amplified, and sequenced. **(B)** Hierarchical clustering diagram comparing relative transcriptomic profiles of all expressed genes in MDA-MB-231 cells grown in various conditions (n = 2 for each condition).

At a pathway-level, differentially expressed genes were compared between all four conditions, identified through DESeq2. Genes were categorized as either highly enriched or highly depleted if they possessed both a |Zscore| > 1.5, and an FDR < 0.1. Metascape was used to perform pathway-enrichment analysis within the Gene Ontology Biological Processes domain. Notably, the perfused print condition showed a substantially lower

number of differentially expressed genes relative to tumor conditions than the 2D cell culture or static matrix conditions (**Figure 2.5A**).

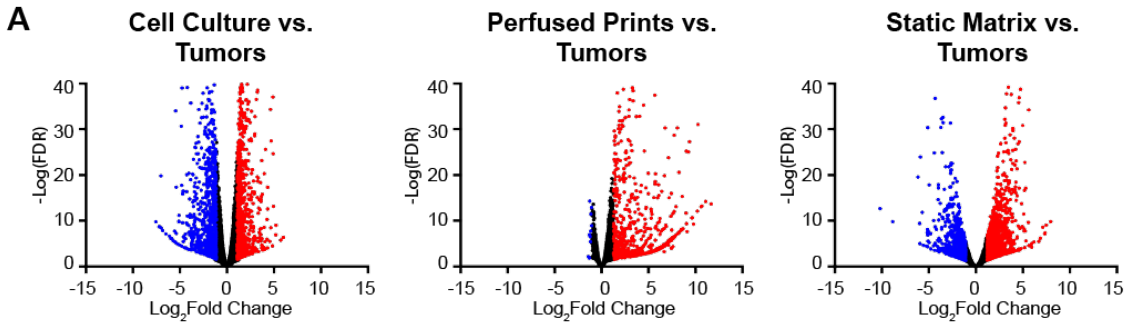

Figure 2.5: Comparison of differentially expressed genes of MDA-MB-231 cells cultured ex vivo in various conditions. (A) Comparison of differentially expressed genes in MDA-MB-231 cells when grown in cell culture, perfused print, and static matrix conditions, relative to orthotopic tumor conditions.

Differentially expressed pathways in both perfused print and tumor conditions relative to 2D cell culture (**Figure 2.6A**) and 3D static matrices (**Figure 2.6B**) were identified, and both perfused print and *in vivo* conditions were found to share a number of enriched and depleted pathways of interest[156,157]. Of note, when comparing the top 20 enriched pathways in both conditions relative to cell culture, over 50% were shared, including those associated with the biological processes of extracellular matrix organization, cell adhesion, and cell proliferation, all key differences that may arise in a 3D growth environment. Similarly, when comparing relative to static matrices, over 50% were shared, including those associated with extracellular matrix organization, locomotion, cell adhesion, and cell junction organization. Furthermore, both were enriched in pathways of growth factor response and transmembrane receptor-protein tyrosine kinase signaling, both prominent in cancer progression.

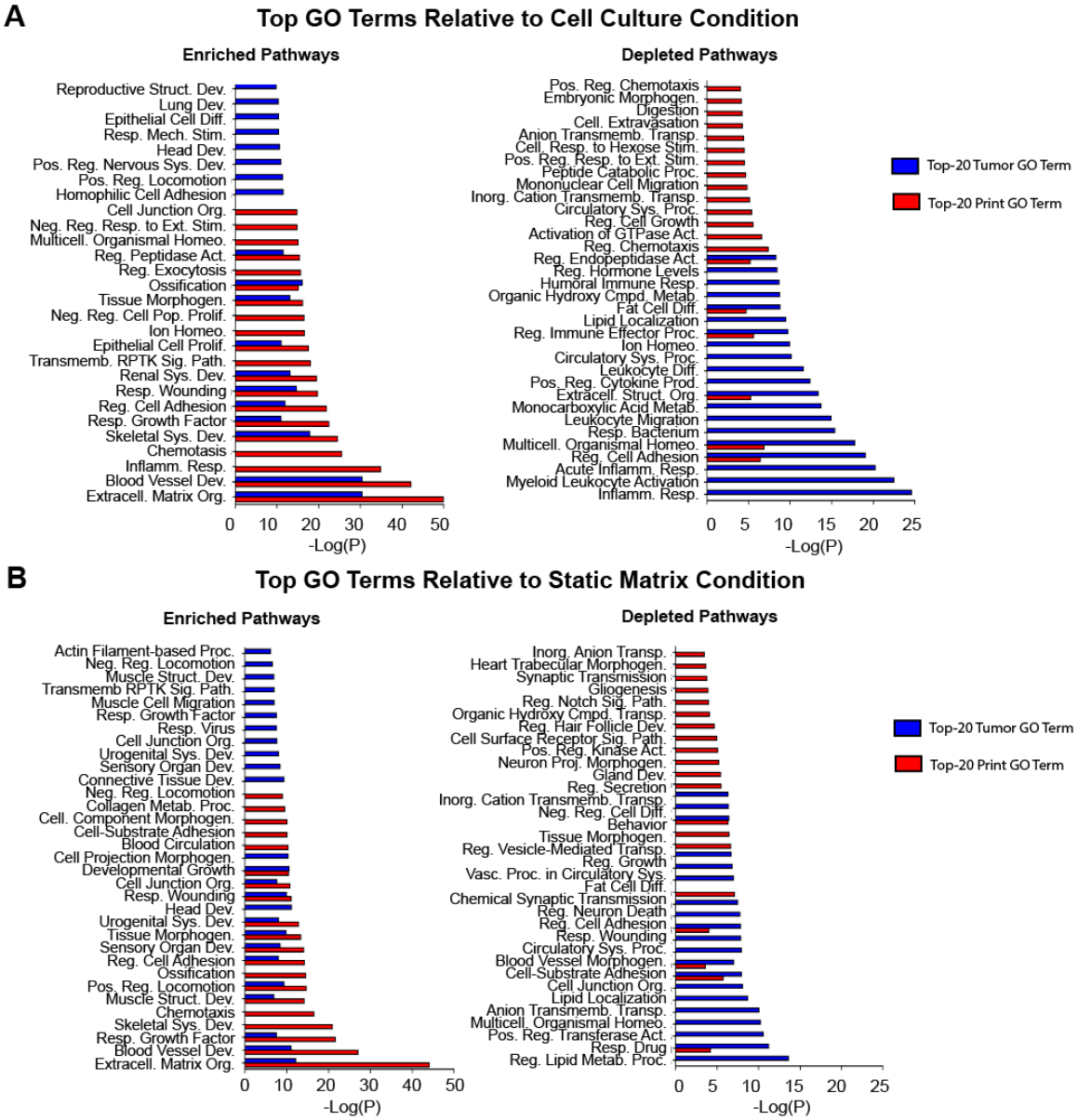

Figure 2.6: Enriched Pathway Comparisons in MDA-MB-231 Tumor Models. (A) Top-20 Metascape-generated enriched (left) and depleted (right) Gene Ontology Biological Process Pathways that are shared by perfused print and tumor conditions in comparison to the cell culture condition. **(B)** Top-20 Metascape-generated enriched (left) and depleted (right) Gene Ontology Biological Process Pathways that are shared by perfused print and tumor conditions in comparison to the static matrix condition.

In comparing the standard perfused prints to those without hMSCs or HUVECs, their transcriptomic profiles clustered most closely to each other as expected, and both were more similar to tumors than either non-perfused condition **(Figure 2.7A-B)**. This

was expected, as the two conditions share all features save the presence of the HUVECs and hMSCs, both of which are minor populations relative to the MDA-MB-231 cells. In terms of pathways, a number of pathways that would be expected to be associated with hMSCs and HUVECs were predictably enriched in the condition that contained them, such as blood vessel development and ECM organization (**Figure 2.7C**).

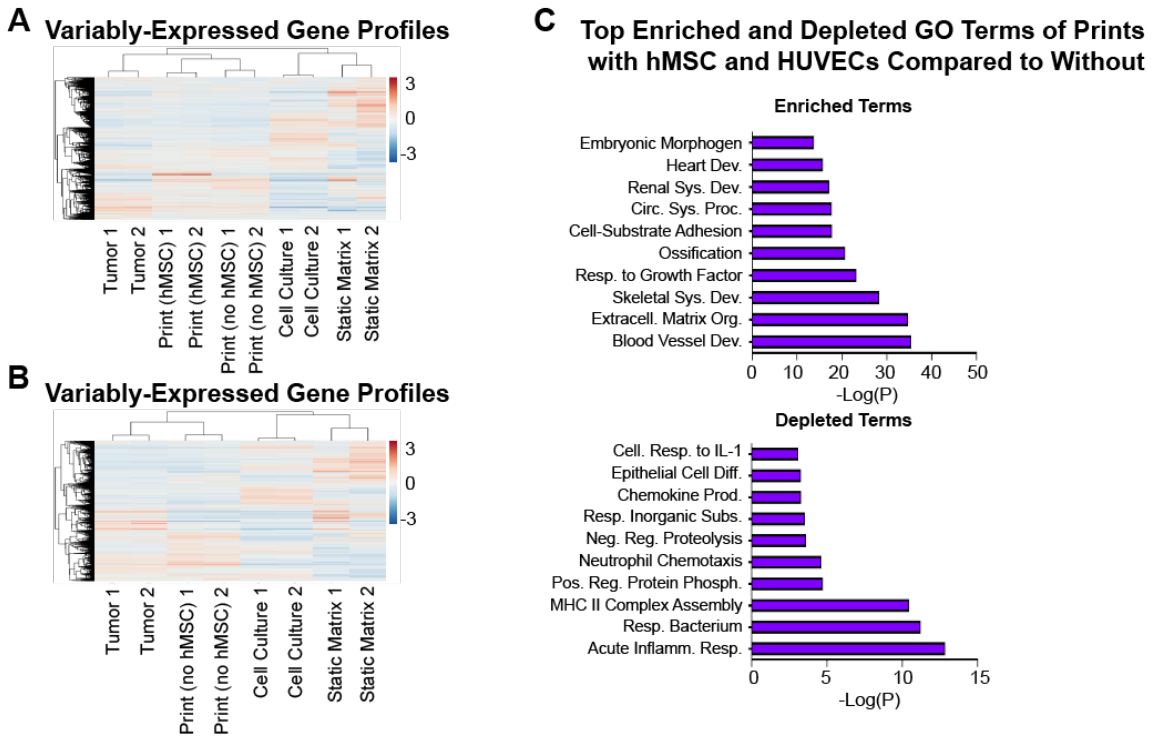

Figure 2.7: Transcriptomic comparison of MDA-MB-231 cells cultured with and without hMSCs and HUVECs. (A) Hierarchical clustering diagram comparing relative transcriptomic profiles of all expressed genes in MDA-MB-231 cells grown in cell culture, static matrix, perfused print, perfused print without HUVECs or hMSCs, and orthotopic tumors (n = 2 for each condition). **(B)** Hierarchical clustering diagram comparing relative transcriptomic profiles of all expressed genes in MDA-MB-231 cells grown in cell culture, static matrix, perfused print without HUVECs or hMSCs, and orthotopic tumors (n = 2 for each condition). **(C)** Top-10 Metascape-generated enriched and depleted Gene Ontology Biological Process Pathways in perfused prints with HUVECs and hMSCs relative to perfused prints without HUVECs or hMSCs.

However, when compared to 2D cell culture, both conditions shared 60% of their top-20 enriched pathways, including most of the prominent pathways originally shared with the tumor condition, such as those associated with ECM organization, blood vessel development, cell adhesion, and cell proliferation (**Figure 2.8A**). While the extent of enrichment is greater in the presence of the HUVECs and hMSCs, the degree of similarity indicates that the presence of these cell types may not be essential for replicating key tumor characteristics. Overall however, this data suggests that regardless of the presence of hMSCs and HUVECs, the perfused model was more transcriptomically similar to *in vivo* conditions.

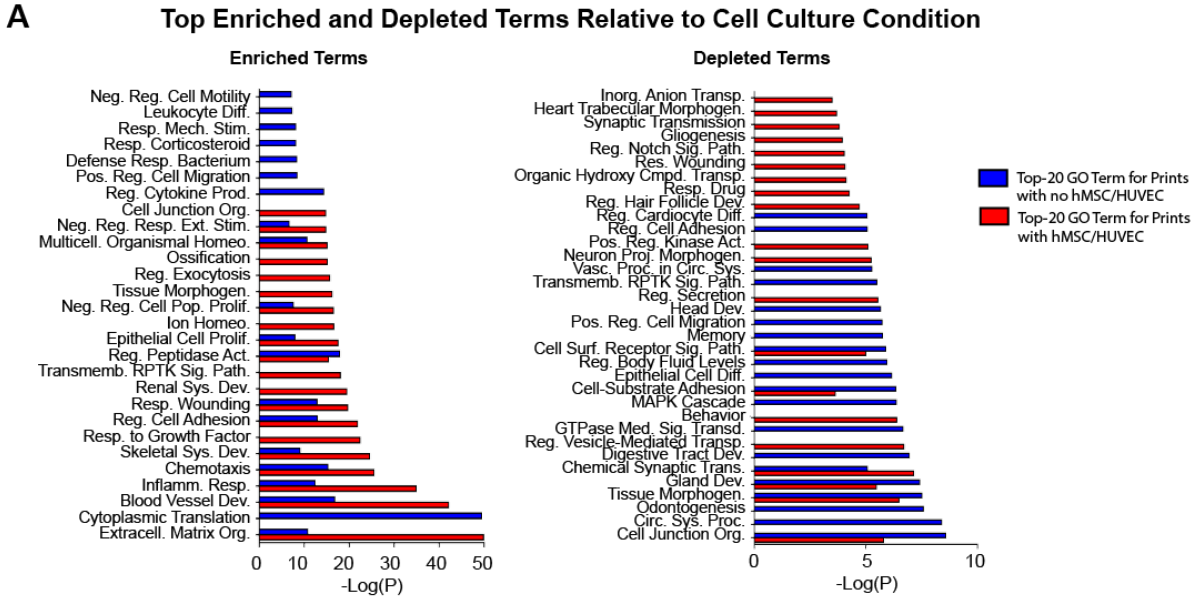

Figure 2.8: Transcriptomic comparison of MDA-MB-231 cells cultured with and without hMSCs and HUVECs. (D) Top-20 Metascape-generated enriched (left) and depleted (right) Gene Ontology Biological Process Pathways in perfused print conditions with hMSCs and HUVECs and perfused print conditions without hMSCs or HUVECs, both compared to cell culture conditions.

2.4.2 A Kinome-wide CRISPRko screen reveals shared vulnerabilities in perfused MDA-MB-231 tumor models and in vivo tumors

Having established a platform for better emulation of *in vivo*-like conditions, we then integrated the system with genetic screening technologies as a means to systematically identify genetic vulnerabilities in cancers. We again incorporated the MDA-MB-231 cell line in our system as a model for breast cancer, and compared the model to 2D and orthotopic MDA-MB-231 mammary growth conditions towards enabling more biologically relevant genetic screens. We initiated a CRISPRko screen by transducing MDA-MB-231 cells with a 3152-element subset of the Brunello CRISPRko library, encompassing 763 genes of the kinome[158]. A portion of the transduced cells was harvested and frozen at Day 3, while the rest were split across 2D-cell culture, perfused printed constructs, and orthotopic mammary tumor growth conditions. A full workflow is shown in **Figure 2.9A**. Replicates for all conditions were loaded with at least 3 x 10^6 cells each to achieve 1000-fold coverage at initial onset, and cells in all conditions were allowed to grow for 4 weeks. Genomic DNA from all samples was subsequently extracted, sequenced, and analyzed using the MAGeCK pipeline[159].

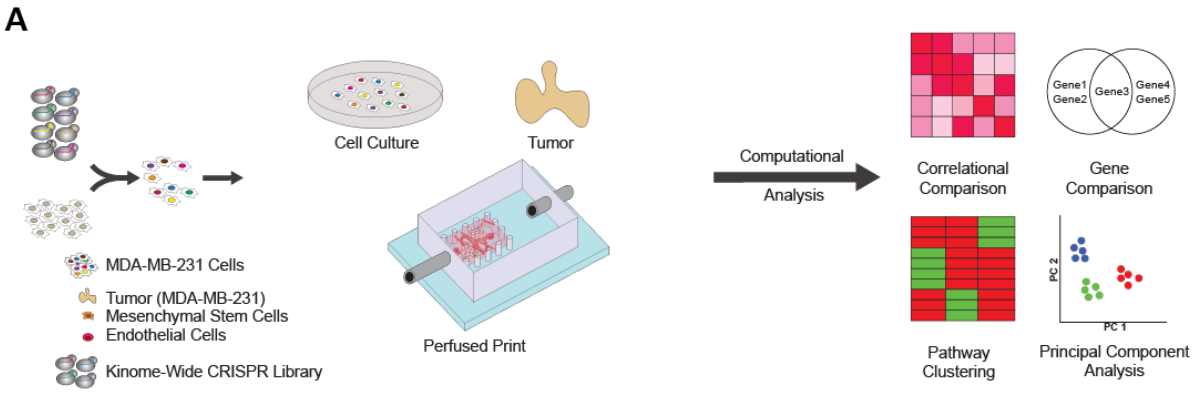

Figure 2.9: Kinome-wide CRISPRko screens in MDA-MB-231 cells cultured in in vitro 2D conditions, in the ex vivo perfused 3D model, and in in vivo orthotopic locations in mice. (A) Schematic representation of the kinome-wide CRISPR knockout screen. MDA-MB-231 cells are lentivirally transduced with a 3152-element CRISPR knockout library. Cells are collected and distributed across three conditions: 2D-cell culture, perfused printed constructs, and tumors in mice injected orthotopically in the mammary fat pad. Conditions are sustained over 4 weeks, after which gDNA is extracted, amplified, sequenced, and processed.

To confirm data efficacy, log_2fold change measurements at the gene-level for all genes were compared between Day-21 cell culture samples and the publicly available DepMap dataset (AVANA v.19Q3) for MDA-MB-231 cells[36] (**Figure 2.10A**).

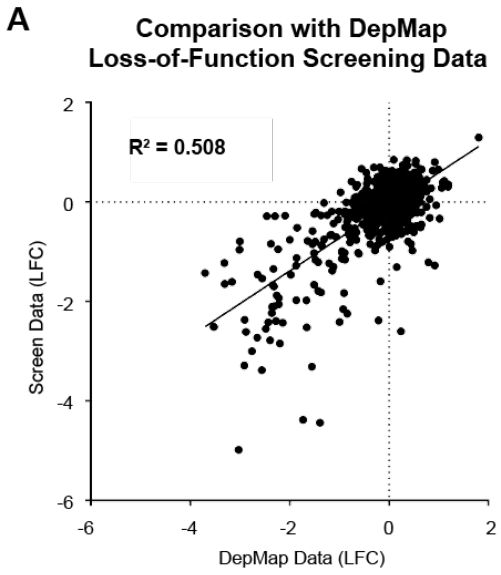

Figure 2.10: Comparison of Kinome-wide CRISPRko screening results to existing data. (A) Correlational comparison of log_2fold change behavior of 763 kinase genes in MDA-MB-231 cells cultured over 3 weeks. Comparison is made between kinome-library experiment, and public DepMap data.

To contrast enrichment and depletion behavior across groups within our study, hierarchical clustering was performed based on log_2fold change measurements of all top hit genes (p-value < 0.0027) across all conditions **(Figure 2.11A)**. Notably, results indicated that perfused print conditions clustered better with mammary tumor conditions compared to cell culture, and as expected, replicates of a given condition tended to cluster together first. A principal component analysis performed across top hit genes for all replicates (**Figure 2.11B**) further reinforced the aforementioned patterns.

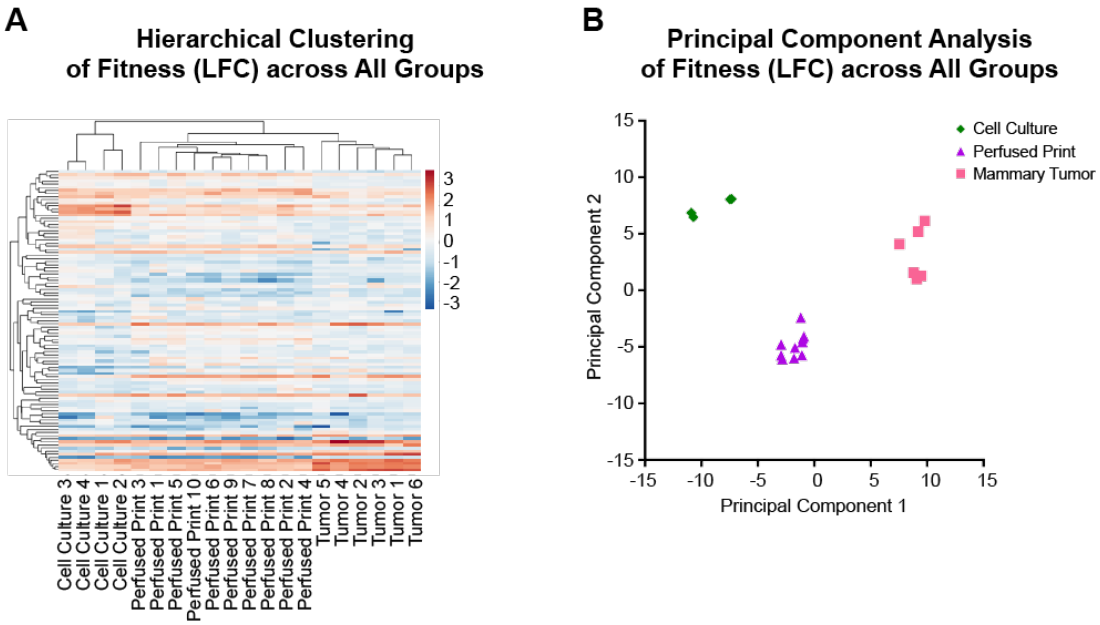

Figure 2.11: Comparison of Fitness Data from Kinome-wide CRISPRko screens in MDA-MB-231 cells across conditions (I). (A) Results of hierarchical clustering performed for top hit genes of all individual replicates for each treatment condition. **(B)** Results of a principal component analysis performed across all genes of all individual replicates for each treatment condition.

When samples were correlated based on log_2fold change in paired comparisons across replicates of all conditions, perfused prints correlated better with mammary tumor conditions compared to cell culture (**Figure 2.12A**). When comparing top depletion and enrichment hits between cell culture, mammary tumor, and perfused print conditions

(**Figure 2.12B**), results clearly showed that mammary tumors shared a much greater number of hits with perfused prints compared to cell culture, though the cell culture condition had the greatest number of unique hits overall. Upon performing pathway-enrichment analysis on the top-20 depleted terms of each condition within the Gene Ontology Biological Process domain, this trend was reinforced[156,157] (**Figure 2.13A**)[151].

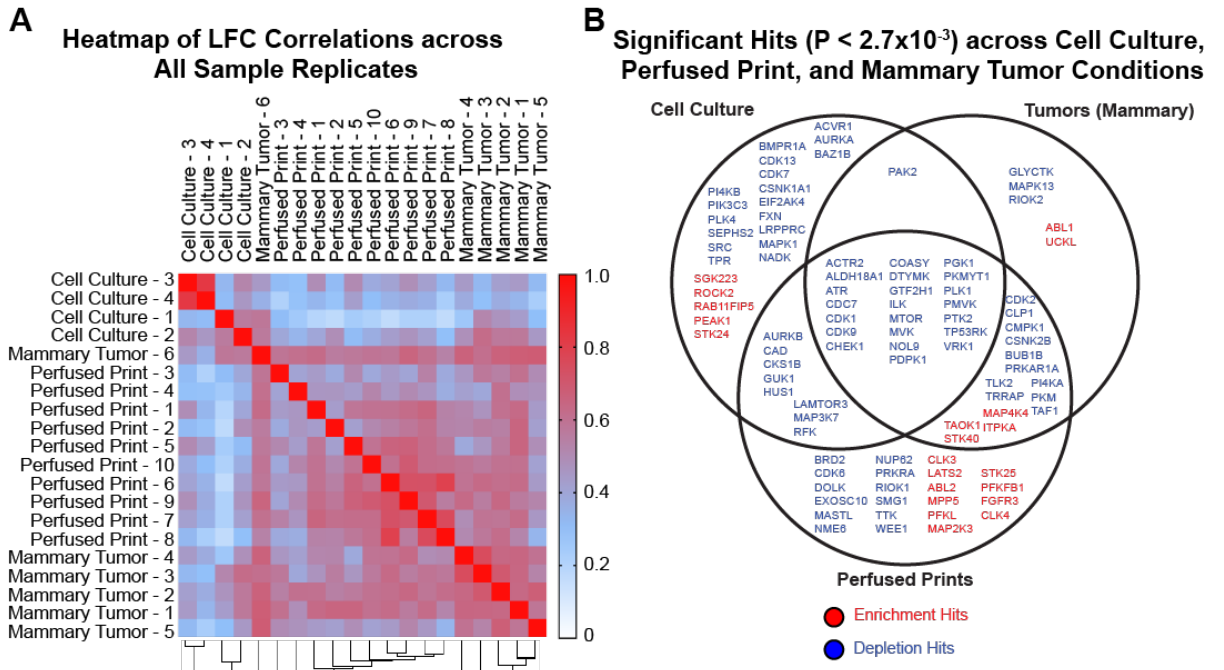

Figure 2.12: Comparison of Fitness Data from Kinome-wide CRISPRko screens in MDA-MB-231 cells across conditions (II). (A) Hierarchical clustering dendrogram and Heatmap showing coefficients of determination in paired comparisons between individual replicates in the kinome-wide screen. Coefficients were generated by comparing log_2fold change behavior of top hit genes (p-value < 0.0027) between each pair of replicates, while hierarchical clustering was performed on the same. **(D)** Venn diagram comparing top depletion and enrichment hits for cell culture, mammary tumor, and perfused print growth conditions, as determined by the MAGeCK algorithm. Criteria consisted of p-value < 0.0027, as well as a LFC value reflecting status as an enriched or depleted hit.

Biologically, shared hits between all conditions consisted largely of genes with essential roles in cell cycle regulation, transcription, and damage response[156,157]. As might be expected, many of these genes are known to be lethal when mutated, such as

CDK1, MVK, CDC7, and PTK2. With regards to the 2D cell culture condition in particular, the majority of significant hits appeared to be attributable to various cell-cycle regulators, such as CDK7 and ACVR1. In contrast, a greater proportion of hits shared between high-flow prints and tumors, as well hits shared between high-flow prints and cell culture, had roles in cellular metabolism[156,157], for instance, CMPK1, and PI4KA. Notably, perfused prints showed the greatest number of enrichment hits, a phenomenon that has been previously observed in another 3D culture model[46].

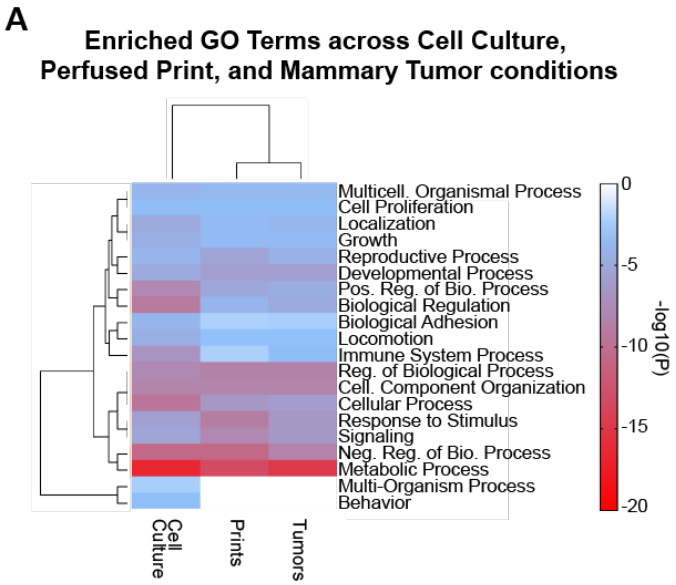

Figure 2.13: Comparison of Pathway Enrichment from Top Hits of Kinome-wide CRISPRko screens in MDA-MB-231 cells across conditions. (A) Metascape-generated heatmap and dendrogram of the 20 most highly-depleted Gene Ontology Biological Process Domain pathways based on the top 40 depletion hits for the cell culture, mammary tumor, and perfused print growth conditions.

In order to validate results, we selected six top depletion hits and six top enrichment hits unique to or selectively shared within the cell culture, perfused print, and mammary tumor conditions. Knockout constructs for each target were created by inserting a single sgRNA for each target, as well as a non-targeting control into the lentiCRISPRv2 backbone[145]. A competitive growth assay was then conducted in MDA-

MB-231 cells between each sgRNA and the non-targeting control in cell culture, perfused prints, and mammary tumors. Genomic DNA from all samples was subsequently extracted and sequenced. Relative depletion and enrichment levels for each guide under each condition were then calculated relative to the starting plasmid pool. The resulting data are shown in **Figure 2.14A - B**. In general, validation behavior matched the expected behavior based on screen result, confirming the overall efficacy of the studies.

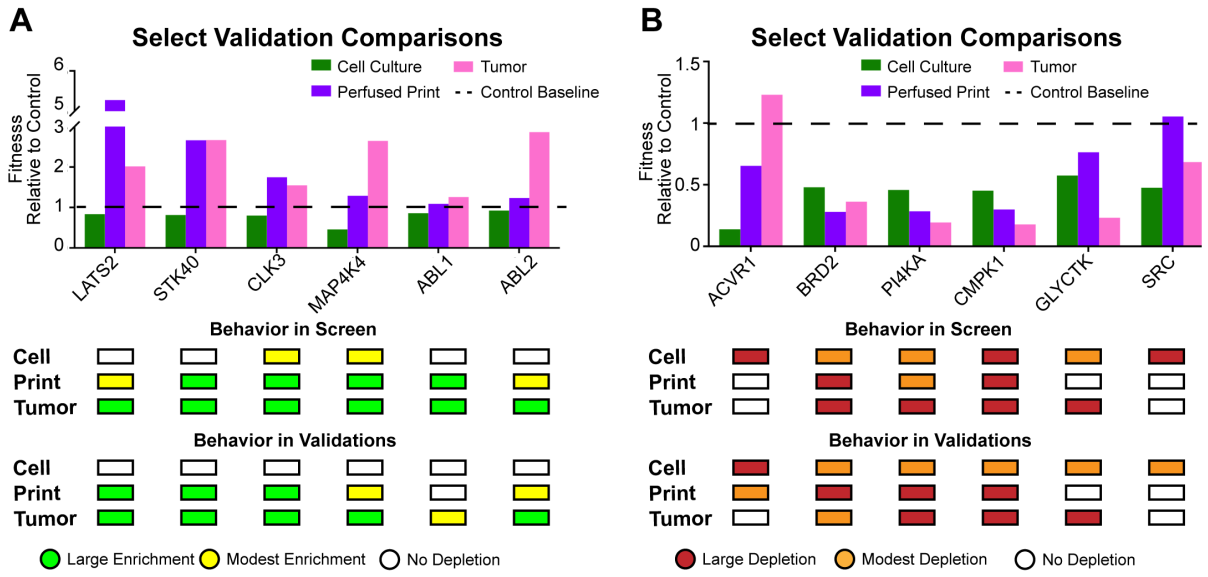

Figure 2.14: Individual validations of top depletion and enrichment hits of the kinome-wide CRISPRko screen. (A-B) Enrichment and Depletion comparisons (top) of six genes validated for cell culture, perfused print, and mammary tumor growth conditions in a competitive growth assay. All comparisons are made relative to distributions found in the original plasmid pool. Chart (bottom) showing expected enrichment or depletion behavior based on results of original screen, compared to observed enrichment or depletion behaviors in validation experiments.

2.5 Conclusion

Taken together, we have developed a platform and approach to conduct therapeutically relevant genetic screens in *ex vivo* tissue models. Specifically, our biologically-derived matrix systems enabled long-term tissue culture, and the comprehensive evaluation of transcriptomic and phenotypic responses confirmed that our tissue engineered models better mimicked *in vivo* conditions compared to traditional 2D and 3D cell culture techniques. While no model system is ideal or a complete recapitulation of the native biological setting, our methodology enables sustained perfusable co-cultures of multiple cell types, and with media and material optimization can enable progressively closer replication of the *in vivo* tumor microenvironment. We thus anticipate our screening format integrating tissue engineering with existing analytic technologies could allow for both better understanding of pathological behavior in various types of cancers, as well as improved discovery of drug targets.

2.6 Acknowledgements

Chapter 2 in full, contains material that appears in Integrated genome and tissue engineering enables screening of cancer vulnerabilities in physiologically relevant perfusable ex vivo cultures as it appears in Biomaterials Volume 280, 2022. I, as the dissertation author, was the primary author of this paper, with the full authors list being: Michael Hu, Xin Yi Lei, Jon Larson, Melissa McAlonis, Kyle Ford, Daniella McDonald, Krystal Mach, Jessica Rusert, Robert Wechsler-Reya, and Prashant Mali.

2.7 Appendix

2.7.1 Preparation of Perfused Printed Constructs for High-Flow

Described below is an example of a preparation method for a perfused printed construct capable of sustaining higher flow rates, formulated from a 1 mL matrix solution composed of 10 mg/mL fibrin, 4 mg/mL Matrigel, and 10 mg/mL gelatin. In addition, the example provides details for the encapsulation of spheroidal MDA-MB-231 clusters for culture.

Preparation of Matrigel, Gelatin, and Thrombin

1. Remove the Matrigel needed from -20°C at least 1 hour before starting the preparation and place on ice.
2. Remove stock 150 mg/mL gelatin solution from 4°C at least 1 hour before starting the preparation, and place at 37°C.
3. Remove stock 500 U/mL thrombin solution from -20°C and place on ice.

Spheroid Harvesting

Spheroids should be harvested at least 30 minutes before the intended time of encapsulation. This is necessary because media must be aspirated from the spheroids without centrifugation.

4. Cut the tip from a standard 1 mL pipette tip to widen the opening.
5. Gently collect spheroids one at a time from low-adhesion wells using the widened pipette tips.
6. Place each spheroid along with residual media in respective wells into a 15 mL centrifuge tube.
7. When finished, cap tube loosely and place in incubator at 37°C.
8. Allow spheroids to incubate for 30 minutes or more such that they can settle to the bottom of the centrifuge tube. During this time, other preparation steps may be completed.
9. Use pipette to gently remove media from the spheroids. Take care not to disturb the loose pellet of spheroids.

Preparation of 100 mg/mL Stock Fibrinogen Solution

10. Warm sterile dPBS (usually in TC fridge) to 37°C in water bath or incubator.
11. Obtain a sterile 1.5 mL vial, and weigh empty while closed.
12. Measure out 10 mg fibrinogen in a sterile operating environment
13. Rapidly add 100 uL warmed dPBS to fibrinogen and gently tap vial until every portion of the fibrinogen is wetted by the dPBS. Do NOT pipette the solution.
14. Incubate Fibrinogen at 37°C for 30 minutes, or until fully dissolved.

Preparation of 50 mg/mL Stock Transglutaminase Solution

15. Obtain a sterile 1.5 mL vial, and weigh empty while closed.
16. Measure out 5 mg transglutaminase in a sterile operating environment.
17. Add 100 uL warmed dPBS to transglutaminase and mix with pipette until dissolved into cloudy solution

18. Incubate at 37°C until fully dissolved.

Preparation of PVA Structures in Silicone Chips

19. Obtain sterile PVA vascular structures and place inlet and outlet ends into the metal perfusion channels in the silicone chip.
20. Gently insert solid metal rods of equal diameter to the inner diameter of the inlet and outlet metal perfusion channels until they come into contact with the PVA structures. The purpose of this is to prevent air pockets from forming.

Matrix Preparation

Matrigel should be kept on ice to prevent gelation. The order by which the components are added in this case is important. Gelatin and Matrigel have opposite temperature-responsive geling behavior, and must be kept separated.

21. Aliquot 400 uL Matrigel into 1.5 mL centrifuge tube.
22. Add 384 uL warmed media into 1.5 mL centrifuge tube.
23. Add 66 uL of warmed stock gelatin solution into warmed media.
24. Add 10 uL of 250 mM calcium chloride solution to warmed media.
25. Add 40 uL of stock transglutaminase solution to warmed media.
26. Add 100 uL of stock fibrinogen solution to warmed media.
27. Mix very well by pipetting at least 10 times.
28. Incubate for 20 minutes or more at 37°C to allow for transglutaminase to crosslink gelatin for optical clarity.
29. Harvest and spin down all cells of interest to be encapsulated within the matrix. Spheroids should be separate from these cells and should not be spun down.
30. Add 2 uL of thrombin stock solution to the Matrigel solution and mix well.
31. Rapidly add the warmed media and matrix solution prepared in Steps 16 – 21 to the Matrigel and thrombin solution. Mix by pipetting at least 5 times.
32. Re-suspend all non-spheroidal cells in complete matrix solution such that they will be resuspended at concentrations desired.
33. Re-suspend spheroids in complete matrix solution. Mixing should be extremely gentle to avoid damaging spheroids.
34. Pour Solution into silicone chips, over the PVA structures.
35. Let the chip sit for 5 minutes at room temperature, then place in 37°C for 20 – 30 minutes. At the end of this, the entire system should be gelated, and the PVA scaffold should have melted.

Evacuation of Sacrificial PVA Vasculature

36. Small portions of the PVA will remain isolated from the aqueous environment of the gelating matrix due to being inside the metal perfusion channels. Use the solid metal rods inserted in Step 14 to carefully and slowly push those portions of PVA forward, into the rest of the melted PVA.
37. Allow incubation for another 15 – 30 minutes.
38. During the incubation period, media for perfusion culture should be warmed to 37°C.
39. Fill 1 set of tubing with warm media. If necessary, sterilize with ethanol beforehand.

40. Remove samples from incubator.
41. Seal samples in an acrylic holder plate if not already sealed.
42. Remove solid metal rods from printed construct, taking care to make sure other parts of construct are not disturbed.
43. Link printed construct with perfusion pump tubing, and slowly perfuse with warm media to evacuate the melted PVA.
44. Perfuse for 5 minutes or more to ensure that all remaining PVA is removed.

Optional Endothelialization Step

1. Allow printed constructs to perfuse for at least several hours before initiating endothelialization.
2. Harvest and spin down Endothelial Cells.
3. Re-suspend cells such that they can be delivered to the matrix at concentrations desired. For endothelial cells, the desired concentration is ~5 - 10 x 10^6 cells/mL.
4. Use 200 mL pipette to VERY slowly inject endothelial cell solution into matrix.
5. Let sit 1 hr to allow Endothelial Adhesion.
6. Turn upside down for 1 hr to allow Endothelial Adhesion to other side.
7. Let sit 6 – 12 hrs (overnight preferred).
8. Begin perfusion.

2.7.2 Lentiviral Preparation of CRISPR Libraries

Described below is a series of steps that may be used to prepare lentivirus stocks of CRISPR knockout libraries for transduction into mammalian cells. Quantities used below are specific to a single 15 cm tissue culture dish of HEK 293T cells.

1. Prior to the day of the procedure, a 15 cm tissue culture dish of HEK 293T cells should be prepared such that it reaches approximately 60% confluency the day of the procedure.
2. Warm Opti-MEM (Life Technologies) to room temperature prior to procedure.
3. In 1 x 15 mL centrifuge tube, add 1.5 mL Opti-MEM with 36 mL of Lipofectamine 2000 (Life Technologies.
4. In a separate 15 mL centrifuge tube, add 1.5 mL Opti-MEM with 3 mg of pMD2.G (Addgene 12259), 12 mg of pCMV delta R8.2 (Addgene 12263), and 12 mg of the pooled vector library.
5. Allow 5 minutes of incubation at room temperature.
6. Very gently add the solution containing the DNA to the solution containing the Lipofectamine.
7. Allow 30 minutes of incubation at room temperature without disturbance.
8. Replace the media of the HEK 293T cells.
9. Gently add the Opti-MEM solution dropwise to the HEK 293T cells.
10. Wait 48 hours, then collect supernatant, and store at 4°C. Replace media.
11. Wait an additional 24 hours, then collect supernatant.
12. Filter supernatant through 0.45 um Steriflip filters (Millipore).
13. Transfer approximately 15 – 17 mL of filtered supernatant into an Amicon Ultra-15 centrifugal ultrafilter (Millipore) and centrifuge at 4°C at 3000 rcf or higher for 35 – 40 minutes.
14. Collect concentrated solution.
15. Repeat steps 13 and 14 until the supernatant has been completely concentrated.
16. Aliquot viral solution and store at -80°C until time of use.

2.7.3 Preparation of Validation Guide RNA Constructs

Described below is a series of steps that may be used to prepare individual plasmids targeting a specific gene for validation.

1. In a PCR tube, prepare a 50 uL solution containing 5 uL of NEB Buffer 3.1 (New England Biosciences), 3 uL of BSMB1 (New England Biosciences), and 3 ug of LentiCRISPRv2 plasmid.
2. Place the PCR tube in a thermocycler set to 55°C for 3 hours.
3. Perform PCR purification of the resulting product using the QIAquick PCR Purification Kit (Qiagen).
4. In a PCR tube, prepare a 10 uL solution containing 5 uL of Gibson Assembly Master Mix (New England Biosciences), 50 ng of digested LentiCRISPRv2 plasmid DNA, and 20 ng of the oligomer representing the validation sgRNA insert sequence.
5. Place the PCR tube in a thermocycler set to 50°C for 1 hour.
6. Thaw 50 uL of Stbl3 chemically competent E. coli (Thermofisher) on ice.
7. Add 5 – 10 uL of Gibson assembly mix to the vial containing the Stbl3 cells.
8. Mix gently by stirring with a pipette tip only.
9. Let incubate for 30 minutes on ice.
10. Perform a 45 second heat-shock on the vial containing the Stbl3 cells in a 42°C water bath.
11. Let incubate for 3 minutes on ice.
12. Add 250 uL of SOC media to the vial and mix briefy.
13. Place in a bacterial incubator and shake at 225 rpm for 1 hour.
14. Plate 100 uL of solution onto an agar plate supplemented with carbenicillin (50 mg/mL), and allow to grow for 16 – 18 hours.
15. Individual colonies can then be assessed for correct insert sequence.

2.7.4 Primer Sequences for Amplification of Integrated sgRNA from gDNA

Listed below are the specific primer sequences used to amplify guide RNA regions during PCR amplification and library preparation of the kinome-wide CRISPRko screen samples, as well as validation samples. Primer sequences were designed to contain one region complementary to the guide RNA scaffold that would allow direct amplification of the integrated gRNA region from genomic DNA, and an overhang region complementary to adapters and indices used for multiplexing on Illumina Sequencing Instrument Workflows.

Forward Primer
ACACTCTTTCCCTACACGACGCTCTTCCGATCTATCTTGTGGAAAGGACGAAACAC
CG

Reverse Primer
GACTGGAGTTCAGACGTGTGCTCTTCCGATCTGTACACGACATCACTTTCCCAGTT
T

Chapter 3: Incorporate Patient-Specific Tissue to Enable Point-of-Care Functional Oncology

3.1 Abstract

Despite promising mutational data obtained from whole-genome sequencing, application of personalized cancer medicine has been hampered by the lack of patient-specific models on which potential treatments can be functionally evaluated. In this chapter, we adapt and further optimize our biofabricated tissue model to allow it to generate three-dimensional perfusable dense cultures of otherwise unculturable patient-derived xenografts. We characterize the system in terms of growth, viability, and gene expression, and compare to existing 2D, 3D, and *in vivo* models. Using this system we then emulate a novel point-of-care diagnostics scenario of a clinically actionable CRISPR knockout (CRISPRko) screen of genes with FDA-approved drug treatments in *ex vivo* PDX cell cultures. Our results reveal differences across *in vitro* and *in vivo* cancer model systems, and highlight the utility of programmable tissue engineered models in screening for therapeutically relevant cancer vulnerabilities.

3.2 Introduction

A fundamental challenge in cancer therapeutics is the innate heterogeneity of tumors. It has been well-understood for decades that cancers contain mixed clonal subpopulations of cells[160], but recent advances in sequencing technologies have revealed significant variations in both genotypic and phenotypic characteristics of tumors on a patient-by-patient basis, even for patients with the same tumor sub-type[5–7]. The result is a wide variation in the effectiveness of established therapies across different

patients[6,7,160,160], highlighting the need for more personalized approaches to treatment[7,161–163].

To this end, several clinical trials have been conducted in which clinicians have made use of whole-genome sequencing to fully characterize patient tumors, identify key mutations, and select a personalized molecular targeting agent for the patient[10]. Unfortunately, results widely indicated that personalized treatments did not significantly impact patient outcomes. This is probably a consequence of several factors, with the most significant being a lack of translational effectiveness in gene-drug association. It is now known from clinical studies that genotype does not reliably predict drug response, likely because of the incomplete understanding of the phenotypic translation of specific mutations[16,17]. Notably, this does not mean personalized cancer medicine is a failure, but rather that functional testing, in which potential treatments are identified and evaluated in personalized model systems prior to patient treatment, is essential[17,163].

With regards to functional evaluation, CRISPR-screens have been developed as a high-throughput method by which large numbers of genetic vulnerabilities can be identified simultaneously, providing a phenotypic measure of the actual results of targeting a specific gene, rather than simple mutational identification[20–30]. In terms of model systems, for many decades, the technology that best mimics the human tumor microenvironment is the use of patient-derived xenograft (PDX) mouse models, in which biopsied tumor tissue is transplanted into and grown in a mouse[17,45,164–166]. In addition to issues such as murine selective pressures and limited engraftment rates[165] however, xenograft models are hampered by time-scale, with individual xenografts often requiring over 8 weeks to grow to a palpable degree[17,45], which is non-viable in a clinical setting.

While many 3D models such as organoid[52,117,124–126] and organ-chip technologies[63,118,127–131] exist, advances in 3D printing uniquely allow for the generation of tissue models that are able to better emulate their biological equivalents in material composition, scale, and cell density[71,82,121,133–136,139,140].

In the previous chapter, we described integrating our previously-designed engineered cancer models with CRISPRko screening technologies to assert that they could be used in this space. We now further refine our methodology towards a patient-specific cancer diagnostics scenario by incorporating PDX cells, and then applying a targeted CRISPRko screen. Characterization studies of the model indicated again that it more closely mimicked *in vivo* conditions compared to existing methods of cell culture, and results of a targeted CRISPR screen consisting of genes with FDA-approved drug treatments[167,168] suggest that the method has the potential for application in patient-specific therapeutics.

3.3 Methods

3.3.1 Printing Methodology

3.3.1.1 3D Printing of Silicone Holders and Long-Term Perfusion

Construction and long-term perfusion of flow chambers were accomplished as previously described[146]. Briefly, perfusion culture utilized a 3-component system consisting of a media reservoir, a flow chamber constructed via extrusion-printed silicone (Dow Corning Toray Sylgard SE1700), and a peristaltic pump (Watson Marlow 205U).

3.3.1.2 Preparation of Perfusable Tissue Constructs

Free-standing PVA structures were designed as previously described[146]. Briefly, geometries of interest were designed in AutoDesk Inventor, exported to the Ultimaker Cura software, and printed using the Ultimaker^3 from solid PVA filaments (Ultimaker).

A detailed description of generating the printed constructs can be found in Appendix 3.7.1. Briefly, for printed constructs used to culture human xenografts, matrix solutions were formulated from fibrinogen (7.5 mg/mL), hyaluronic acid (1 mg/mL), and thrombin (2 U/mL). Briefly, stock solutions of thrombin (Sigma-Aldrich) were prepared prior to formulation at 500 U/mL, aliquoted, and stored at -20 °C. Solutions of bovine plasma fibrinogen (Millipore) were dissolved in dPBS at 37 °C immediately prior to use, and at respective concentrations of 100 mg/mL. Hyaluronic acid (LifeCore) was prepared at a stock concentration of 10 mg/mL by stirring overnight in PBS at 4 °C. Matrices were prepared by directly mixing all components, resuspending cells in the matrix solution, pouring into single-chamber silicone holders, allowing for gelation, and then transferring into dual-chamber holders prior to perfusion, as previously described.

3.3.2 Cell Culture

The Med411-FH medulloblastoma patient-derived xenograft line[169,170] was maintained in the Wechsler-Reya lab. Tumors were harvested and dissociated into single cells the day of culture, and were subsequently encapsulated in their respective growth environments. For Med411-FH, media was composed of NeuroCult basal medium supplemented with Proliferation Kit (StemCell Technologies), 2 μg/mL heparin (Sigma), 20 ng/mL epidermal growth factor (Sigma), and 20 ng/mL fibroblast growth factor (Lonza).

3.3.3 Animal Work

Non-obese diabetic, severe combined immunodeficiency, interleukin-2 receptor gamma knockout (NOD-SCID gamma, or NSG) mice used for intracranial tumor transplantation were purchased from Jackson Labs (Stock No: 005557 Bar Harbor, ME) and maintained in animal facilities at the Sanford Consortium for Regenerative Medicine. All experiments were performed in accordance with national guidelines and regulations, and with the approval of animal care and use committees at Sanford Burnham Prebys Medical Discovery Institute and the University of California San Diego.

3.3.4 Model Growth

3.3.4.1 Ex Vivo Culture of Human Xenografts

The Med411-FH PDX line[169,170] was generated by Jim Olson's lab at Fred Hutchinson Cancer Research Center and maintained in the Wechsler-Reya Lab via orthotopic implantation of approximately 1 x 10^5 dissociated tumor cells into the cerebellum of male NSG mice. Lines were subsequently propagated from mouse-to-mouse[170–172]. Immediately prior to the study, tumors were allowed to grow for approximately 6 weeks before being harvested and dissociated into single cells via treatment with 10U/mL papain (Worthington). Cells were either snap-frozen in liquid nitrogen and stored at -80 °C, immediately resuspended into media, into one of several static matrix conditions, or into perfused print conditions, and allowed to grow over 10 days. Matrix composition in static matrix conditions consisted of a blend of either Matrigel (4 mg/mL), fibrinogen (7.5 mg/mL), gelatin (10 mg/mL), or fibrinogen (7.5 mg/mL) and

hyaluronic acid (1 mg/mL). Matrix composition in perfused prints consisted of fibrinogen (7.5 mg/mL) and hyaluronic acid (1 mg/mL). Subsequent media used was either the previously-described NeuroCult formulation, or a 1:1 mixture of the NeuroCult formulation with EGM-2 (Lonza).

3.3.5 Model Analysis

3.3.5.1 Cell Density Calculations

For Med411-FH PDX cells, matrices could not be easily removed from their holders. Consequently, approximate cell density comparisons were calculated using the initial matrix masses loaded for each matrix and print condition. Cells were isolated from their matrix environments using either Dispase II solution or Papain as described previously. Living cells were counted using the Trypan Blue assay, and density was approximated using the number of living cells, and the original mass of matrix solution used for each condition.

3.3.5.2 Imaging

Widefield fluorescent microscopy images were obtained using the Leica DMi8 microscope at 10X magnification with a resolution of 0.1118 mm. Confocal images were obtained using the Zeiss 880 Airyscan Confocal.

3.3.5.3 Validation of Screen Hits with Drug Treatments

Top hits from the screen, mTOR, Topoisomerase, and CDK4/6 were respectively targeted using Everolimus (SelleckChem), Irinotecan (SelleckChem), and Palbociclib

(SelleckChem). For storage, stock solutions of Everolimus and Irinotecan were prepared by dissolving at 10 mM in DMSO, while a stock solution of Palbociclib was prepared by dissolving at 10 mM in water. All stock solutions were stored at -80 °C. In all cases, perfused prints with PDX medulloblastoma cells were prepared as previously described, and allowed to grow for 72 hours. Perfusion media was then supplemented with drugs for 48 hours. Everolimus and Palbociclib were respectively supplemented at 10 μM, while Irinotecan was supplemented at 5 μM. After 48 hours, the drug supplementation was removed, and perfusion with non-drug treated media was continued for 24 hours, after which quantitative viability measurements were obtained using the CCK8 assay.

3.3.6 Genetic and Transcriptomic Analysis

3.3.6.1 Extraction of RNA from PDX Medulloblastoma Cells for Transcriptomic Analysis

Snap-frozen cells had RNA extracted directly using the RNeasy Kit (Qiagen). For matrix and perfused print conditions containing only fibrin or a combination of fibrin and hyaluronic acid, matrices were cut into <1 mm pieces, resuspended in 10U/mL papain (Worthington), and allowed to incubate for 1 hour at 37 °C to digest the matrix. To collect cells following all matrix digestions, solutions were centrifuged at 300g for 5 minutes, and supernatant was aspirated. RNA was then extracted using the RNeasy Kit.

Following RNA extraction, approximately 500 ng of RNA from each condition was used to synthesize cDNA using the NEBNext poly(A) mRNA Magnetic Isolation Module (New England Biosystems). Libraries were then constructed and indexed using the NEBNext Ultra II RNA Library Prep Kit (New England Biosystems) and NEB Multiplex

Primers. The final product was purified using 1.0x Ampure XP beads, pooled in equal ratios, and sequenced using the NovaSeq with either paired end 250 bp reads or paired end 100 bp reads.

3.3.6.2 Targeted CRISPR Knockout Screen in PDX Models

The puromycin-resistance domain of the LentiCRISPR v2 plasmid[145] was excised and replaced with an eGIP reporter sequence[173]. A plasmid map and the full plasmid sequence can be found in Appendix 3.7.3. A total of 66 unique gene-targeting sgRNAs, 4 non-targeting control sgRNAs, and 4 AAVS1-targeting sgRNAs (Appendix 3.7.4) were inserted individually by Gibson assembly into the plasmid via a BsmBI cut site. For each sgRNA, the Gibson assembly was transformed into chemically competent Stbl3 cells (Invitrogen), and sgRNA identity was confirmed via sanger sequencing of individually purified clones. Plasmid DNA here was extracted using a QIAprep Spin Miniprep Kit (Qiagen). The sequence validated plasmids were then pooled and transformed into Stbl4 electrocompetent Escherichia coli (Invitrogen), which were recovered for 1 hour at 37 °C in SOC media (Thermo). Subsequently, the transformed Escherichia coli were used to inoculate a100 mL culture of LB-carbenicillin (50 mg/mL) and incubated overnight at 37 °C. Plasmid DNA was then extracted with a QIAprep Spin Maxiprep Kit (Qiagen).

To produce lentivirus particles, 36 mL of Lipofectamine 2000 (Life Technologies) was added to 1.5 mL of Opti-MEM (Life Technologies), while 3 mg of pMD2.G (Addgene 12259), 12 mg of pCMV delta R8.2 (Addgene 12263), and either 12 mg of the pooled vector library or 9 mg of a single guide construct were added to a separate 1.5 mL of Opti-MEM. Both solutions were incubated for 5 minutes at room temperature, after which they

were mixed and allowed to incubate for an additional 30 minutes. This final transfection solution was added dropwise to a 15 cm tissue culture dish of HEK 293T cells at approximately 60% confluency prior. Notably, a single solution of this composition was used to transfect a single 15 cm dish. Supernatant was collected after 48 and 72 hours, filtered through 0.45 mm Steriflip filters (Millipore), and concentrated using Amicon Ultra-15 centrifugal ultrafilters (Millipore). Final viral solutions were aliquoted and stored long-term at -80 °C. A detailed description of the methodology can be found in Appendix 3.7.2.

For viral transduction, PDX medulloblastoma cells were supplemented with medium containing polybrene (8 mg/mL, Millipore) and enough viral particles to produce a 0.3 MOI. After 24 hours, medium was replaced. After 72 hours, cells were harvested and distributed into either perfused print conditions, or orthotopic tumor conditions. Replicates for each condition contained a minimum of 1 x 10^5 transduced cells to achieve >1000-fold library coverage. Cells selected for perfused print conditions were encapsulated within a matrix of 5 mg/mL fibrin and 1 mg/mL hyaluronan, and allowed to grow for 6 weeks. Because digestion of the matrices occurred, cells were intermittently freed from the matrices via papain-digestion, and re-encapsulated.

3.3.6.3 Extraction and Processing of gDNA for Screen Analysis

Genomic DNA was directly extracted from cell culture samples via the DNeasy Blood and Tissue Kit (Qiagen). For perfused print and tumor samples, cells were first isolated from their matrix environments. Matrices or tissue were cut into < 1 mm fragments, then resuspended in Dispase II solution (Millipore) and incubated at 37 °C on a shaker at 60 rpm for 1.5 hours. The solution was then centrifuged for 5 minutes at 300g,

supernatant was aspirated, and the remaining cells and matrix fragments were resuspended in the digestion solution provided by the Miltenyi Tumor Dissociation Kit (Miltenyi Biotec) and incubated at 37 °C on a shaker at 60 rpm for 1.5 hours. The solution was then centrifuged for 5 minutes at 300g, and supernatant was aspirated. DNA was then extracted from the remaining cells via the DNeasy Blood and Tissue Kit (Qiagen).

Guide RNA sequences were amplified using Kapa Hifi HotStart polymerase (Roche). An approximately 350 bp fragment was amplified in the PCR 1 reaction using primers containing the Illumina adaptor sequences (Appendix 3.7.5), with input quantities achieving 1000-fold coverage. Of note, conditions without enough cells or DNA to account for a minimum 500-fold coverage were not processed further. Amplicons were purified using the PCR Purification Kit (Qiagen), and 50 ng of product was transferred to the PCR 2 reaction. Amplicons from the knockout library samples were indexed using either NEBNext Single Index Oligos for Illumina (New England Biosystems) or NEBNext Multiplex Oligos for Illumina kit (New England Biosystems). The final product was purified using 1.2x volume of Ampure XP beads, mixed in equal ratios, and sequenced on the NovaSeq with paired end 100 bp reads respectively.

3.3.7 Computational Analysis

3.3.7.1 Computational Analysis of Targeted Knockout Library

Raw FASTQ files were analyzed using the MAGeCK software to both quantify guides and test for enrichment or depletion. All samples were median-normalized, and replicates were compared to Day 3 samples to calculate both positive and negative guide enrichment. Log_2-fold change (LFC) measurements were calculated for each guide for all

individual replicates, and for overall treatment conditions obtained by grouping all replicates for a given condition. Zscores were calculated directly from Log_2-fold change measurements.

3.3.8 Statistical Analysis

Statistical parameters (mean, standard deviation) for all data shown in bar graphs were processed using GraphPad Prism v7.0. Direct statistical comparisons where indicated were conducted using a two-sided t-test. Samples used in the data are biological replicates. Hierarchical clustering for RNA-seq data was performed in R using the DESeq2, stats, genefilter, and pheatmap packages. Clustering was performed using the Pearson Correlation as the measure of distance, and the Average Distance as the method. Principal component analysis for both RNA-seq and CRISPR screening data was performed in R using the Stats package. For CRISPR screening data, all log_2fold measurements were normalized as Z-scores prior to analysis. Correlational comparisons, linear regressions, and calculations of coefficients of determination (R^2) for all CRISPR screening datasets was performed in MATLAB.

3.4 Results and Discussion

3.4.1 Perfused PDX medulloblastoma tumor models show greater similarities to in vivo tumors compared to 2D cell culture and static 3D culture

Spurred by the encouraging results from the previous chapter, we next evaluated the ability of the system to culture primary patient-derived cancer tissues. Specifically, we explored patient-derived xenograft cells, which are known to often be difficult to culture *in*

vitro without genetic reprogramming[174], but offer the closest available model of a primary human tumor. Towards this, mCherry-labeled medulloblastoma PDX cells were orthotopically injected into the cerebellum of immunodeficient (NOD-SCID-IL2R gamma knockout, or NSG) mice, allowed to grow over 6 weeks, harvested and dissociated into single cells. We determined optimal growth conditions by encapsulating the dissociated cells in one of four static matrix conditions or in perfused prints, and then culturing them over 10 days. Static matrix conditions contained either blends of fibrin and hyaluronic acid (HA), materials relevant for brain tumor models[119], or a blend of the biologically derived matrices: fibrin, gelatin, and Matrigel[146]. Prints were constructed from blends of fibrin and HA. Each condition was grown in either supplemented NeuroCult medium (NC) (StemCell Technologies), or a 1:1 mixture of NC and Endothelial Growth Medium 2 (EGM-2) (Lonza), with EGM-2 being present to permit potential co-culture with endothelial cells. Growth in various 3D matrix conditions was assessed both qualitatively via microscopic images, and quantitatively (**Figure 3.1A**) using the Cell-Counting Kit 8 reagent (Dojindo). Results suggested that the presence of HA significantly increased cell growth. Additionally, the degree of growth in blends of fibrin/HA and fibrin/gelatin/Matrigel showed no significant difference. Upon comparing static matrix conditions and perfused print conditions, both qualitative images (**Figure 3.1B**) and cell density measurements (**Figure 3.1C**) indicated significantly more growth in perfused prints, regardless of matrix composition.

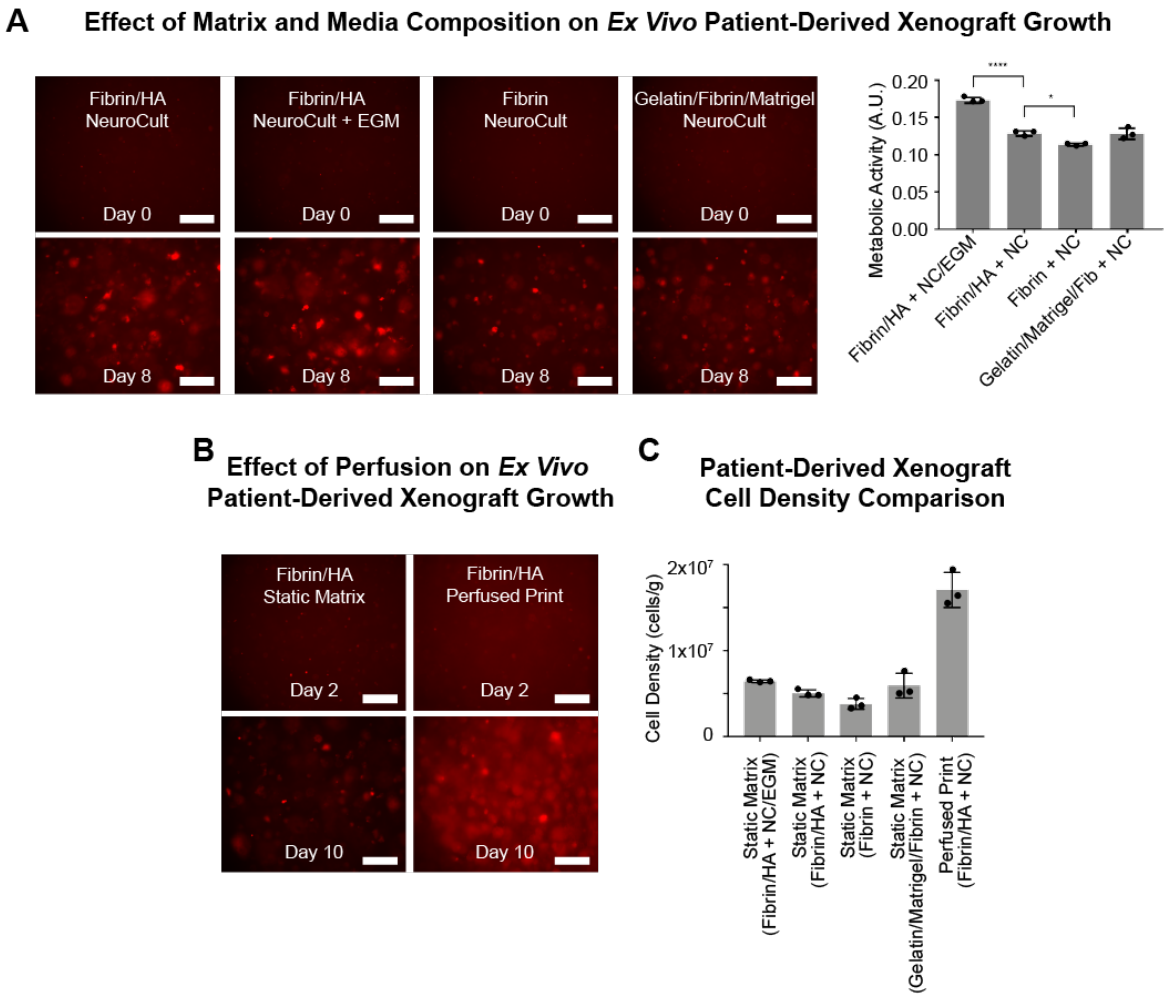

Figure 3.1: Optimization and evaluation of culture conditions for patient-derived xenografts. (A) Fluorescent images (left) and metabolic activity measurements (right) of PDX medulloblastoma cells grown in matrices of various compositions. Scale bars: 250 μm (n = 3 with P values *P < 0.05 and ****P <0.0001). Error bars show standard deviation. **(B)** Fluorescent images showing the growth of PDX medulloblastoma cells in static matrix conditions compared to perfused print conditions. Scale bars: 250 μm. **(C)** Cell density counts for PDX medulloblastoma cells in various static matrix conditions compared to perfused prints (n = 3).

To further characterize the system, we performed a gene expression analysis comparing PDX medulloblastoma cells grown *in vivo* to those grown in several *in vitro* conditions. Specifically, PDX medulloblastoma cells grown orthotopically in mice were compared to those grown in static matrix and perfused print conditions, and to those

grown in suspension culture, as is standard for many established medulloblastoma cell lines[175–177] (**Figure 3.2A**). Of note, hMSC and HUVECs were not included in these cultures, as hMSCs are not a prominent population in the brain, and culturing conditions were not optimal for endothelial cells. For the orthotopic condition, mRNA was extracted directly from cells dissociated from PDX tumors. For all *in vitro* conditions, cells were grown over a period of 10 days, after which mRNA was extracted. Transcriptomic profiles were generated through bulk-RNA sequencing, followed by STAR alignment[149] and analysis with the DESeq2 pipeline[155].

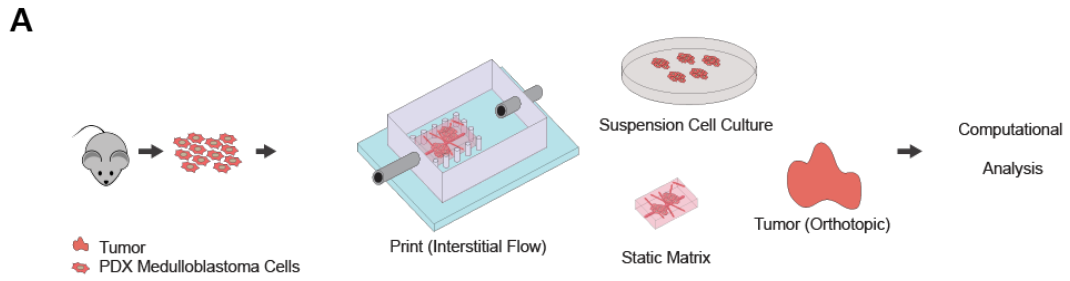

Figure 3.2: Ex vivo culture of PDX medulloblastoma cells in various model conditions. (A) Schematic representation of PDX medulloblastoma culture conditions. PDX medulloblastoma cells are isolated from tumors, then distributed across several conditions: suspension cell culture, static matrices, perfused printed constructs, and tumors in mice injected orthotopically in the cerebellum. Conditions are sustained over 10 days, after which RNA is extracted, amplified, and sequenced.

Initially, we compared relative expression levels of common medulloblastoma marker genes, or those associated specifically with one of the four medulloblastoma subtypes[178,179] across all conditions. Log-normalized expression of common marker genes in medulloblastomas (NES, MYC, and CD276) as well as marker genes associated with Group 3 medulloblastomas appeared consistent across nearly all conditions (**Table 3.1**), suggesting that the Group 3 medulloblastoma characteristics appear to be maintained under *in vitro* growth conditions.

Table 3.1: Relative expression levels of key medulloblastoma subtype marker genes across all conditions.

Gene Class	Gene	Cells 1	Cells 2	Matrix Fibrin/HA (NC + EGM) 1	Matrix Fibrin/HA (NC + EGM) 2	Matrix Fibrin/HA (NC) 1	Matrix Fibrin/HA (NC) 2	Print Fibrin/HA (NC) 1	Print Fibrin/HA (NC) 2	Tumor 1	Tumor 2
Common Marker Genes	GAPDH	13.2	13.1	12.3	12.8	12.8	13.2	13.1	13.1	13.1	13.2
	NES	7.7	8.0	8.2	8.4	8.4	8.6	8.5	8.5	8.5	8.5
	MYC	14.4	14.2	13.3	13.7	13.6	14.1	14.5	14.6	14.4	14.5
	CD276	8.9	9.0	9.0	9.1	9.1	9.4	8.4	8.4	8.4	8.5
Wnt-Type Medulloblastoma Marker	DKK1	-0.2	-0.1	-0.4	-0.4	-0.4	-0.4	-0.4	-0.4	-0.4	-0.4
	WIF1	0.0	0.0	0.0	0.0	0.0	0.0	0.0	0.0	0.0	0.0
	DKK2	-2.2	-2.2	-2.2	-2.2	-2.2	-2.2	-2.2	-2.2	-2.2	-2.1
	DKK4	-0.6	-0.6	-0.5	-0.6	-0.6	-0.5	-0.6	-0.4	-0.6	-0.5
	LEF1	-0.8	-0.8	-0.5	-0.7	-0.8	-0.6	-0.9	-0.9	-0.9	-0.8
	WNT11	2.6	2.8	3.3	3.7	3.7	3.7	2.4	2.6	2.8	2.7
	WNT16	4.2	4.5	3.6	3.7	3.9	4.1	3.9	3.8	4.0	4.4
SHH-Type Medulloblastoma Marker	SFRP1	8.3	8.6	5.5	4.4	5.9	6.2	6.2	6.1	5.1	5.1
	HHIP	5.0	5.1	4.8	5.3	5.4	5.4	5.0	5.5	4.1	3.9
	GLI1	3.5	3.7	4.7	4.1	3.9	4.1	3.9	3.8	4.2	4.1
	GLI2	1.8	2.4	1.9	1.9	2.2	2.6	2.6	2.5	2.4	1.9
	BOC	3.2	2.4	3.7	3.9	3.1	4.0	3.7	4.0	5.1	5.2
	ATOH1	-2.3	-2.3	-2.3	-2.3	-2.3	-2.3	-2.3	-2.3	-2.3	-2.3
	SOX2	-1.1	-1.2	-0.9	-1.2	-0.9	-1.1	-1.2	-1.2	-1.2	-1.1
	SOX9	6.7	6.7	6.5	6.8	7.0	7.4	7.1	7.3	6.1	6.2
	SOX13	2.6	3.5	2.7	2.9	3.1	3.3	2.8	2.9	2.3	2.5
	HOXA5	-1.5	-1.4	-1.4	-1.4	-1.4	-1.5	-1.5	-1.5	-1.5	-1.4
	HOXA9	-0.3	-0.3	-0.4	-0.4	-0.3	-0.5	-0.5	-0.5	-0.5	-0.4
Group 3 Medulloblastoma Marker	NPR3	10.6	10.6	8.2	8.1	8.1	8.5	9.9	9.9	8.6	8.6
	IMPG2	11.7	11.7	10.4	10.6	10.8	11.0	11.8	11.8	11.7	11.7
	GABRA5	11.2	11.0	10.4	10.3	10.5	10.7	11.4	11.4	11.5	11.6
	NRL	6.4	6.4	8.0	8.4	7.4	7.4	6.4	6.2	6.6	6.8
	MAB21L2	11.6	11.5	10.9	11.0	10.8	10.8	10.9	11.0	11.0	11.1
	CRX	7.5	7.8	8.7	8.2	7.9	8.0	7.4	7.6	7.5	7.5
Group 4 Medulloblastoma Marker	EOMES	-0.5	-0.7	-0.7	-0.7	-0.6	-0.7	-0.7	-0.6	-0.7	-0.7
	UNC5D	3.0	2.7	2.3	2.2	2.2	2.3	3.0	3.0	3.5	3.7
	RBM24	3.9	3.5	3.1	3.4	3.3	4.0	4.1	3.9	3.7	3.3
	OAS1	-2.3	-2.3	-2.3	-2.3	-2.3	-2.3	-2.3	-2.3	-2.3	-2.3
	KCNA1	-1.9	-1.9	-1.8	-1.9	-1.9	-1.9	-1.9	-1.9	-1.9	-1.9
	KCNA5	2.1	2.5	2.2	2.2	2.1	2.5	2.6	2.5	2.1	2.2

(Data entries are rlog (normalized log2) representations of relative gene expression)

Hierarchical clustering performed based on the transcriptomic profiles revealed that, like with the MDA-MB-231 cells analyzed previously, perfused prints clustered more closely with tumors compared to both the static matrix and cell culture conditions (**Figure 3.3A**). A principal component analysis performed across expression profiles of all genes showed tumors separating from perfused print and cell culture conditions, but with the perfused print condition remaining closer overall (**Figure 3.3B**).

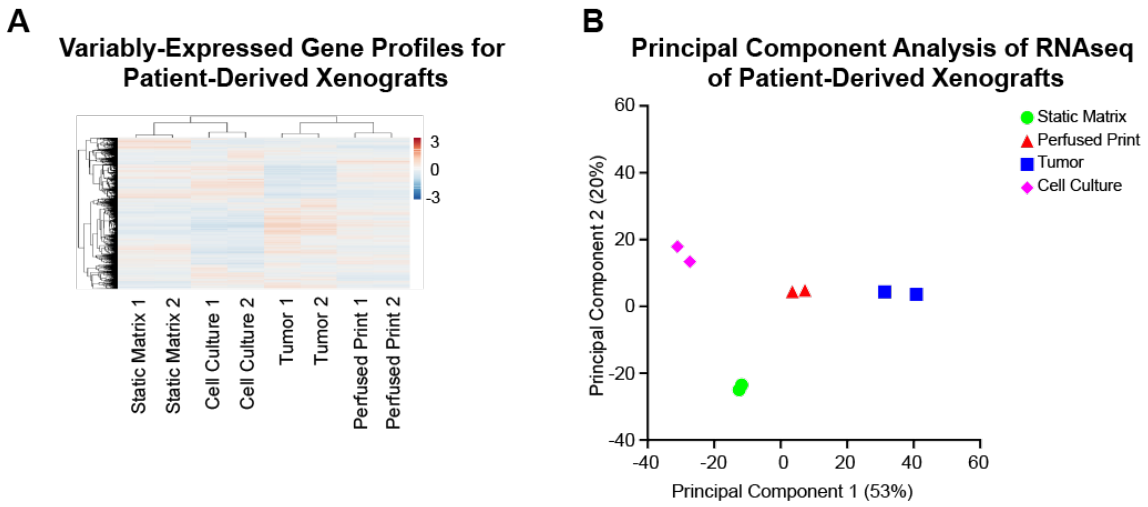

Figure 3.3: Transcriptomic profiling of PDX medulloblastoma cells cultured ex vivo in various model conditions. (A) Hierarchical clustering diagram comparing relative transcriptomic profiles of all expressed genes in PDX medulloblastoma cells grown in suspension cell culture, static matrix, perfused print, and orthotopic tumor conditions (n = 2 for each condition). **(B)** Principal component analysis comparing relative transcriptomic profiles of all expressed genes in PDX medulloblastoma cells grown in suspension cell culture, static matrix, perfused print, and orthotopic tumor conditions (n = 2 for each condition).

Furthermore, like before, the number of differentially expressed genes between perfused prints and tumors was lower than either cell culture or static matrix conditions compared to tumors (**Figure 3.4A**).

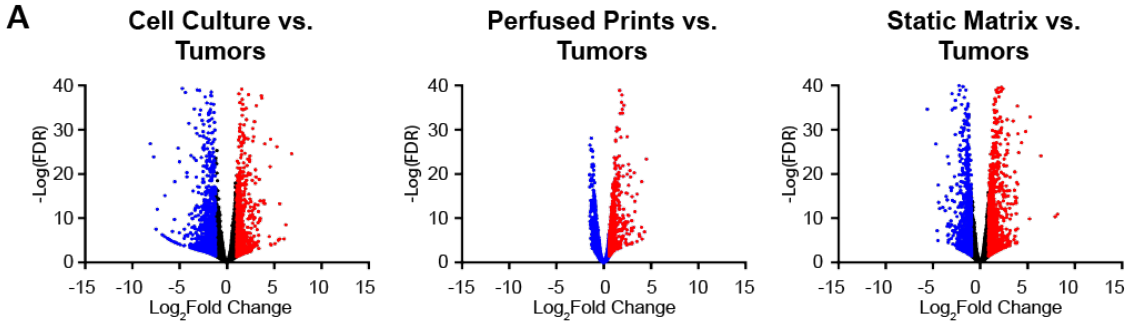

Figure 3.4: Comparison of differentially expressed genes of PDX Medulloblastoma cells cultured ex vivo in various conditions. (A) Comparison of differentially expressed genes PDX Medulloblastoma cells when grown in cell culture, perfused print, and static matrix conditions, relative to orthotopic tumor conditions.

Of note, data associated with PDX medulloblastoma cells grown with a mixture of NeuroCult and EGM-2 media was analyzed as well, but both a principal component analysis and hierarchical clustering based on all expressed genes revealed that the transcriptomic profiles deviated extremely heavily from all other conditions (**Figure 3.5A - B**). This is likely the result of the serum present within the EGM-2 media, as NeuroCult is normally a serum-free formulation. Because of these differences, the data associated with these samples was not analyzed any further, and it is also for this reason that co-culture with endothelial cells was not further pursued.

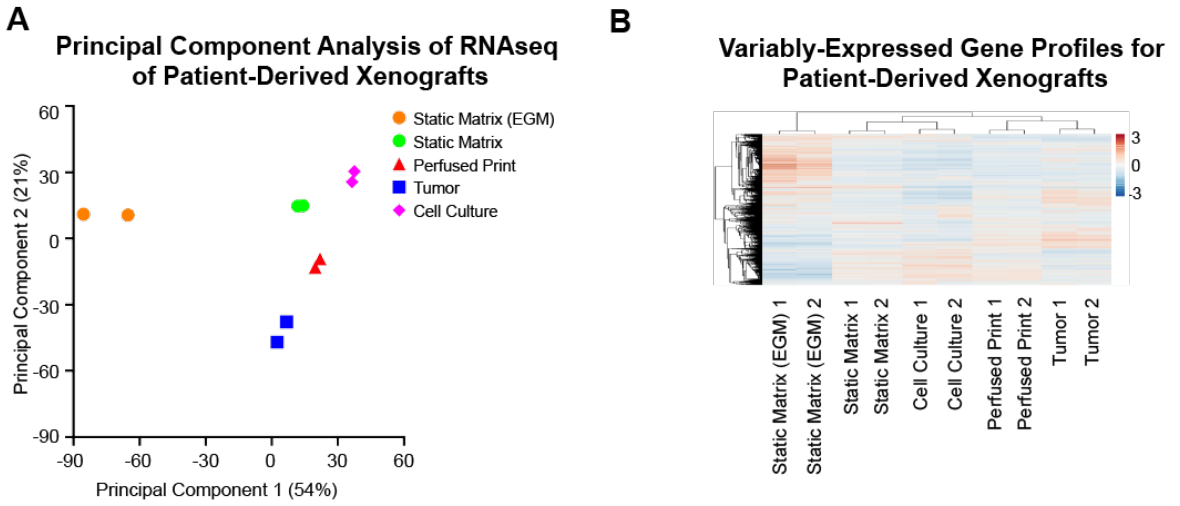

Figure 3.5: Transcriptomic Deviations of PDX medulloblastoma cells cultured with a mixed NeuroCult and EGM-2 formulation. (A) Principal component analysis comparing relative transcriptomic profiles of all expressed genes in PDX medulloblastoma cells grown in suspension cell culture, static matrix, perfused print, and orthotopic tumor conditions, along with static matrix with a mixed media formulation of NeuroCult and EGM-2 (n = 2 for each condition). **(B)** Hierarchical clustering diagram comparing relative transcriptomic profiles of all expressed genes in PDX medulloblastoma cells grown in suspension cell culture, static matrix, perfused print, and orthotopic tumor conditions, along with static matrix with a mixed media formulation of NeuroCult and EGM-2 (n = 2 for each condition).

Because our previous analyses indicated that the perfused print conditions appeared more similar to the orthotopic tumors, we performed a closer examination of the gene-level similarities between the two conditions. Both the perfused print condition and orthotopic tumor condition were compared to the cell culture condition (**Figure 3.6A**) and the static matrix condition (**Figure 3.6B**) as baselines, and differentially expressed genes were identified through DESeq2. Genes were categorized as either highly enriched or highly depleted if they possessed both a |Zscore| > 1.5, and an FDR < 0.1. Metascape was used to perform pathway-enrichment analysis within the Gene Ontology Biological Processes domain, and both tumors and perfused prints were found to share 40% of their top 20 enriched pathways and over 50% of their top 20 depleted pathways compared to

cell culture, and 25% of their top 20 enriched pathways and over 50% of their top 20 depleted pathways compared to static matrices[156,157].

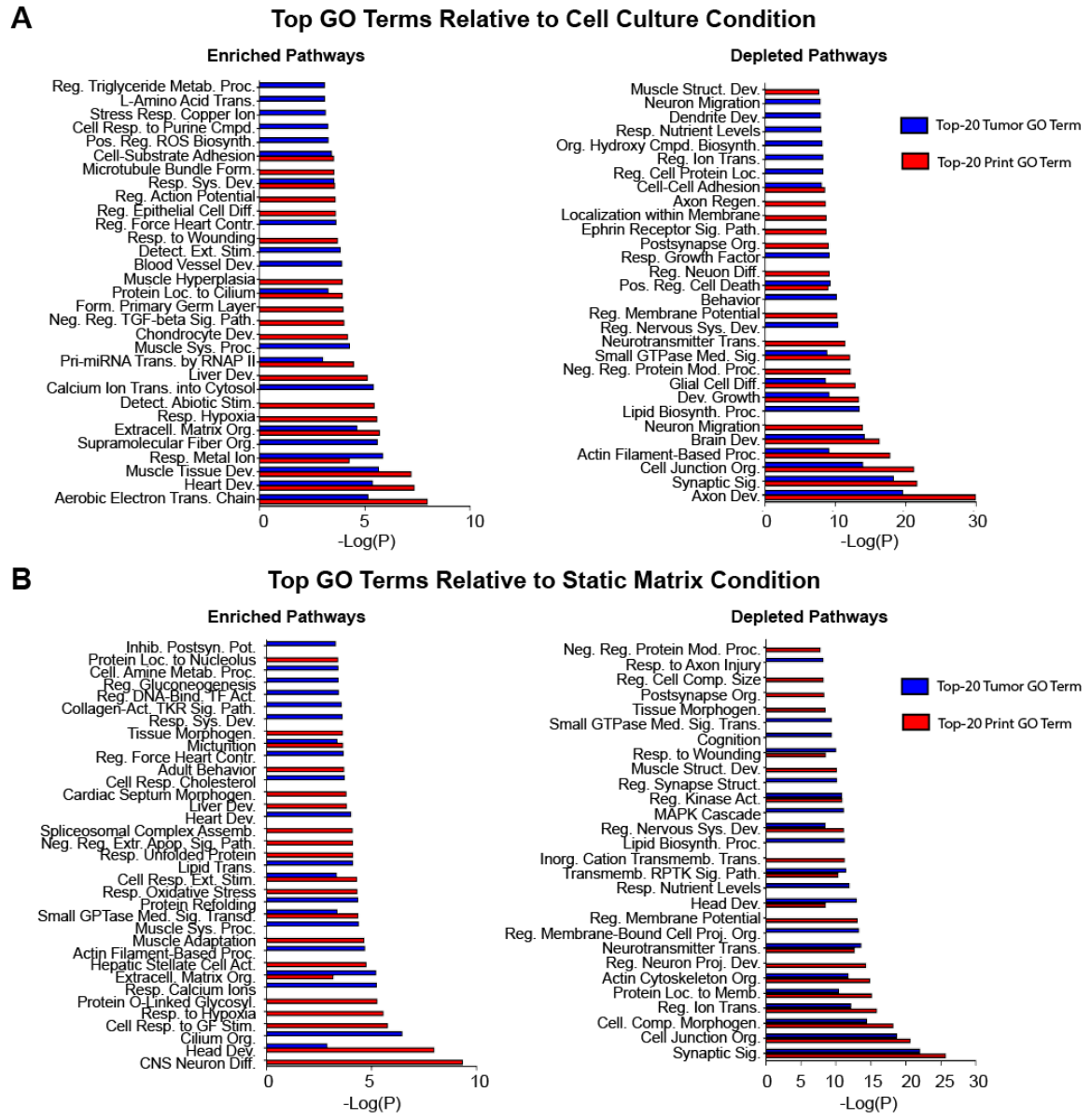

Figure 3.6: Enriched Pathway Comparison in PDX Medulloblastoma Tumor Models. (A) Top-20 Metascape-generated enriched (left) and depleted (right) Gene Ontology Biological Process Pathways that are shared by perfused print and tumor conditions in comparison to the suspension cell culture condition. **(B)** Top-20 Metascape-generated enriched (left) and depleted (right) Gene Ontology Biological Process Pathways that are shared by perfused print and tumor conditions in comparison to the static matrix condition.

Similar to the analysis in MDA-MB-231 cells described previously, tumor and perfused print conditions showed significant enrichment in extracellular matrix organizational processes, compared to both suspension cell culture and static matrix conditions. In addition, there was also enrichment in genes associated with the electron transport chain relative to cell culture, suggesting potential metabolic differences, and both tumor and perfused print conditions showed depletion in genes associated with positive regulation of apoptosis. This included genes such as BAD, GADD45A, and CTNNA1[180–182], all known to be involved in positively promoting apoptotic pathways. Consistent with this, upon comparing viability of the PDX medulloblastoma cells in suspension cell culture relative to perfused prints (**Figure 3.7A**), we noted viability was high immediately following dissociation from tumors, but progressively decreased over time in suspension cell culture, but in contrast, *ex vivo* viability remained both high and stable when cultured in perfused prints.

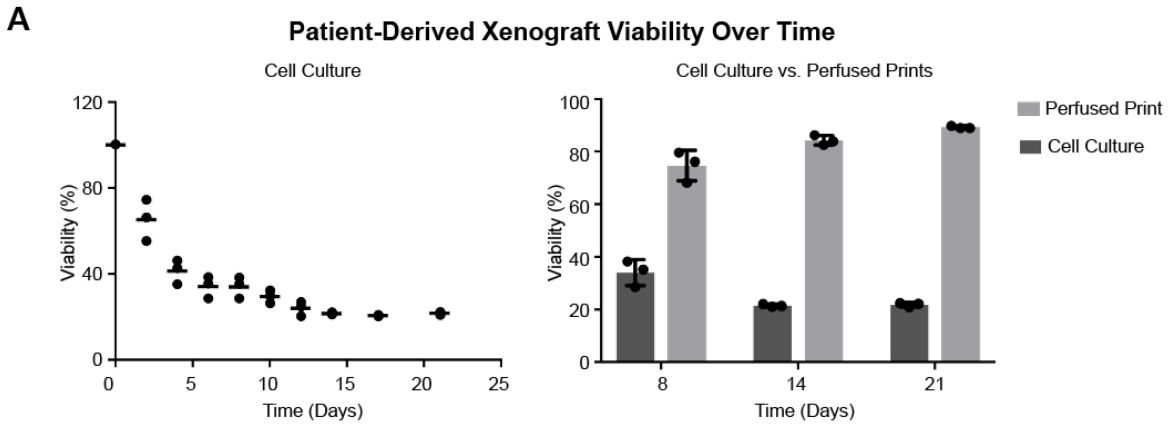

Figure 3.7: Viability comparison of PDX medulloblastoma cells cultured ex vivo in suspension and perfused cultures. (A) Survival of PDX medulloblastoma cells over time when grown in suspension cell culture (left), and comparison of PDX medulloblastoma cell survival in suspension cell culture vs. perfused prints (right).

3.4.2 A curated CRISPRko screen of genes with FDA-approved drug treatments reveals targetable vulnerabilities in PDX medulloblastoma models

In an ideal bed-side diagnostic scenario, a perturbation screen could be used to fully characterize a patient's tumor to develop a patient-specific treatment plan. However, tumor biopsies are typically obtained via syringe, with even large cores being no more than 1/16" in diameter and 1/2" in length. A genome-wide perturbation screen requires hundreds of millions of cells for necessary coverage when accounting for transduction efficiencies[37,40,145], and as such, would be impractical in this setting. In contrast, a smaller-scale but targeted screen containing sgRNAs for genes of high therapeutic interest would be much more applicable and of greatest utility to clinicians.

To this end, we construct a 74-element CRISPRko library from gene-targets of known FDA-approved anti-cancer drugs[167], as well as genes known to have prominent roles in Group 3 medulloblastomas[179] (**Figure 3.8A**). This library was to be integrated with the aforementioned PDX models. In addition to replicating aspects of the *in vivo* microenvironment, the perfused culture system was capable of growing the PDX cells *ex vivo* with greater survivability compared to suspension cell culture, and at higher growth rates compared to static 3D culture, both key requirements in conducting a successful depletion screen.

We initiated the CRISPRko screen by transducing the library into PDX medulloblastoma cells. A portion of the transduced cells was harvested and frozen at Day 3, while the rest were split by being either encapsulated into perfused printed constructs, or injected into the cerebellum of immunodeficient (NOD-SCID-IL2R gamma knockout, or NSG) mice. A full workflow is shown in **Figure 3.8B**. This experiment was conducted

twice to ensure reproducibility of results, with the first and second trials respectively including n = 4 and n = 5 replicates for perfused prints, and n = 6 replicates for tumors. Each replicate was loaded with over 1 x 10^5 transduced cells each to achieve over 1000-fold coverage at initial onset, and cells in all conditions were allowed to grow for 6 weeks. Genomic DNA from all samples was subsequently extracted, sequenced, and analyzed using the MAGeCK pipeline[159]. Fitness for individual genes was estimated by calculating the Zscores of the $\log_2$foldchange.

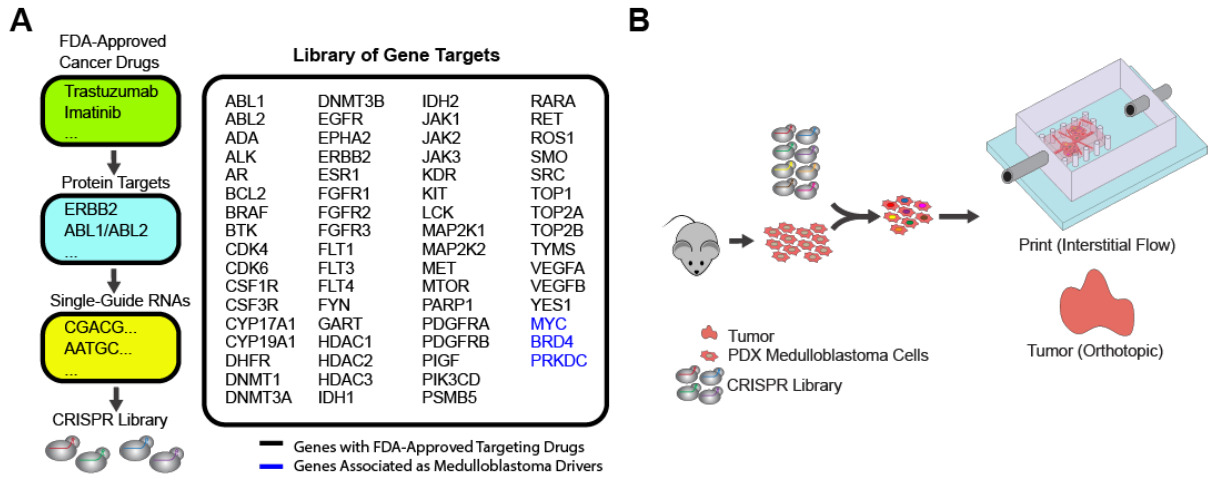

Figure 3.8: Targeted CRISPRko screen in PDX medulloblastoma cells cultured in the ex vivo perfused 3D model, and in in vivo orthotopic locations in mice. (A) Overview of CRISPR knockout library design. Target genes of single-guide RNAs were assembled from a list of genes with FDA-approved drugs targeting their products. **(B)** Schematic representation of the targeted CRISPR knockout screen. PDX-medulloblastoma cells are isolated from tumors, and lentivirally transduced with a 74-element CRISPR knockout library. Cells are collected and distributed in perfused printed constructs and tumors in mice injected orthotopically in the cerebellum. Conditions are sustained over 6 weeks, after which gDNA is extracted, amplified, sequenced, and processed.

A fitness comparison between perfused prints of the first and second trials showed relatively high correlation and consistent behavior (**Figure 3.9A**) while a similar comparison between tumors of the first and second trials showed substantially more variability (**Figure 3.9B**).

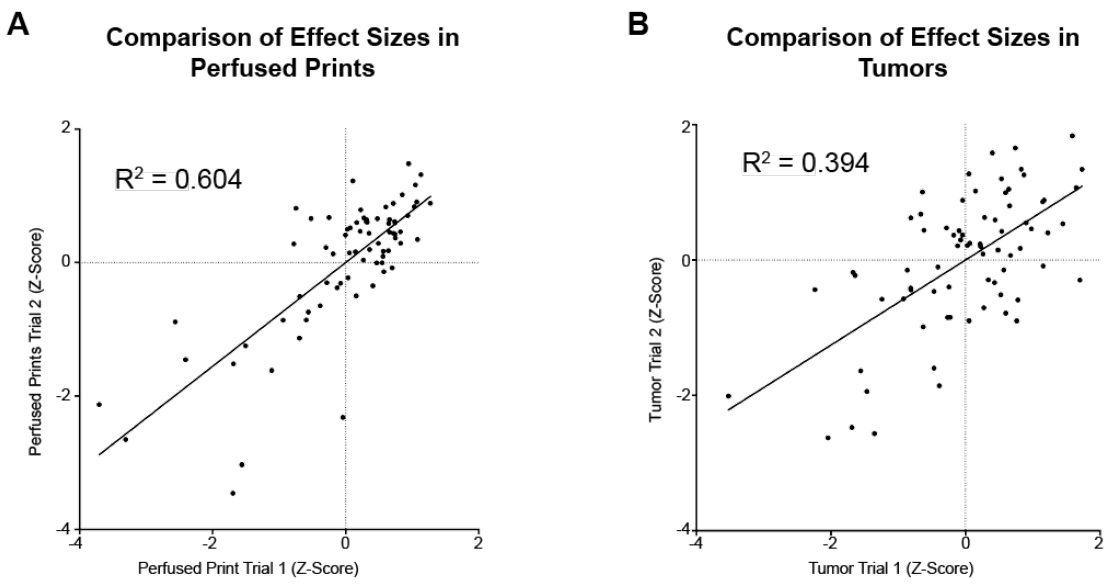

Figure 3.9: Comparison of Targeted CRISPRko Screen Result Reproducibility in Perfused Prints and Tumors. (A) Comparison of effect sizes (Z-Score) for all 74 sgRNA targets between two rounds of the CRISPRko screen conducted in perfused prints. **(B)** Comparison of effect sizes (Z-Score) for all 74 sgRNA targets between two rounds of the CRISPRko screen conducted in orthotopic tumors.

This was further reflected when a principal component analysis was performed across all genes of all replicates, and indicated close clustering of all print replicates, and substantially greater variation for all tumor replicates **(Figure 3.10A**). A fitness comparison between tumor and perfused print conditions revealed a number of shared genes depleted in both conditions (**Figure 3.10B**). These included KDR, MYC, mTOR, TOP, CDK4, and CDK6. MYC, while lacking a therapeutic targeting agent, is known to be a primary driver of Group 3 Medulloblastomas[179], and as such, its behavior is as expected. Potential use of KDR, mTOR, and CDK4/6 inhibitors in the context of medulloblastomas have been investigated with positive results[169,183–185], while topoisomerases have also been found to be highly expressed in medulloblastomas[186].

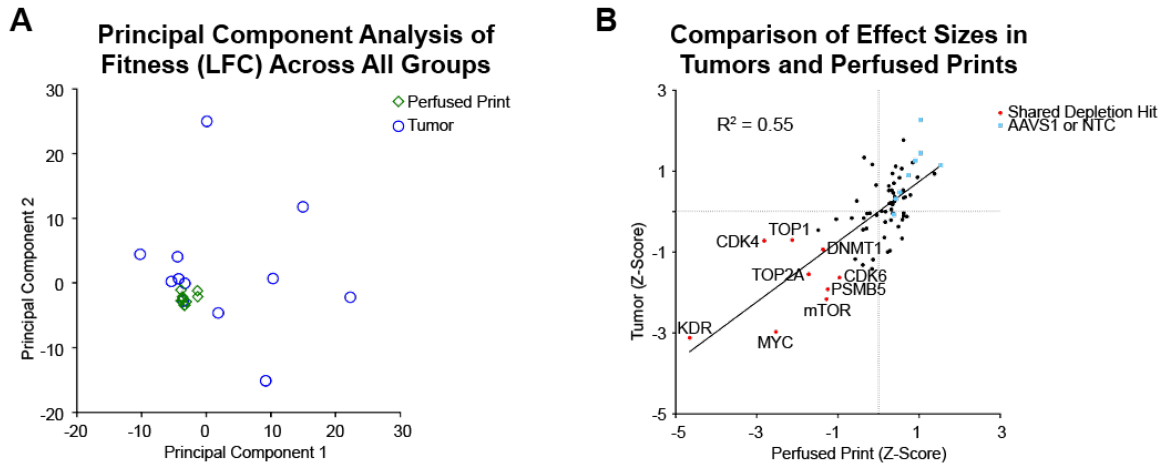

Figure 3.10: Comparison of Targeted CRISPRko Screen Results in Perfused Prints and Tumors. (**A)** Results of a principal component analysis performed across all genes of all individual replicates for each treatment condition. **(B)** Comparison of effect sizes (Z-Score) for all 74 sgRNA targets in perfused prints and orthotopic tumors. AAVS1 and NTC respectively represent sgRNAs targeting the adeno-associated virus integration site 1 and non-targeting controls, both serving as controls.

To validate results, inhibitory drugs against TOP, mTOR, and CDK4/6 were obtained and a growth comparison was made in perfused print PDX medulloblastoma models grown with and without each respective drug. Inhibition of growth was assessed qualitatively via fluorescent microscopy images over time (**Figure 3.11A**). Similarly, a quantitative comparison of cell viability using the CCK8 assay revealed significantly inhibited growth in each case (**Figure 3.11B**).

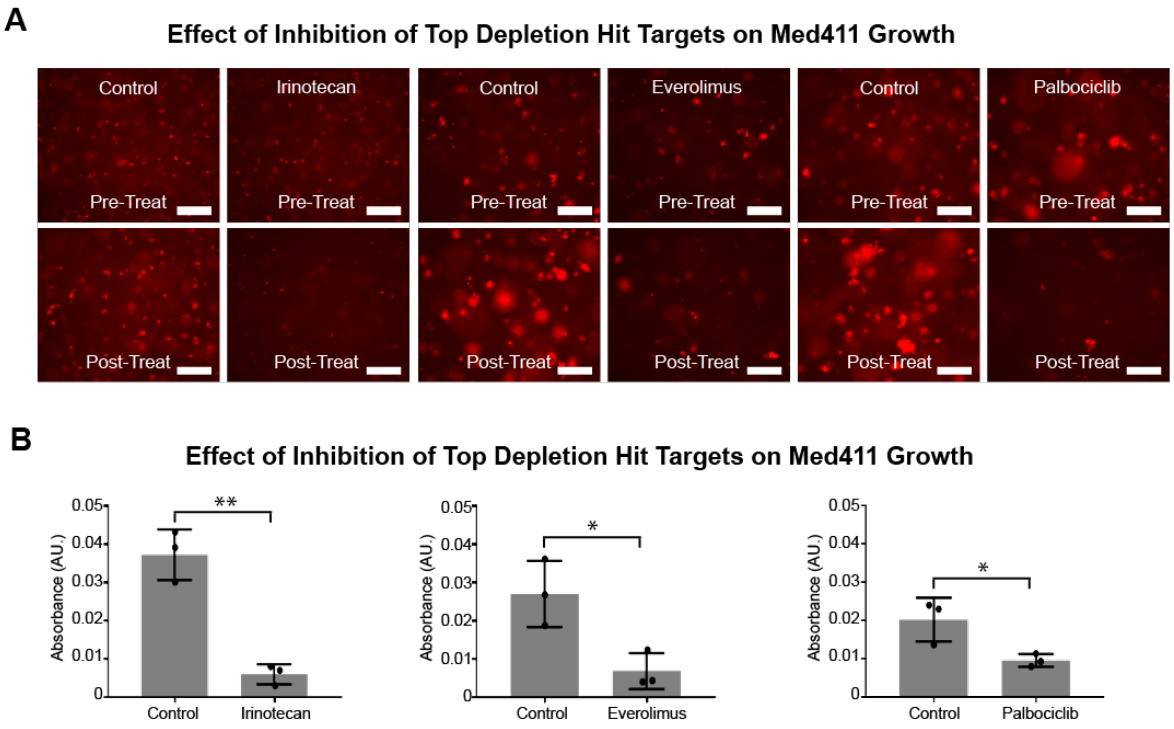

Figure 3.11: Drug Validations of Top Targets from Targeted CRISPRko Screen in PDX Medulloblastoma models. (A) Fluorescent images showing the growth of PDX medulloblastoma cells in with and without inhibitory drug treatments targeting top hits from the results of the CRISPRko Screen. Scale bars: 250 μm. **(B)** Metabolic activity measurements of PDX medulloblastoma cells grown in perfused prints when treated with various drugs inhibiting top depletion targets of the CRISPRko screen (n = 3 with P values *P < 0.05 and **P < 0.01).

Together, the results and validation confirm the overall efficacy of the studies and potential utility of this methodology in point-of-care oncology settings. As such, in a hypothetical diagnostic scenario, a targeted CRISPRko library could be transduced into a small number of cells obtained from a tumor biopsy. The transduced cells could subsequently be cultured, and the distribution of sgRNAs sequenced to obtain potential patient-specific treatment targets in a matter of weeks (**Figure 3.12A**).

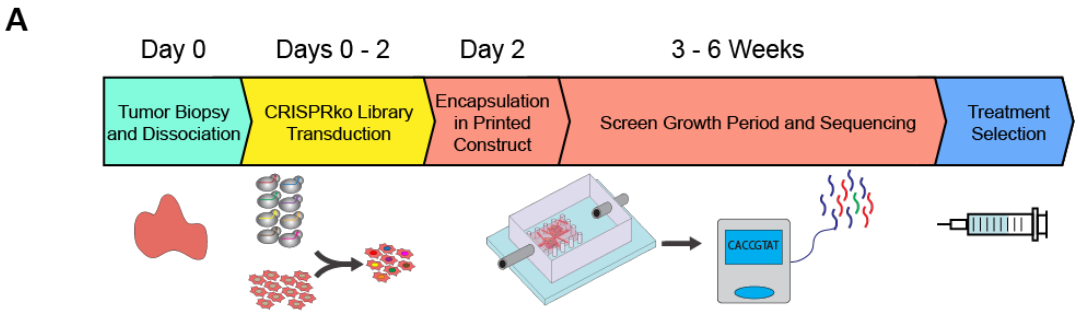

Figure 3.12: Applicational Timeline for Therapeutic Use. (A) Timeline for a potential point-of-care functional oncology setting outlining the use of focused CRISPR screens in a perfused printed model for patient-specific cancer vulnerability screening.

3.5 Conclusion

Here, we have further expanded upon our platform and provided a proof-of-concept of its potential translational use. In addition to long-term culture of established cell lines, we have enabled *ex vivo* maintenance of PDXs, which are typically refractory to *in vitro* culture. Again, transcriptomic and phenotypic responses confirmed that our tissue engineered models better mimicked *in vivo* conditions compared to traditional 2D and 3D cell culture techniques. When applied in a point-of-care oncology scenario, results of our CRISPRko screen for therapeutically-actionable targets in a medulloblastoma PDX model revealed and validated several notable hits, including mTOR, CDK4/6, and TOP all of which have been evaluated as potential targets in medulloblastomas. Moreover, results in our engineered system showed comparable results to identical screens conducted in current gold-standard PDX models, while also demonstrating greater reproducibility. Taken together, we have integrated major advances in the distinct fields of genetic and tissue engineering, and produced a novel means by which to identify potential therapeutic treatments on a patient-specific basis.

3.6 Acknowledgements

Chapter 3 in full, contains material that appears in Integrated genome and tissue engineering enables screening of cancer vulnerabilities in physiologically relevant perfusable ex vivo cultures as it appears in Biomaterials Volume 280, 2022. I, as the dissertation author, was the primary author of this paper, with the full authors list being: Michael Hu, Xin Yi Lei, Jon Larson, Melissa McAlonis, Kyle Ford, Daniella McDonald, Krystal Mach, Jessica Rusert, Robert Wechsler-Reya, and Prashant Mali.

3.7 Appendix

3.7.1 Preparation of Perfused Printed Constructs from Fibrin and HA Matrices

Described below is an example of a preparation method for a perfused printed construct capable of sustaining higher flow rates, formulated from a 1 mL matrix solution composed of 10 mg/mL fibrin, and 1 mg/mL hyaluronic acid.

Preparation of Hyaluronic Acid
Hyaluronic acid solution should be prepared at least 24 hours prior to intended print preparation in order to give adequate time to dissolve.

1. Aliquot approximately 50 mg of lyophilized hyaluronic acid ((LifeCore) into a 15 mL centrifuge tube.
2. Add 5 mL of cold PBS. Do not attempt to mix by pipetting.
3. Place on shaker at 4°C for a minimum of 12 hours.

Preparation of Thrombin

4. Remove stock 500 U/mL thrombin solution from -20°C and place on ice.

Preparation of 100 mg/mL Stock Fibrinogen Solution

5. Warm sterile dPBS (usually in TC fridge) to 37°C in water bath or incubator.
6. Obtain a sterile 1.5 mL vial, and weigh empty while closed.
7. Measure out 10 mg fibrinogen in a sterile operating environment
8. Rapidly add 100 uL warmed dPBS to fibrinogen and gently tap vial until every portion of the fibrinogen is wetted by the dPBS. Do NOT pipette the solution.
9. Incubate Fibrinogen at 37°C for 30 minutes, or until fully dissolved.

Preparation of PVA Structures in Silicone Chips

10. Obtain sterile PVA vascular structures and place inlet and outlet ends into the metal perfusion channels in the silicone chip.
11. Gently insert solid metal rods of equal diameter to the inner diameter of the inlet and outlet metal perfusion channels until they come into contact with the PVA structures. The purpose of this is to prevent air pockets from forming.

Matrix Preparation

12. Harvest, spin down, or prepare all cells to be encapsulated prior to preparing matrix solutions.
13. Add 800 uL warmed media into 1.5 mL centrifuge tube.
14. Add 100 uL of stock fibrinogen solution to a separate 1.5 mL centrifuge tube.
15. Add 100 uL of stock hyaluronic acid solution to fibrin solution.
16. Add 2 uL of thrombin stock solution to the warmed media solution and mix well.
17. Rapidly add the warmed media to the solution of fibrinogen and hyaluronic acid, and mix well.
18. Re-suspend all cells in complete matrix solution such that they will be resuspended at concentrations desired.
19. Pour Solution into silicone chips, over the PVA structures.

20. Let the chip sit for 5 minutes at room temperature, then place in 37°C for 30 – 40 minutes. At the end of this, the entire system should be gelated, and the PVA scaffold should have melted.

Evacuation of Sacrificial PVA Vasculature

21. Small portions of the PVA will remain isolated from the aqueous environment of the gelating matrix due to being inside the metal perfusion channels. Use the solid metal rods inserted in Step 11 to carefully and slowly push those portions of PVA forward, into the rest of the melted PVA.
22. Allow incubation for another 30 – 40 minutes.
23. During the incubation period, media for perfusion culture should be warmed to 37°C.
24. Fill 1 set of tubing with warm media. If necessary, sterilize with ethanol beforehand.
25. Remove samples from incubator.
26. Seal samples in an acrylic holder plate if not already sealed.
27. Remove solid metal rods from printed construct, taking care to make sure other parts of construct are not disturbed.
28. Link printed construct with perfusion pump tubing, and slowly perfuse with warm media to evacuate the melted PVA.
29. Perfuse for 5 minutes or more to ensure that all remaining PVA is removed.

3.7.2 Lentiviral Preparation of CRISPR Libraries

Described below is a series of steps that may be used to prepare lentivirus stocks of CRISPR knockout libraries for transduction into mammalian cells. Quantities used below are specific to a single 15 cm tissue culture dish of HEK 293T cells.

1. Prior to the day of the procedure, a 15 cm tissue culture dish of HEK 293T cells should be prepared such that it reaches approximately 60% confluency the day of the procedure.
2. Warm Opti-MEM (Life Technologies) to room temperature prior to procedure.
3. In 1 x 15 mL centrifuge tube, add 1.5 mL Opti-MEM with 36 mL of Lipofectamine 2000 (Life Technologies.
4. In a separate 15 mL centrifuge tube, add 1.5 mL Opti-MEM with 3 mg of pMD2.G (Addgene 12259), 12 mg of pCMV delta R8.2 (Addgene 12263), and 12 mg of the pooled vector library.
5. Allow 5 minutes of incubation at room temperature.
6. Very gently add the solution containing the DNA to the solution containing the Lipofectamine.
7. Allow 30 minutes of incubation at room temperature without disturbance.
8. Replace the media of the HEK 293T cells.
9. Gently add the Opti-MEM solution dropwise to the HEK 293T cells.
10. Wait 48 hours, then collect supernatant, and store at 4°C. Replace media.
11. Wait an additional 24 hours, then collect supernatant.
12. Filter supernatant through 0.45 um Steriflip filters (Millipore).
13. Transfer approximately 15 – 17 mL of filtered supernatant into an Amicon Ultra-15 centrifugal ultrafilter (Millipore) and centrifuge at 4°C at 3000 rcf or higher for 35 – 40 minutes.
14. Collect concentrated solution.
15. Repeat steps 13 and 14 until the supernatant has been completely concentrated.
16. Aliquot viral solution and store at -80°C until time of use.

3.7.3 Modified LentiCRISPRv2 Plasmid

Due to the sensitivity of the Med411 PDX medulloblastoma cells, a standard puromycin-selection process typical to the LentiCRISPRv2 plasmid could not be used. Instead, the puromycin-resistance domain of the LentiCRISPRv2 plasmid was removed and replaced with an eGFP reporter sequence to allow for assessment of transduction efficiency via imaging or flow cytometry.

A plasmid map of the modified plasmid is shown below in Figure 3.7.1, along with the full sequence of the plasmid.

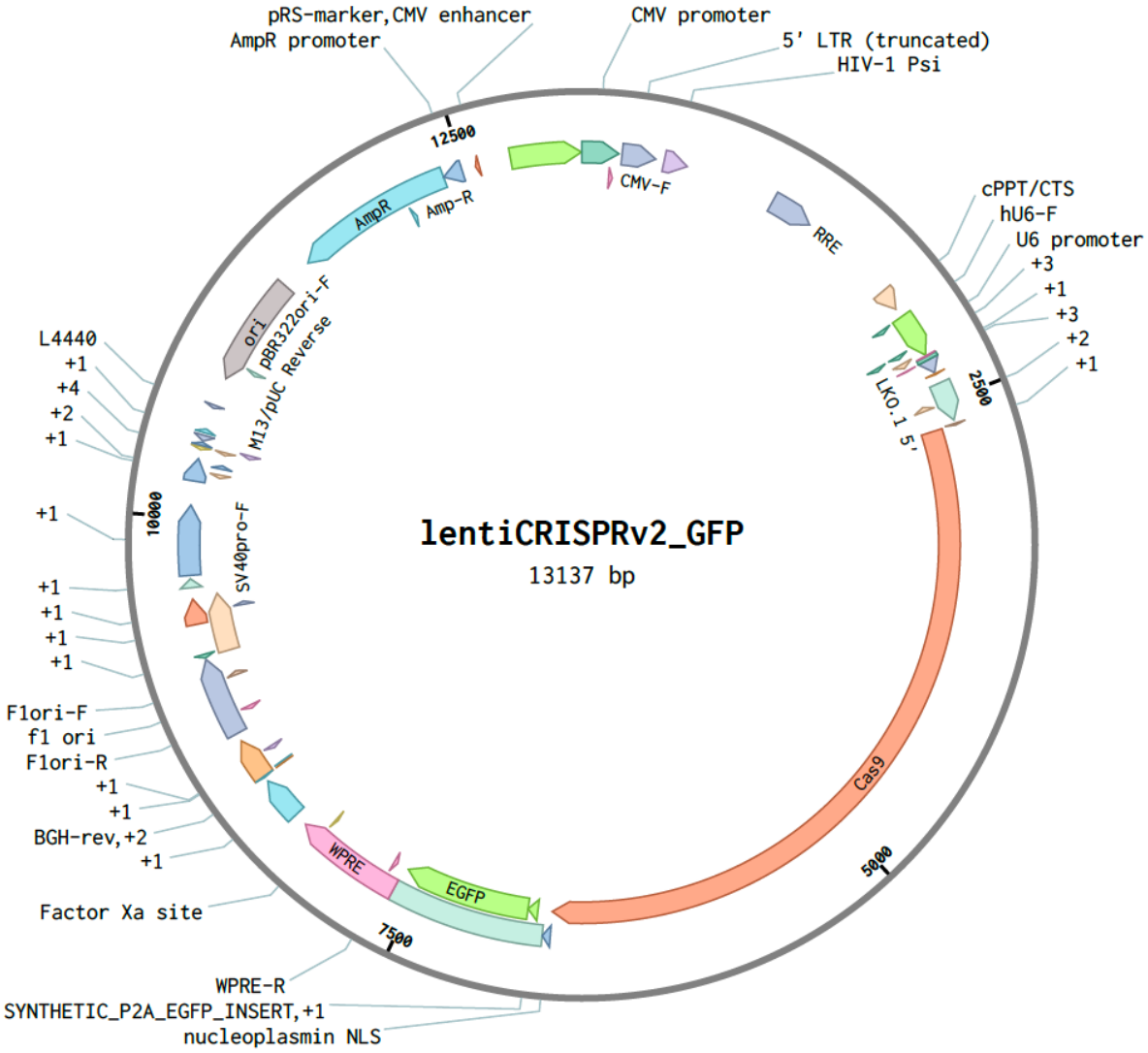

Figure 3.13: Plasmid map of the modified LentiCRISPRv2 plasmid used for construction of the targeted library.

Plasmid Sequence

tgatgcggttttggcagtacatcaatgggcgtggatagcggtttgactcacggggatttccaagtctccaccccattgacgtc
aatgggagtttgttttggcaccaaaatcaacgggactttccaaaatgtcgtaacaactccgccccattgacgcaaatgggc
ggtaggcgtgtacggtgggaggtctatataagcagcgcgttttgcctgtactgggtctctctggttagaccagatctgagcct
gggagctctctggctaactagggaacccactgcttaagcctcaataaagcttgccttgagtgcttcaagtagtgtgtgcccgt
ctgttgtgtgactctggtaactagagatccctcagacccttttagtcagtgtggaaaatctctagcagtggcgcccgaacagg
gacttgaaagcgaaagggaaaccagaggagctctctcgacgcaggactcggcttgctgaagcgcgcacggcaagag
gcgaggggcggcgactggtgagtacgccaaaaattttgactagcggaggctagaaggagagagatgggtgcgagag
cgtcagtattaagcgggggagaattagatcgcgatgggaaaaaattcggttaaggccaggggaaagaaaaaatata
aattaaaacatatagtatgggcaagcagggagctagaacgattcgcagttaatcctggcctgttagaaacatcagaaggc
tgtagacaaatactgggacagctacaaccatcccttcagacaggatcagaagaacttagatcattatataatacagtagc
aaccctctattgtgtgcatcaaaggatagagataaaagacaccaaggaagctttagacaagatagaggaagagcaaa
acaaaagtaagaccaccgcacagcaagcggccgctgatcttcagacctggaggaggagatatgagggacaattgga
gaagtgaattatataaatataaagtagtaaaaattgaaccattaggagtagcacccaccaaggcaaagagaagagtggt
gcagagagaaaaaagagcagtgggaataggagctttgttccttgggttcttgggagcagcaggaagcactatgggcgc
agcgtcaatgacgctgacggtacaggccagacaattattgtctggtatagtgcagcagcagaacaatttgctgagggctat
tgaggcgcaacagcatctgttgcaactcacagtctggggcatcaagcagctccaggcaagaatcctggctgtggaaaga
tacctaaaggatcaacagctcctggggatttggggttgctctggaaaactcatttgcaccactgctgtgccttggaatgctagt
tggagtaataaatctctggaacagatttggaatcacacgacctggatggagtgggacagagaaattaacaattacacaa
gcttaatacactccttaattgaagaatcgcaaaaccagcaagaaaagaatgaacaagaattattggaattagataaatgg
gcaagtttgtggaattggtttaacataacaaattggctgtggtatataaaattattcataatgatagtaggaggcttggtaggttt
aagaatagtttttgctgtactttctatagtgaatagagttaggcagggatattcaccattatcgtttcagacccacctcccaacc
ccgaggggacccgacaggcccgaaggaatagaagaagaaggtggagagagagacagagacagatccattcgatta
gtgaacggatcggcactgcgtgcgccaattctgcagacaaatggcagtattcatccacaattttaaaagaaaaggggggg
attgggggtacagtgcaggggaaagaatagtagacataatagcaacagacatacaaactaaagaattacaaaaaca
aattacaaaaattcaaaattttcgggtttattacagggacagcagagatccagtttggttaattaaggtaccgagggcctattt
cccatgattccttcatatttgcatatacgatacaaggctgttagagagataattagaattaatttgactgtaaacacaaagata
ttagtacaaaatacgtgacgtagaaagtaataatttcttgggtagtttgcagttttaaaattatgttttaaaatggactatcatatg
cttaccgtaacttgaaagtatttcgatttcttggctttatatatcttgtggaaaggacgaaacaccgNNNNNNNNNNNN
NNNNNNNNgttttagagctagaaatagcaagttaaaataaggctagtccgttatcaacttgaaaaagtggcaccgag
tcggtgctttttttgaattcgctagctaggtcttgaaaggagtgggaattggctccggtgcccgtcagtgggcagagcgcacat
cgcccacagtccccgagaagttgggggggagggtcggcaattgatccggtgcctagagaaggtggcgcggggtaaac
tgggaaagtgatgtcgtgtactggctccgccttttttcccgagggtgggggagaaccgtatataagtgcagtagtcgccgtga
acgttctttttcgcaacgggtttgccgccagaacacaggaccggttctagagcgctgccaccatggacaagaagtacagc
atcggcctggacatcggcaccaactctgtgggctgggccgtgatcaccgacgagtacaaggtgcccagcaagaaattc
aaggtgctgggcaacaccgaccggcacagcatcaagaagaacctgatcggagccctgctgttcgacagcggcgaaa
cagccgaggccacccggctgaagagaaccgccagaagaagatacaccagacggaagaaccggatctgctatctgc
aagagatcttcagcaacgagatggccaaggtggacgacagcttcttccacagactggaagagtccttcctggtggaaga
ggataagaagcacgagcggcaccccatcttcggcaacatcgtggacgaggtggcctaccacgagaagtaccccacca
tctaccacctgagaaagaaactggtggacagcaccgacaaggccgacctgcggctgatctatctggccctggcccacat
gatcaagttccggggccacttcctgatcgagggcgacctgaaccccgacaacagcgacgtggacaagctgttcatccag
ctggtgcagacctacaaccagctgttcgaggaaaaccccatcaacgccagcggcgtggacgccaaggccatcctgtct
gccagactgagcaagagcagacggctggaaaatctgatcgcccagctgcccggcgagaagaagaatggcctgttcgg
aaacctgattgccctgagcctgggcctgacccccaacttcaagagcaacttcgacctggccgaggatgccaaactgcag
ctgagcaaggacacctacgacgacgacctggacaacctgctggcccagatcggcgaccagtacgccgacctgtttctg
gccgccaagaacctgtccgacgccatcctgctgagcgacatcctgagagtgaacaccgagatcaccaaggcccccctg

agcgcctctatgatcaagagatacgacgagcaccaccaggacctgaccctgctgaaagctctcgtgcggcagcagctg
cctgagaagtacaaagagatttttcttcgaccagagcaagaacggctacgccggctacattgacggcggagccagccag
gaagagttctacaagttcatcaagcccatcctggaaaagatggacggcaccgaggaactgctcgtgaagctgaacaga
gaggacctgctgcggaagcagcggaccttcgacaacggcagcatcccccaccagatccacctgggagagctgcacg
ccattctgcggcggcaggaagatttttacccattcctgaaggacaaccgggaaaagatcgagaagatcctgaccttccgc
atcccctactacgtgggccctctggccaggggaaacagcagattcgcctggatgaccagaaagagcgaggaaaccat
cacccccctggaacttcgaggaagtggtggacaagggcgcttccgcccagagcttcatcgagcggatgaccaacttcgat
aagaacctgcccaacgagaaggtgctgcccaagcacagcctgctgtacgagtacttcaccgtgtataacgagctgacca
aagtgaaatacgtgaccgagggaatgagaaagcccgccttcctgagcggcgagcagaaaaaggccatcgtggacct
gctgttcaagaccaaccggaaagtgaccgtgaagcagctgaaagaggactacttcaagaaaatcgagtgcttcgactcc
gtggaaatctccggcgtggaagatcggttcaacgcctccctgggcacataccacgatctgctgaaaattatcaaggacaa
ggacttcctggacaatgaggaaaacgaggacattctggaagatatcgtgctgaccctgacactgtttgaggacagagag
atgatcgaggaacggctgaaaacctatgcccacctgttcgacgacaaagtgatgaagcagctgaagcggcggagata
caccggctggggcaggctgagccggaagctgatcaacggcatccgggacaagcagtccggcaagacaatcctggatt
tcctgaagtccgacggcttcgccaacagaaacttcatgcagctgatccacgacgacagcctgacctttaaagaggacatc
cagaaagcccaggtgtccggccagggcgatagcctgcacgagcacattgccaatctggccggcagccccgccattaa
gaagggcatcctgcagacagtgaaggtggtggacgagctcgtgaaagtgatgggccggcacaagcccgagaacatc
gtgatcgaaatggccagagagaaccagaccacccagaagggacagaagaacagccgcgagagaatgaagcggat
cgaagagggcatcaaagagctgggcagccagatcctgaaagaacaccccgtggaaaacacccagctgcagaacga
gaagctgtacctgtactacctgcagaatgggcgggatatgtacgtggaccaggaactggacatcaaccggctgtccgact
acgatgtggaccatatcgtgcctcagagctttctgaaggacgactccatcgacaacaaggtgctgaccagaagcgacaa
gaaccggggcaagagcgacaacgtgccctccgaagaggtcgtgaagaagatgaagaactactggcggcagctgctg
aacgccaagctgattacccagagaaagttcgacaatctgaccaaggccgagagaggcggcctgagcgaactggataa
ggccggcttcatcaagagacagctggtggaaacccggcagatcacaaagcacgtggcacagatcctggactcccgga
tgaacactaagtacgacgagaatgacaagctgatccgggaagtgaaagtgatcaccctgaagtccaagctggtgtccg
atttccggaaggatttccagttttacaaagtgcgcgagatcaacaactaccaccacgcccacgacgcctacctgaacgcc
gtcgtgggaaccgccctgatcaaaaagtaccctaagctggaaagcgagttcgtgtacggcgactacaaggtgtacgacg
tgcggaagatgatcgccaagagcgagcaggaaatcggcaaggctaccgccaagtacttcttctacagcaacatcatga
acttttcaagaccgagattaccctggccaacggcgagatccggaagcggcctctgatcgagacaaacggcgaaaccg
gggagatcgtgtgggataagggccgggattttgccaccgtgcggaaagtgctgagcatgccccaagtgaatatcgtgaa
aaagaccgaggtgcagacaggcggcttcagcaaagagtctatcctgcccaagaggaacagcgataagctgatcgcca
gaaagaaggactgggaccctaagaagtacggcggcttcgacagccccaccgtggcctattctgtgctggtggtggccaa
agtggaaaagggcaagtccaagaaactgaagagtgtgaaagagctgctggggatcaccatcatggaaagaagcagc
ttcgagaagaatcccatcgactttctggaagccaagggctacaaagaagtgaaaaaggacctgatcatcaagctgccta
agtactccctgttcgagctggaaaacggccggaagagaatgctggcctctgccggcgaactgcagaagggaaacgaa
ctggccctgccctccaaatatgtgaacttcctgtacctggccagccactatgagaagctgaagggctcccccgaggataat
gagcagaaacagctgtttgtggaacagcacaagcactacctggacgagatcatcgagcagatcagcgagttctccaag
agagtgatcctggccgacgctaatctggacaaagtgctgtccgcctacaacaagcaccgggataagcccatcagagag
caggccgagaatatcatccacctgtttaccctgaccaatctgggagcccctgccgccttcaagtactttgacaccaccatcg
accggaagaggtacaccagcaccaaagaggtgctggacgccaccctgatccaccagagcatcaccggcctgtacga
gacacggatcgacctgtctcagctgggaggcgacaagcgacctgccgccacaaagaaggctggacaggctaagaag
aagaaagattacaaagacgatgacgataagggatccggcgcaacaaacttctctctgctgaaacaagccggagatgtc
gaagagaatcctggaccgatggtgagcaagggcgaggagctgttcaccggggtggtgcccatcctggtcgagctggac
ggcgacgtaaacggccacaagttcagcgtgtccggcgagggcgagggcgatgccacctacggcaagctgaccctga
agttcatctgcaccaccggcaagctgcccgtgccctggcccaccctcgtgaccaccctgacctacggcgtgcagtgcttca
gccgctaccccgaccacatgaagcagcacgacttcttcaagtccgccatgcccgaaggctacgtccaggagcgcacca

tcttcttcaaggacgacggcaactacaagacccgcgccgaggtgaagttcgagggcgacaccctggtgaaccgcatcg
agctgaagggcatcgacttcaaggaggacggcaacatcctggggcacaagctggagtacaactacaacagccacaa
cgtctatatcatggccgacaagcagaagaacggcatcaaggtgaacttcaagatccgccacaacatcgaggacggca
gcgtgcagctcgccgaccactaccagcagaacacccccatcggcgacggccccgtgctgctgcccgacaaccactac
ctgagcacccagtccgccctgagcaaagaccccaacgagaagcgcgatcacatggtcctgctggagttcgtgaccgcc
gccgggatcactctcggcatggacgagctgtacaagtaacacgcgttaagtcgacaatcaacctctggattacaaaatttg
tgaaagattgactggtattcttaactatgttgctccttttacgctatgtggatacgctgctttaatgcctttgtatcatgctattgcttc
ccgtatggctttcattttctcctccttgtataaatcctggttgctgtctctttatgaggagttgtggcccgttgtcaggcaacgtggc
gtggtgtgcactgtgtttgctgacgcaacccccactggttggggcattgccaccacctgtcagctcctttccgggactttcgctt
tcccccctccctattgccacggcggaactcatcgccgcctgccttgcccgctgctggacaggggctcggctgttgggcactg
acaattccgtggtgttgtcggggaaatcatcgtcctttccttggctgctcgcctgtgttgccacctggattctgcgcgggacgtc
cttctgctacgtcccttcggccctcaatccagcggaccttccttcccgcggcctgctgccggctctgcggcctcttccgcgtctt
cgccttcgccctcagacgagtcggatctccctttgggccgcctccccgcgtcgactttaagaccaatgacttacaaggcag
ctgtagatcttagccacttttaaaagaaaaggggggactggaagggctaattcactcccaacgaagacaagatctgctttt
tgcttgtactgggtctctctggttagaccagatctgagcctgggagctctctggctaactagggaacccactgcttaagcctc
aataaagcttgccttgagtgcttcaagtagtgtgtgcccgtctgttgtgtgactctggtaactagagatccctcagacccttttag
tcagtgtggaaaatctctagcagggcccgtttaaacccgctgatcagcctcgactgtgccttctagttgccagccatctgttgtt
tgcccctcccccgtgccttccttgaccctggaaggtgccactcccactgtcctttcctaataaaatgaggaaattgcatcgcat
tgtctgagtaggtgtcattctattctgggggggtggggtggggcaggacagcaaggggaggattgggaagacaatagca
ggcatgctggggatgcggtgggctctatggcttctgaggcggaaagaaccagctggggctctaggggtatccccacgc
gccctgtagcggcgcattaagcgcggcgggtgtggtggttacgcgcagcgtgaccgctacacttgccagcgccctagcg
cccgctcctttcgctttcttcccttcctttctcgccacgttcgccggctttccccgtcaagctctaaatcgggggctccctttagggt
tccgatttagtgctttacggcacctcgaccccaaaaaacttgattagggtgatggttcacgtagtgggccatcgccctgatag
acggtttttcgccctttgacgttggagtccacgttctttaatagtggactcttgttccaaactggaacaacactcaaccctatctc
ggtctattcttttgatttataagggattttgccgatttcggcctattggttaaaaaatgagctgatttaacaaaaatttaacgcgaa
ttaattctgtggaatgtgtgtcagttagggtgtggaaagtccccaggctccccagcaggcagaagtatgcaaagcatgcat
ctcaattagtcagcaaccaggtgtggaaagtccccaggctccccagcaggcagaagtatgcaaagcatgcatctcaatt
agtcagcaaccatagtcccgcccctaactccgcccatcccgcccctaactccgcccagttccgcccattctccgccccatg
gctgactaatttttttttatttatgcagaggccgaggccgcctctgcctctgagctattccagaagtagtgaggaggctttttttgga
ggcctaggcttttgcaaaaagctcccgggagcttgtatatccattttcggatctgatcagcacgtgttgacaattaatcatcgg
catagtatatcggcatagtataatacgacaaggtgaggaactaaaccatggccaagttgaccagtgccgttccggtgctc
accgcgcgcgacgtcgccggagcggtcgagttctggaccgaccggctcgggttctcccgggacttcgtggaggacgact
tcgccggtgtggtccgggacgacgtgaccctgttcatcagcgcggtccaggaccaggtggtgccggacaacaccctggc
ctgggtgtgggtgcgcggcctggacgagctgtacgccgagtggtcggaggtcgtgtccacgaacttccgggacgcctcc
gggccggccatgaccgagatcggcgagcagccgtgggggcgggagttcgccctgcgcgacccggccggcaactgcg
tgcacttcgtggccgaggagcaggactgacacgtgctacgagatttcgattccaccgccgccttctatgaaaggttgggctt
cggaatcgttttccgggacgccggctggatgatcctccagcgcggggatctcatgctggagttcttcgcccaccccaacttg
tttattgcagcttataatggttacaaataaagcaatagcatcacaaatttcacaaataaagcatttttttcactgcattctagttgt
ggtttgtccaaactcatcaatgtatcttatcatgtctgtataccgtcgacctctagctagagcttggcgtaatcatggtcatagct
gtttcctgtgtgaaattgttatccgctcacaattccacacaacatacgagccggaagcataaagtgtaaagcctggggtgcc
taatgagtgagctaactcacattaattgcgttgcgctcactgcccgctttccagtcgggaaacctgtcgtgccagctgcatta
atgaatcggccaacgcgcggggagaggcggtttgcgtattgggcgctcttccgcttcctcgctcactgactcgctgcgctcg
gtcgttcggctgcggcgagcggtatcagctcactcaaaggcggtaatacggttatccacagaatcaggggataacgcag
gaaagaacatgtgagcaaaaggccagcaaaaggccaggaaccgtaaaaaggccgcgttgctggcgtttttccatagg
ctccgccccctgacgagcatcacaaaaatcgacgctcaagtcagaggtggcgaaacccgacaggactataaagata
ccaggcgtttcccccctggaagctccctcgtgcgctctcctgttccgaccctgccgcttaccggatacctgtccgcctttctccct

tcgggaagcgtggcgctttctcatagctcacgctgtaggtatctcagttcggtgtaggtcgttcgctccaagctgggctgtgtg
cacgaacccccgttcagcccgaccgctgcgccttatccggtaactatcgtcttgagtccaacccggtaagacacgactta
tcgccactggcagcagccactggtaacaggattagcagagcgaggtatgtaggcggtgctacagagttcttgaagtggtg
gcctaactacggctacactagaagaacagtatttggtatctgcgctctgctgaagccagttaccttcggaaaaagagttggt
agctcttgatccggcaaacaaaccaccgctggtagcggtggtttttttgtttgcaagcagcagattacgcgcagaaaaaaa
ggatctcaagaagatcctttgatcttttctacggggtctgacgctcagtggaacgaaaactcacgttaagggattttggtcatg
agattatcaaaaaggatcttcacctagatccttttaaattaaaaatgaagttttaaatcaatctaaagtatatatgagtaaactt
ggtctgacagttaccaatgcttaatcagtgaggcacctatctcagcgatctgtctatttcgttcatccatagttgcctgactcccc
gtcgtgtagataactacgatacgggagggcttaccatctggccccagtgctgcaatgataccgcgagacccacgctcacc
ggctccagatttatcagcaataaaccagccagccggaagggccgagcgcagaagtggtcctgcaactttatccgcctcc
atccagtctattaattgttgccgggaagctagagtaagtagttcgccagttaatagtttgcgcaacgttgttgccattgctacag
gcatcgtggtgtcacgctcgtcgtttggtatggcttcattcagctccggttcccaacgatcaaggcgagttacatgatccccca
tgttgtgcaaaaaagcggttagctccttcggtcctccgatcgttgtcagaagtaagttggccgcagtgttatcactcatggttat
ggcagcactgcataattctcttactgtcatgccatccgtaagatgcttttctgtgactggtgagtactcaaccaagtcattctga
gaatagtgtatgcggcgaccgagttgctcttgcccggcgtcaatacgggataataccgcgccacatagcagaactttaaa
agtgctcatcattggaaaacgttcttcggggcgaaaactctcaaggatcttaccgctgttgagatccagttcgatgtaaccca
ctcgtgcacccaactgatcttcagcatcttttactttcaccagcgtttctgggtgagcaaaaacaggaaggcaaaatgccgc
aaaaaagggaataagggcgacacggaaatgttgaatactcatactcttccttttcaatattattgaagcatttatcagggtta
ttgtctcatgagcggatacatatttgaatgtatttagaaaaataaacaaatagggttccgcgcacatttccccgaaaagtgc
cacctgacgtcgacggatcgggagatctcccgatcccctatggtgcactctcagtacaatctgctctgatgccgcatagtta
agccagtatctgctccctgcttgtgtgttggaggtcgctgagtagtgcgcgagcaaaatttaagctacaacaaggcaaggc
ttgaccgacaattgcatgaagaatctgcttagggttaggcgttttgcgctgcttcgcgatgtacgggccagatatacgcgttg
acattgattattgactagttattaatagtaatcaattacggggtcattagttcatagcccatatatggagttccgcgttacataact
tacggtaaatggcccgcctggctgaccgcccaacgacccccgcccattgacgtcaataatgacgtatgttcccatagtaa
cgccaatagggactttccattgacgtcaatgggtggagtatttacggtaaactgcccacttggcagtacatcaagtgtatcat
atgccaagtacgcccccctattgacgtcaatgacggtaaatggcccgcctggcattatgcccagtacatgaccttatgggact
ttcctacttggcagtacatctacgtattagtcatcgctattaccatgg

3.7.4 List of Guide RNA Sequences in Targeted Library

Listed below are the sequences associated with the 74 elements in the targeted library transduced into the Med411 PDX medulloblastoma cells.

Table 3.2: Guide RNA sequences in Targeted CRISPRko Library.

Targeted Gene	gRNA Sequence	Targeted Gene	gRNA Sequence
ABL1	GAGCGTGGTGATGAGCCCGT	JAK3	GGAAGCTGTCAAAGTCCTGG
ABL2	CTGCTGCCCCGGATCCCGCG	KDR	ACACCTGTGCAGCATCCAGT
ADA	ATAGCCTCCCGGCAGCCCCT	KIT	TTTGTCCAGGAACTGAGCAG
ALK	GATGCCCGAGAAGAAGGCGT	LCK	AGCCTTCGTAGGTAACCAGT
AR	AGGGTACCACACATCAGGTG	MAP2K1	TCTTACCCAGAAGCAGAAGG
BCL2	GCTGAGCGCAGGCCCCGCGG	MAP2K2	GTAGGGTTGATGGTGAGCGC
BRAF	GGGCCAGGCTCTGTTCAACG	MET	GCTAATCTTGGGACATCAGA
BTK	CTGTGTTTGCTAAATCCACA	mTOR	AATAGGGTGAATGATCCGGG
CDK4	GTCTACATGCTCAAACACCA	PARP1	GCAGAAAGTCAAGAAGACAG
CDK6	CCAGCAGTACGAATGCGTGG	PDGFRa	GTAACCTTACACAACAGTGA
CSF1R	GCATGGCTTCACCATCCACA	PDGFRb	AAAGGCCATCAACATCACCG
CSF3R	GTGCCCCTGGAGGAAGACAG	PIGF	AAGTTCTCCAAGAAGAGTGA
CYP17A1	GTCACTCCGGAATTTCTCCT	PIK3CD	ACAAGGAGTCAAACTCGTGG
CYP19A1	AATCTGCCGTGGGAGATGAG	PSMB5	CATGTTGGCAAGCAGTTTGG
DHFR	CGGCCCGGCAGATACCTGAG	RARA	GATCTGGTCGGCGATGGTGA
DNMT1	CCTGTTCTCTTTCAAGACCA	RET	CGGTGAGCAGGGGAAAGCCG
DNMT3a	AGGATGTGACACTCACCGGG	ROS1	AGGCTGTGTCTGTAGTACAA
DNMT3b	GATCGAGTCTTCCCTCCCGC	SMO	GGACATGCACAGCTACATCG
EGFR	CTCTTCTTAGACCATCCAGG	SRC	TGTCCTTCAAGAAAGGCGAG
EPHA2	GGTCCGACTCGGCATAGTAG	TOP1	TTATGGATAACCACAAAGAG
ERBB2	CAGAACCTGCAAGTAATCCG	TOP2A	GCCTTCCTGAATTTGAAGAG
ESR1	GCACCATTGATAAAAACAGG	TOP2B	TGTAGGAATGAATTGCAGGG
FGFR1	GATCATCATCTATTGCACAG	TYMS	CCTGCATGCCGAATACCGAC
FGFR2	AGTGTGGTCCCATCTGACAA	VEGFA	GCTCTACCTCCACCATGCCA
FGFR3	GCTGCCGGCCAACCAGACGG	VEGFB	GCAGCAGGCGGCGGAGCAGA
FLT1	TCAGGGATCAAAGTGTCAAG	YES1	TTGAATCCTGGAAATCAACG
FLT3	GAGACAGGAAATGTTCCCTG	MYC	CTTCGGGGAGACAACGACGG
FLT4	CCTTTGACTGGGACTACCCA	PRKDC	CTCCATAATCCGGACCACAA
FYN	TTGTCCTTTGGAAACCCAAG	BRD4	CCAGACCCCTGTCATGACAG
GART	TGGCCTTCACAACCAAAGCA	AAVS1-A	CCTGCAACAGATCTTTGATG
HDAC1	GGAAGAGGCCTTCTACACCA	AAVS1-B	GGTCCAAACTTAGGGATGTG
HDAC2	TGGGTCATGCGGATTCTATG	AAVS1-C	AGTACAGTTGGGAAACAACT
HDAC3	GGGGTCGTAGAAATAGGCCA	AAVS1-D	GGCCATTCCCGGCCTCCCTG
IDH1	ACCCATCCACTCACAAGCCG	NTC-A	AAAAAGCTTCCGCCTGATGG
IDH2	GGGCATGTACAACACCGACG	NTC-B	AACTAGCCCGAGCAGCTTCG
JAK1	TATGTTGTGGACGATCAACG	NTC-C	AAGTGACGGTGTCATGCGGG
JAK2	CTGCCACTGCAATACCAACG	NTC-D	AATATTTGGCTCGGCTGCGC

3.7.5 Primer Sequences for Amplification of Integrated sgRNA from gDNA

Listed below are the specific primer sequences used to amplify guide RNA regions during PCR amplification and library preparation of the targeted screen samples. Primer sequences were designed to contain one region complementary to the guide RNA scaffold that would allow direct amplification of the integrated gRNA region from genomic DNA, and an overhang region complementary to adapters and indices used for multiplexing on Illumina Sequencing Instrument Workflows.

Forward Primer
ACACTCTTTCCCTACACGACGCTCTTCCGATCTATCTTGTGGAAAGGACGAAACAC
CG

Reverse Primer
GACTGGAGTTCAGACGTGTGCTCTTCCGATCTGTACACGACATCACTTTCCCAGTT
T

Chapter 4: Engineering Lineage-Specific Teratomas via Material Microenvironment

4.1 Abstract

Recent advances in stem cell technologies have allowed for significant progress in organotypic engineering. However, organotypic models remain limited by biological differences between 2D and organoid cultures relative to in vivo tissue environments. In this final chapter we extend previous findings regarding the impact of materials on replicating cancer biology, and apply it in an *in vivo* context to promote lineage-specific differentiation of stem cells during teratoma development. We initiated teratoma growth in a variety of natural and synthetic materials including collagen, fibrin, gelatin methacryloyl, polyethylene glycol, hyaluronic acid, gelatin, Matrigel, along with various blends of multiple materials. We then examined their impact on development and differentiation using a combination of transcriptomic profiling and computational cell-sorting algorithms. Our findings suggest that specific combinations of materials, namely formulations of high-stiffness fibrin and blends of fibrin with hyaluronic acid, could respectively bias differentiation down cardiac and neural lineages. This validates a proof-of-concept of the importance of the stem cell microenvironment and matrix composition for downstream differentiation, and suggests that materials can be applied further from *in vitro* to *in vivo* organotypic engineering.

4.2 Introduction

Historically, teratomas have been viewed in the context of two major functionalities. The first is as a major obstacle in stem-cell based regenerative therapies. Teratomas have long been understood to grow from cells with pluripotent differentiation capacity[187,188], but more recently, they have been the unwanted byproduct of efforts at therapeutic stem cell transplants, with preclinical tests often resulting in uncontrollable teratoma formation[189–191]. The second is as a method of verifying cell pluripotency of human stem cells, due to their ability to form mature tissue types from endodermal, mesodermal, and ectodermal germ layers[192]. Specifically, cells exhibiting pluripotency are injected into immunodeficient mice, where they differentiate in a random fashion into various lineages, often resulting in a mixture of tissue types derived from all three germ layers[192–194]. Were this random differentiation controlled however, teratomas could provide additional utility as a functional model of specific tissue types.

In this context, developmental biologists have long sought to understand the key parameters that influence stem cell differentiation, especially in a 3D environment[195,196]. Understanding these parameters is vital for organotypic tissue engineering and developmental biology research. Researchers have exhaustively explored directed differentiation of stem cells in 2D culture, producing a wide range of tissue-specific cells[197–202]. Despite this, it is well-understood that major differences exist between *in vivo* tissue and 2D monolayers, with most 2D cultures failing to reproduce key aspects of human biology[203]. As such, much of this work has been extended into 3D models, with particularly towards the generation of tissue-specific organoid systems from pluripotent stem cells[52,204–207]. Recently, efforts have even been made towards directing stem cell

differentiation in vivo through the use of microRNA-based targeting, in which synthetic micro-RNA-responsive constructs were used to enrich cells of specific lineages during teratoma development, resulting in overrepresentation of pre-determined tissues[208].

Building on these advancements, we believe that one worthwhile avenue that has yet to be explored, is the use of a biomaterials-based approach in an *in vivo* context. Researchers have modulated biomaterials previously to assess regulatory effects on stem cell fate[209,210], and our prior work highlights the importance of the material environment of various tissue-specific cancer subtypes. As such, we now utilize a materials-based approach to enrich for desired lineages in teratomas. Specifically, teratomas were assayed under multiple unique matrix conditions to assess cell heterogeneity outcomes. In contrast to the established standard of pure Matrigel, we engineered a variety of unique microenvironments for teratoma growth from an assortment of natural and synthetic materials. These included materials known to be present at high levels in specific organs, such as hyaluronic acid in the brain[211], and materials that could be applied over a large range of concentrations. Fibrin in particular exists as a natural material with a highly tunable stiffness[212,213], which is vital, as another major factor known to impact stem cell differentiation is elastic modulus[214,215]. Taken together, combining our prior work in material optimizations with teratoma biology offers a unique opportunity in organotypic tissue engineering.

4.3 Methods

4.3.1 Cell Culture

H1 hESCs and HUES62 hESCs were cultured under feeder-free conditions in mTeSR1 medium (Stem Cell Technologies). Cells were passaged using Versene dissociation reagent (Thermo Fisher Scientific). Prior to each passage, tissue-culture plates were coated with growth factor-reduced Matrigel (Corning) diluted in DMEM/F12 medium (Thermo Fisher Scientific) at a ratio of 100 uL of Matrigel to 6 mL of medium. Following coating, plates were incubated for a minimum of 30 minutes at 37°C.

4.3.2 Material Preparation

Teratoma cells were encapsulated in matrices of 15 different compositions. Specifically, these included: Matrigel (5 mg/mL), collagen (5 mg/mL), fibrin (3, 20, or 40 mg/mL), a blended mixture of fibrin (3 or 20 mg/mL) and hyaluronic acid (2 mg/mL), a blended mixture of fibrin (3 or 20 mg/mL) and Matrigel (4 mg/mL), a blended mixture of fibrin (3 or 20 mg/mL), gelatin (10 mg/mL) and Matrigel (4 mg/mL), gelatin methacryloyl (5% or 10%), and polyethylene glycol (5% or 10%).

Matrigel and collagen matrices were allowed to incubate at 37°C to gelate with no additional components save mTeSR media. Blended matrices of fibrin, gelatin, and Matrigel were formulated with Matrigel (4 mg/mL), fibrinogen (3 or 20 mg/mL), gelatin (10 mg/mL), transglutaminase (2 mg/mL), $CaCl_2$ (2.5 mM), and thrombin (2 U/mL)[146]. Briefly, stock solutions of gelatin, $CaCl_2$, and thrombin were prepared prior to formulation. Type A porcine skin gelatin (Sigma-Aldrich) was dissolved overnight in water (15 wt/vol %) at 70 °C, buffered to pH 7.4 using 1 M NaOH, passed through a 0.22 mm filter (Millipore),

and stored at 4 °C. $CaCl_2$ was dissolved at 250 mM in Dulbecco's phosphate buffered saline (dPBS), and Thrombin (Sigma-Aldrich) was prepared at 500 U/mL, aliquoted, and stored at -20 °C. Solutions of both bovine plasma fibrinogen (Millipore) and transglutaminase (MooGloo) were dissolved in dPBS at 37 °C immediately prior to use, and at respective concentrations of 100 mg/mL and 50 mg/mL. During formulation, all components except Matrigel and thrombin were mixed and incubated at 37 °C for 20 minutes, after which Matrigel and thrombin were rapidly added. Blended matrices of fibrin and Matrigel were formulated identically, but with the absence of gelatin, transglutaminase, and $CaCl_2$. Matrices of fibrin alone were formulated identically, but in the additional absence of Matrigel, and with the addition of the high-concentration 40 mg/mL fibrin formulation. Blended matrices of fibrin and hyaluronic acid were formulated from fibrinogen (3 or 20 mg/mL), hyaluronic acid (2 mg/mL), and thrombin (2 U/mL). All components except hyaluronic acid were prepared as previously described. Hyaluronic acid (LifeCore) was prepared at a stock concentration of 10 mg/mL by stirring overnight in PBS at 4 °C. Matrices were prepared by directly mixing all components.

Gelatin methacryloyl 300-bloom (Millipore-Sigma) and polyethylene glycol diacrylate (Millipore-Sigma) were both prepared by dissolving respective components in dPBS to form stock 20% solutions, diluting with mTeSR to the appropriate concentrations, encapsulating cells, and exposing to a UV light source in the presence of Irgacure 2959 (Millipore-Sigma) initiator to induce radical polymerization.

4.3.3 Animal Work

4.3.3.1 Matrix Implantation

Mice were anesthetized using intraperitoneal administration of ketamine (75mg/kg) / xylazine (15mg/kg). Once the mouse was fully anesthetized, the right flank was shaved and sterilized with alternating swabs of 7.5% povidone-iodine and 10% USP povidone-iodine respectively (PDI PVP #S141125) followed by 70% isopropyl alcohol. A small incision was made on the right flank subcutaneously with small animal surgical scissors. Subcutaneous connective tissue was released via blunt dissection to create a small pocket for the hydrogel. Upon hydrogel placement, the incision was closed with standard 4-0 silk sutures (UNIFY® #S-S418R13). Sutures were removed 10-14 days post-op.

4.3.3.2 Mouse Maintenance

$Rag2^{-/-};gc^{-/-}$ immunodeficient mice used for orthotopic breast cancer models were maintained in animal facilities at the Powell-Focht Bioengineering Hall at the University of California San Diego. All experiments were performed in accordance with national guidelines and regulations, and with the approval of animal care and use committees at Sanford Burnham Prebys Medical Discovery Institute and the University of California San Diego.

4.3.4 Model Analysis

4.3.4.1 Histology

Sectioning and H&E staining was performed by the Moore's Cancer Center Histology Core. In brief, teratoma fragments were encapsulated in either Optimal Cutting

Temperature (O.C.T.), or paraffin wax. blocks were cut into 10 micron sections onto a positively charged glass slide. The slide was then stained with Harris hematoxylin and then rinsed in tap water and treated with an alkaline solution. The slide was then de-stained to remove non-specific background staining with a weak acid alcohol. The section was then stained with an aqueous solution of eosin and passed through several changes of alcohol, then rinsed in several baths of xylene. A thin layer of polystyrene mountant was applied, followed by a glass cover slip.

4.3.5 Genetic and Transcriptomic Analysis

4.3.5.1 Bulk RNA Extraction

Teratoma samples were frozen via LN2, then pulverized with a pestle and mortar until fully powderized. Powderized samples were resuspended in Qiazol (Qiagen) at a ratio of 900 uL Qiazol per 100 mg of original tissue, mixed with an 18-gauge syringe, and allowed to incubate on a shaker for approximately 30 minutes. Samples were centrifuged at 12000g at 4 °C for 10 minutes, and supernatant was collected. Chloroform (Fisher Scientific) was added to samples at a ratio of 180 uL chloroform per 900 uL supernatant. Samples were mixed and allowed to incubate for 10 minutes, then centrifuged at 12000g at 4 °C for 15 minutes to separate into aqueous and organic phases. The aqueous phase was collected, while the organic phase was discarded. Samples were diluted at a 1:1 ratio with 70% ethanol, and the remainder of the extraction was performed using the RNeasy Kit (Qiagen).

Following RNA extraction, approximately 1 ug of RNA from each condition was used to synthesize cDNA and construct a transcriptomic library using the NEBNext

poly(A) mRNA Magnetic Isolation Module (New England Biosystems) and NEBNext Ultra II RNA Library Prep Kit (New England Biosystems). Multiplex indexing was performed with NEB Multiplex Primers. The final product was purified using Ampure XP beads, pooled in equal ratios, and sequenced using the NovaSeq with paired end 100 bp reads.

4.3.6 Computational Analysis

4.3.6.1 Cell-Type Distribution Analysis

Reads were aligned to both human reference genome HG38 and mouse reference genome MM10 using STAR[149]. Resulting BAM files were processed using the XenofilteR analytical tool[150] to remove reads from transcripts from cells of the host mice. Read counts were then generated by mapping to reference transcriptome GenCode v33 using FeatureCounts. Prior single-cell sequencing data across seven teratomas was used to construct a signature matrix containing gene profiles associated with twenty-three different cell types identified within the teratomas by randomly sampling up to 200 cells from each cell type[208]. The CIBERSORTx analytical tool (https://cibersort.stanford.edu/)[216] was used to estimate abundances of each of the different cell types based on the read counts obtained from the transcriptomic libraries, and the gene profiles in the signature matrix.

4.3.6.2 Gene Ontology Pathway Analysis

Read counts were normalized in DESeq2[155] both across all samples for a given gene using the geometric mean, and within each sample using the median. Relative expression profiles and differentially expressed gene lists were subsequently generated

using the DESeq2 pipeline. Enriched and depleted pathways were identified using Metascape[151]. Differentially expressed genes were classified as genes with both |Zscore| > 2 and FDR < 0.1, were input into Metascape, and pathway lists were restricted to terms within the Gene Ontology Biological Process domain.

4.4 Results and Discussion

4.4.1 Cell-Type Distribution

To assess the potential of various material formulations to prime for certain cell types, we encapsulated H1 ESCs in the following 15 matrix conditions for downstream analysis: Matrigel (5 mg/mL), collagen (5 mg/mL), fibrin (3, 20, or 40 mg/mL), a blended mixture of fibrin (3 or 20 mg/mL) and hyaluronic acid (2 mg/mL), a blended mixture of fibrin (3 or 20 mg/mL) and Matrigel (4 mg/mL), a blended mixture of fibrin (3 or 20 mg/mL), gelatin (10 mg/mL) and Matrigel (4 mg/mL), gelatin methacryloyl (5% or 10%), and polyethylene glycol (5% or 10%) (**Fig. 4.1A-B**). Following implantation of each material in the right flank of $Rag2^{-/-};\gamma c^{-/-}$ immunodeficient mice teratomas were allowed to grow for up to 8 weeks until the tumors were of a sufficient size for extraction and downstream analyses. Post-extraction, tumors were divided in a semi-random fashion. Half of tissue was snap-frozen for bulk RNA extraction and sequencing, while the other half was encapsulated in either OCT or paraffin wax for sectioning and H&E staining. Of note, the collagen matrix condition did not form any appreciable tumor mass throughout the study. Additionally, all synthetic conditions (gelatin methacryloyl and polyethylene glycol) failed to form tumor tissue as well, and upon extraction (8 weeks) only the initial matrix was present with a surrounding fibrous capsule **(Fig. 4.1B**).

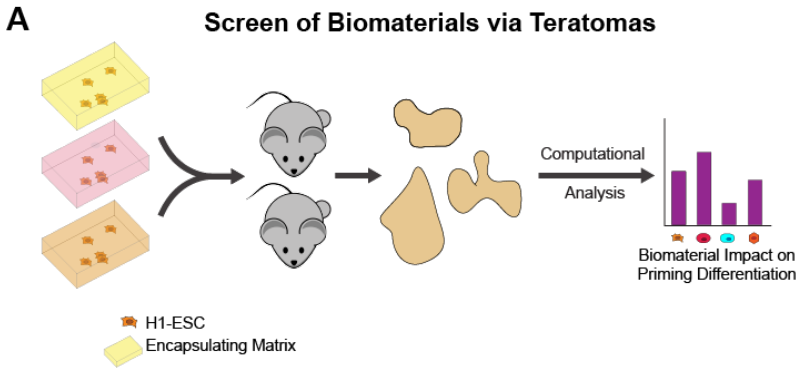

B

Material	Teratoma Formation
Matrigel	Y
Collagen	N
Fibrin (3 mg/mL)	Y
Fibrin (20 mg/mL)	Y
Fibrin (40 mg/mL)	Y
Matrigel/Fibrin (3 mg/mL)	Y
Matrigel/Fibrin (20 mg/mL)	Y
Gelatin/Matrigel/Fibrin (3 mg/mL)	Y
Gelatin/Matrigel/Fibrin (20 mg/mL)	Y
HA/Fibrin (3 mg/mL)	Y
HA/Fibrin (20 mg/mL)	Y
PEGDA (5%)	N
PEGDA (10%)	N
GelMA (5%)	N
GelMA (10%)	N

Figure 4.1: Effect of Biomaterial Environmental Composition on Teratoma Lineage Differentiation. **(A)** Schematic representation of the biomaterial screening procedure. H1-ESC cells are encapsulated in biomaterials of various compositions, then transplanted subcutaneously into immunodeficient mice and allowed to grow into teratomas. RNA is extracted, sequenced, and analyzed to determine the distribution of cell types within the teratoma. **(B)** Table displaying results of teratoma growth in different transplanted materials.

Upon obtaining cell-type distributions within each teratoma from analysis via the Cibersortx algorithm[216], we identified several materials of interest. Fibrin (40 mg/mL) showed an excess of muscle cell types, while the Hyaluronan/Fibrin (3 mg/mL and 20 mg/mL) conditions showed greater proportions of neural cell types, and the Gelatin/Matrigel/Fibrin (3 mg/mL) showed a large proportion of retinal cell types (**Fig. 4.2A, 4.2B**). Other material conditions yielded teratomas that were largely unremarkable relative to the Matrigel control.

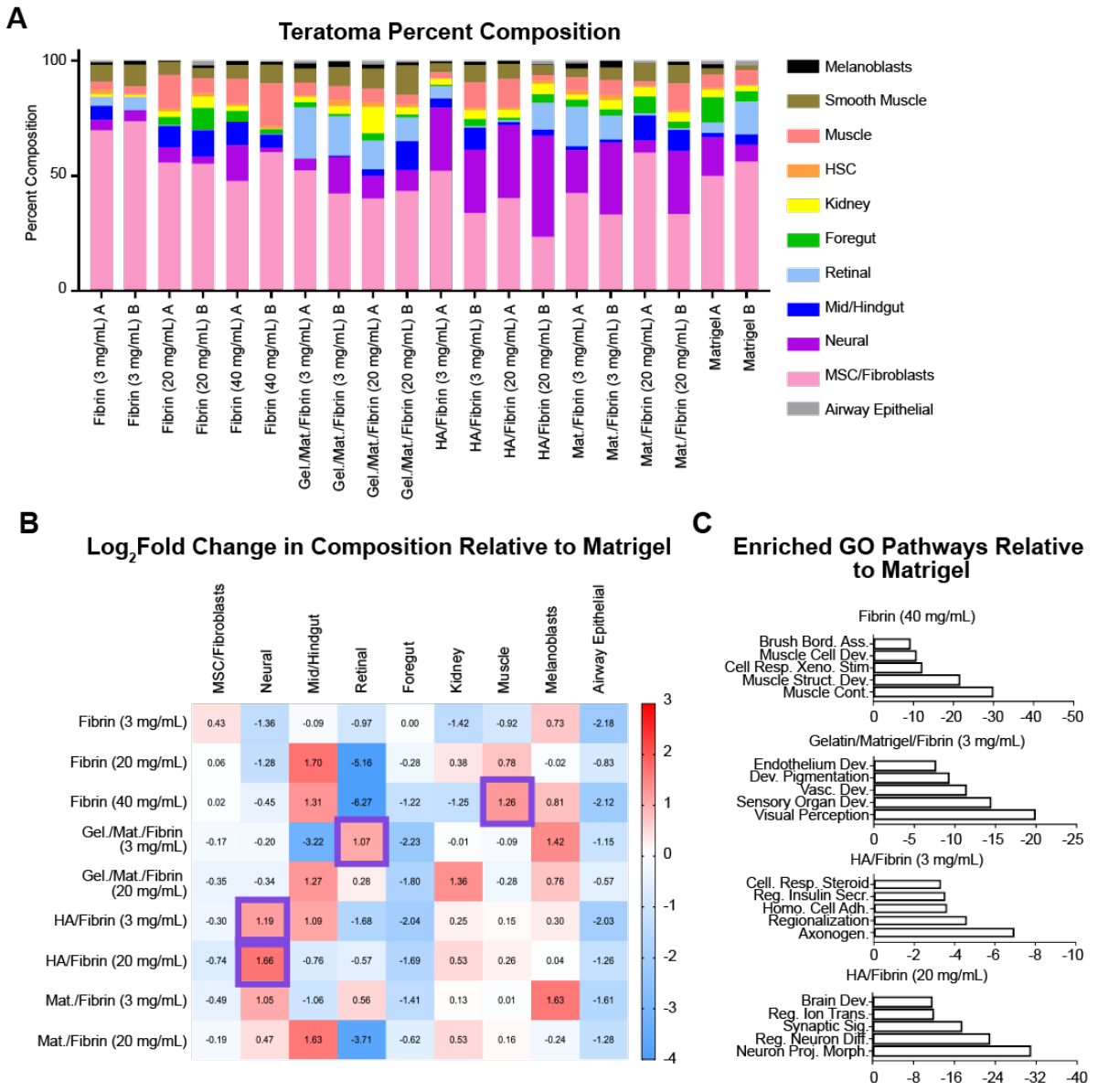

Figure 4.2: Cell Type Distributions and Pathway Enrichment Based on Material Environment. (A) Raw cell-type distributions in teratomas grown in various material conditions, determined by the Cibersortx algorithm. **(B)** Table comparing the distribution of cell types of teratomas grown from various material transplants relative to Matrigel controls obtained via Cibersortx. Data shows log_2fold change values of the percent composition of each cell type relative to their percent composition in Matrigel. **(C)** Top-5 Metascape-generated enriched (left) Gene Ontology Biological Process Pathways in major conditions of interest based on enriched cell types.

This was verified via histological analysis, with all material conditions being examined relative to the Matrigel control (**Fig. 4.3A**). Examination revealed a large

amount of retinal pigmented epithelium in the Gelatin/Matrigel/Fibrin (3 mg/mL) condition (**Fig. 4.3B**), an excess of cardiac muscle in the Fibrin (40 mg/mL) condition (**Fig. 4.4A**), and greater neural architectures in both Hyaluronan/Fibrin conditions (**Fig. 4.4B-C**).

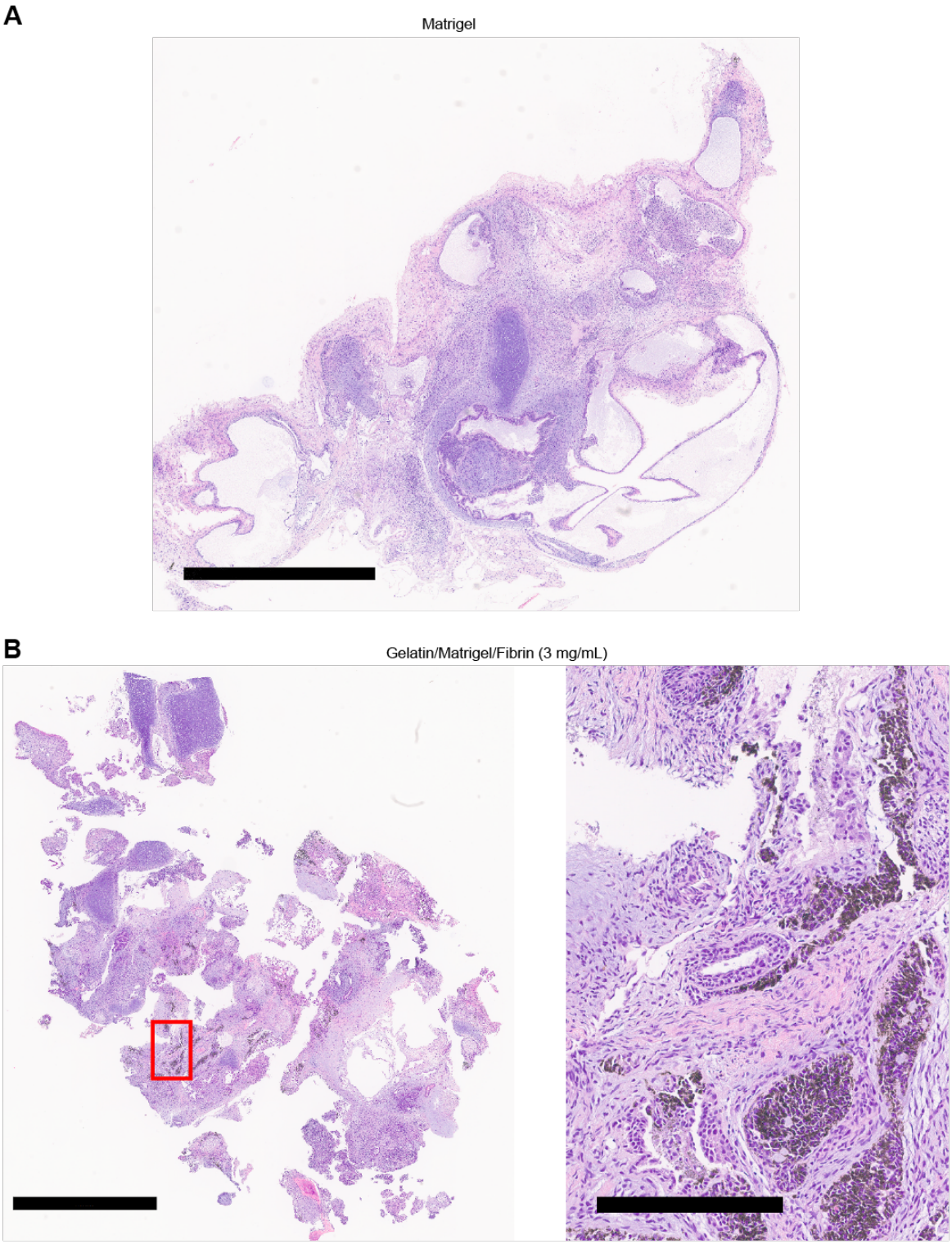

Figure 4.3: Hematoxylin and Eosin Staining of Teratomas. (A) Teratoma grown in Matrigel. Scale bar: 2 mm **(B)** Teratoma grown in a blend of Gelatin, Matrigel, and Fibrin (3 mg/mL) with zoomed images of regions containing a high level of retinal tissue. Scale bars: 2 mm (left) and 300 μm (right).

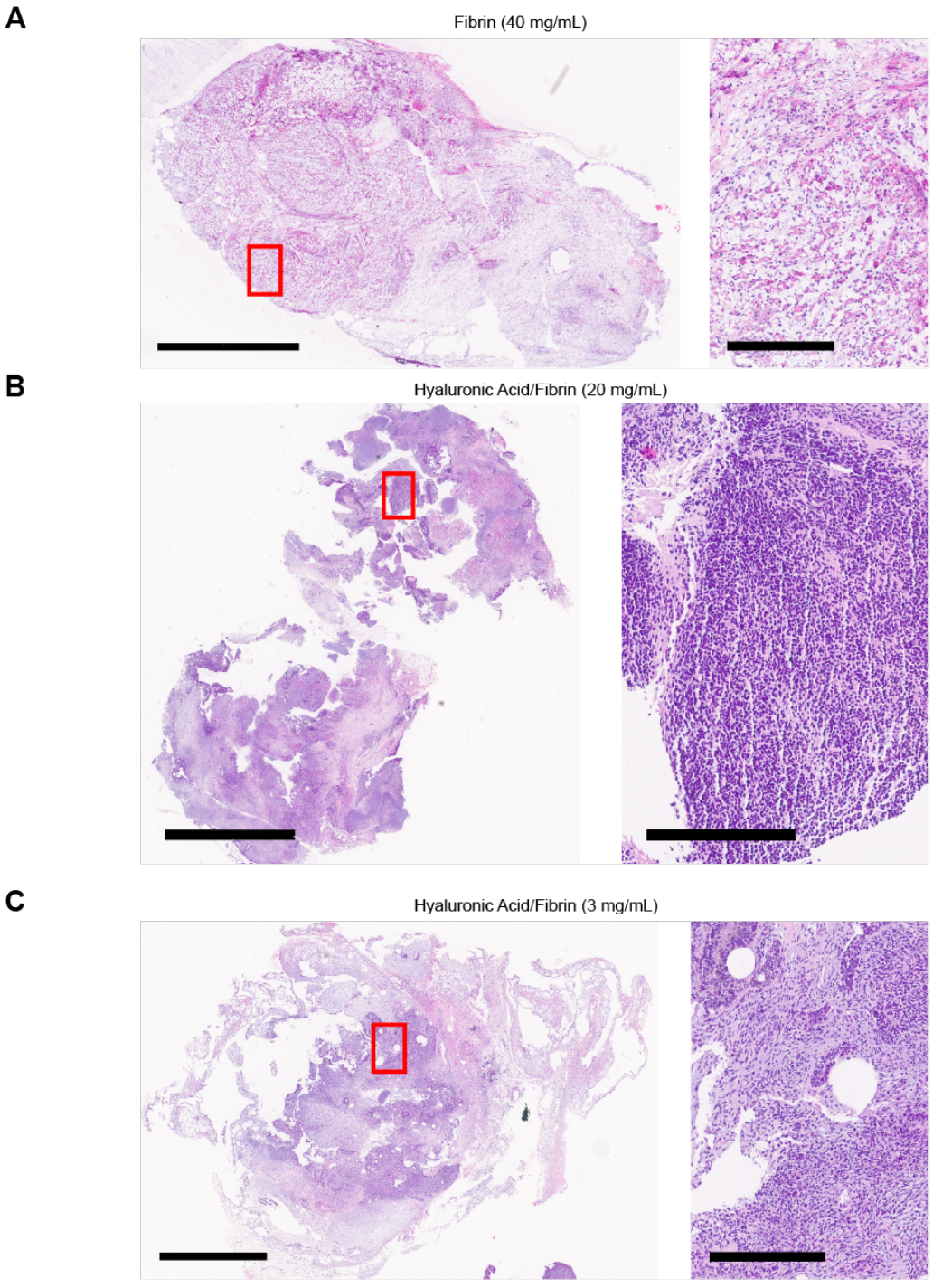

Figure 4.4: Hematoxylin and Eosin Staining of Teratomas. (A) Teratoma grown in Fibrin (40 mg/mL) with zoomed images of regions containing a high level of muscle tissue. **(B)** Teratoma grown in a blend of Hyaluronic Acid and Fibrin (20 mg/mL) with zoomed images of regions containing a high level of neural tissue. **(C)** Teratoma grown in a blend of Hyaluronic Acid and Fibrin (3 mg/mL) with zoomed image of region containing a high level of neural tissue. Scale bars: 2 mm (left) and 300 μm (right) for all.

These results were all confirmed via gene ontological analysis from bulk RNA sequencing data obtained from whole tissues of each material-teratoma compared to the Matrigel control (**Fig. 4.2C**). In particular, the Gelatin/Matrigel/Fibrin (3 mg/mL) condition had consistently upregulated gene ontology pathways for eye development, with the top-5 non-redundant pathways including visual perception, sensory organ development, and lens development. Both Hyaluronan/Fibrin conditions showed enriched pathways for various neuronal pathways, including neuron projection morphogenesis, brain development, and regulation of nervous system development. This result is reasonable with known biology as it is well known in the field that hyaluronic acid has a high water-retaining capacity that makes it a highly prevalent space-filling compound in the brain. Additionally, the Fibrin (40 mg/mL) condition showed enrichment in various muscle-related pathways, such as muscle system processes, regulation of calcium ion transport, and heart development. This result would be consistent with known biology of increased matrix stiffness (~9-11 kPa) leading to more muscular development.

4.4.2 Validation of Material Composition Effects

To ensure that results were reproducible, the entire previously-described set of experimentation and analysis was performed again for the four material types of interest in H1 hESCs, as well as for the Fibrin (40 mg/mL) and Hyaluronan/Fibrin materials in HUES62 hESCs (**Fig. 4.5A**). Broadly, major results obtained previously were replicated for all conditions (**Fig. 4.5B**).

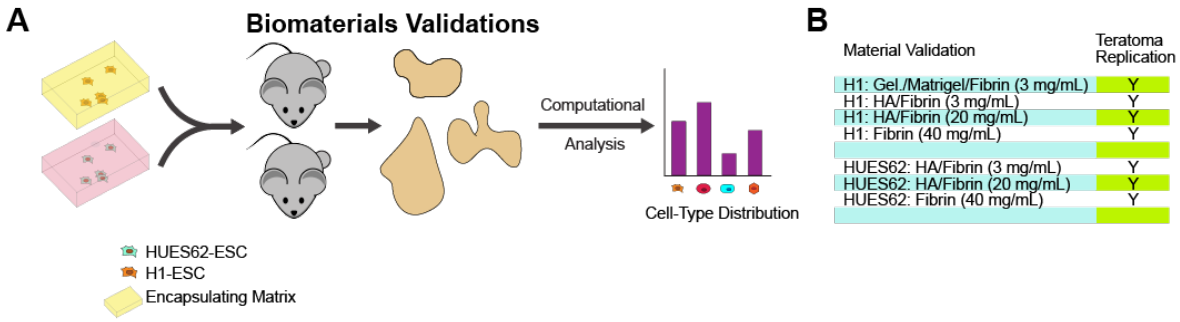

Figure 4.5: Validation of Effects of Biomaterial Environmental Composition on Teratoma Lineage Differentiation in H1 and HUES62 ESC. (A) Schematic representation of the biomaterial screening procedure. H1- or HUES62-ESC cells are encapsulated in biomaterials of interest determined by the previous screen, then transplanted subcutaneously into immunodeficient mice and allowed to grow into teratomas. RNA is extracted, sequenced, and analyzed to determine the distribution of cell types within the teratoma. **(B)** Table displaying results of teratoma growth in different transplanted materials, and whether or not results from initial screen were reproduced.

Results from the Cibersort algorithm again indicated enrichment of retinal cell types for H1 the teratomas grown in the Gelatin/Matrigel/Fibrin condition, enrichment of neural cell types for the H1 teratomas grown in the Hyaluronan/Fibrin condition, and enrichment of muscle cell types for the H1 teratomas grown in the Fibrin condition (**Fig. 4.6A**), all of which were expected based on previous results.

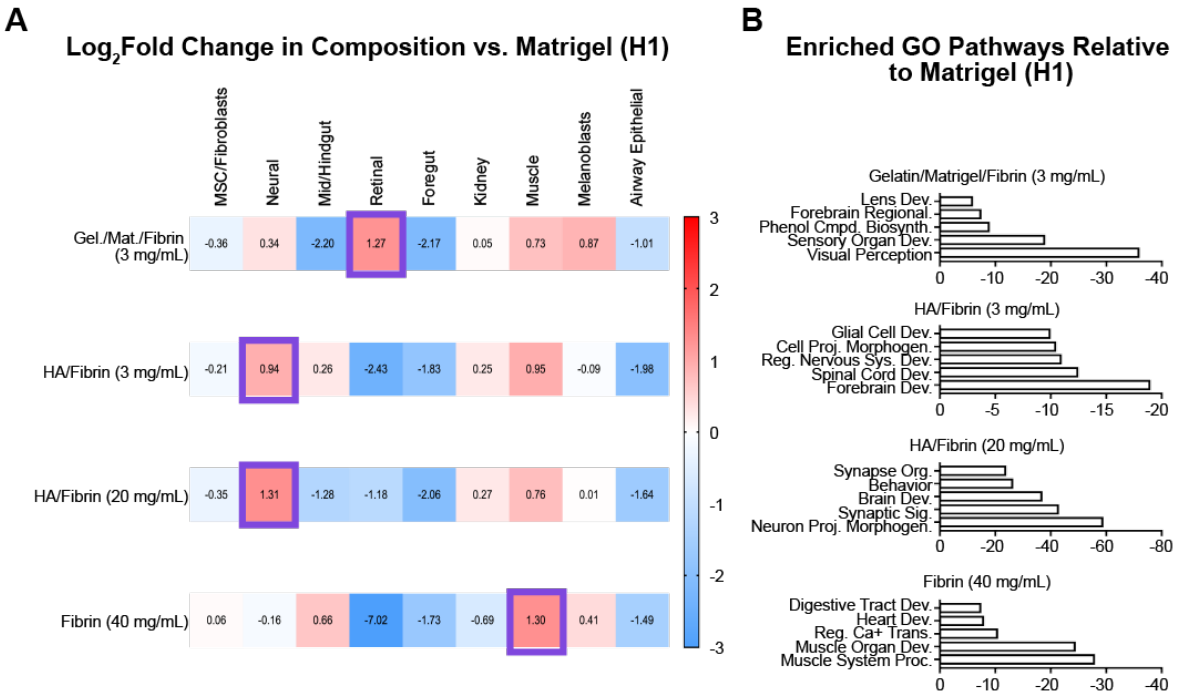

Figure 4.6: Cell Type Distributions and Pathway Enrichment Based on Material Environment for Validations in H1-ESC. (A) Table comparing the distribution of cell types of H1-ESC teratomas grown from various material transplants relative to Matrigel controls obtained via Cibersortx. Data shows log_2fold change values of the percent composition of each cell type relative to their percent composition in Matrigel. **(B)** Top-5 Metascape-generated enriched (left) Gene Ontology Biological Process Pathways in H1 teratomas of all conditions.

This was further backed by histological images showing the same (**Figs. 4.7-4.8**), and similarly enriched gene ontological pathways relative to the original run (**Fig. 4.6B**). Interestingly, nearly all conditions appeared to demonstrate some degree of muscle cell type enrichment, though the largest magnitude was still seen in the Fibrin (40 mg/mL) condition. Furthermore, rather than showing large amounts of skeletal and cardiac muscle as before (**Fig. 4.3A**), the validation condition appeared to show greater enrichment of smooth muscle (**Fig. 4.6B**). This is further reflected in the pathway analysis results, with digestive tract development appearing among the five most enriched pathways (**Fig.**

4.6B), though some of that contribution could also stem from the mild enrichment in cells of mid- and hindgut lineages.

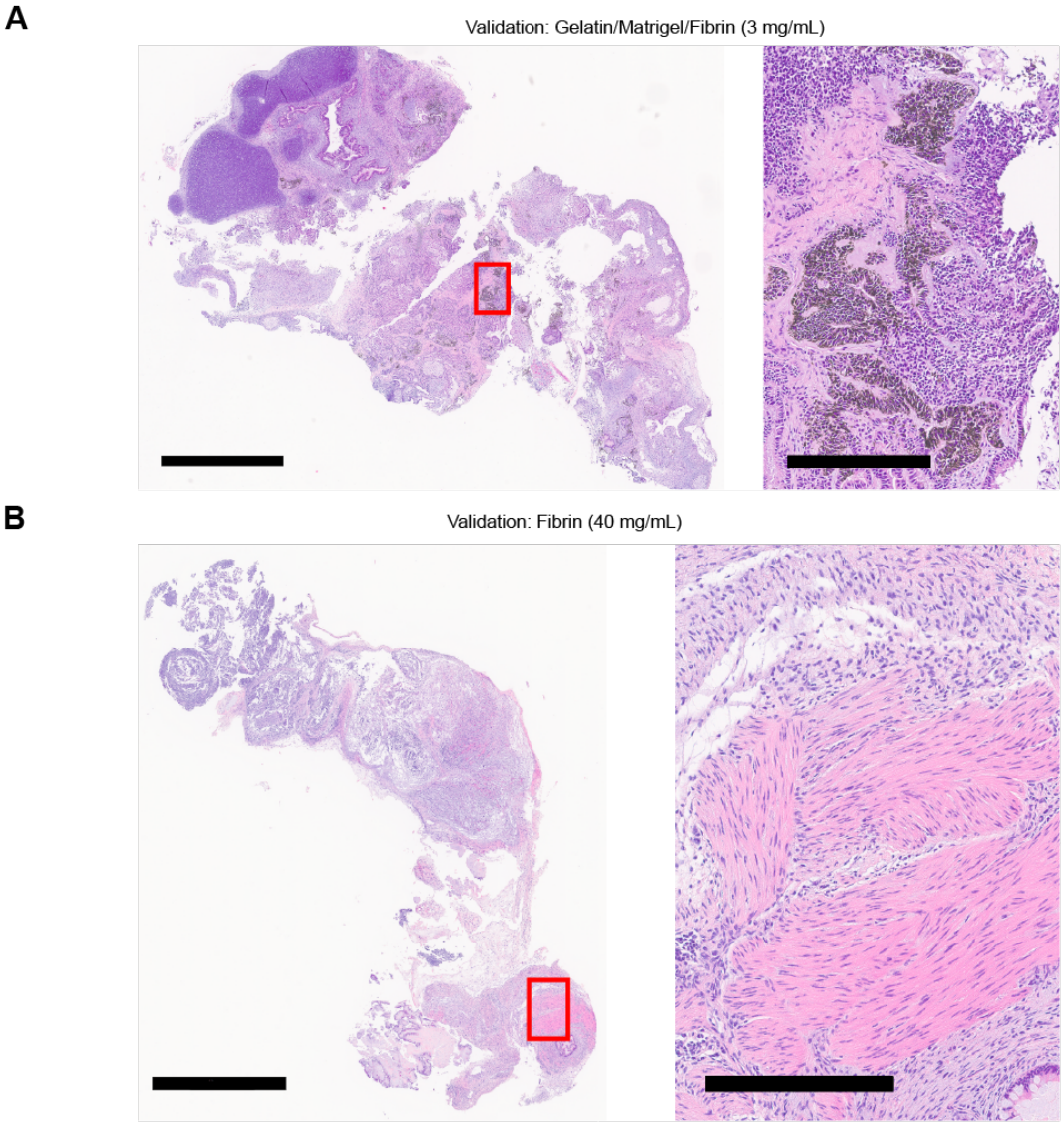

Figure 4.7: Hematoxylin and Eosin Staining of H1-ESC Validation Teratomas (I). (A) Teratoma grown in a blend of Gelatin, Matrigel, and Fibrin (3 mg/mL) with zoomed images of regions containing a high level of retinal tissue. **(B)** Teratoma grown in Fibrin (40 mg/mL) with zoomed image of region containing a high level of muscle tissue. Scale bars: 2 mm (left) and 300 μm (right) for all.

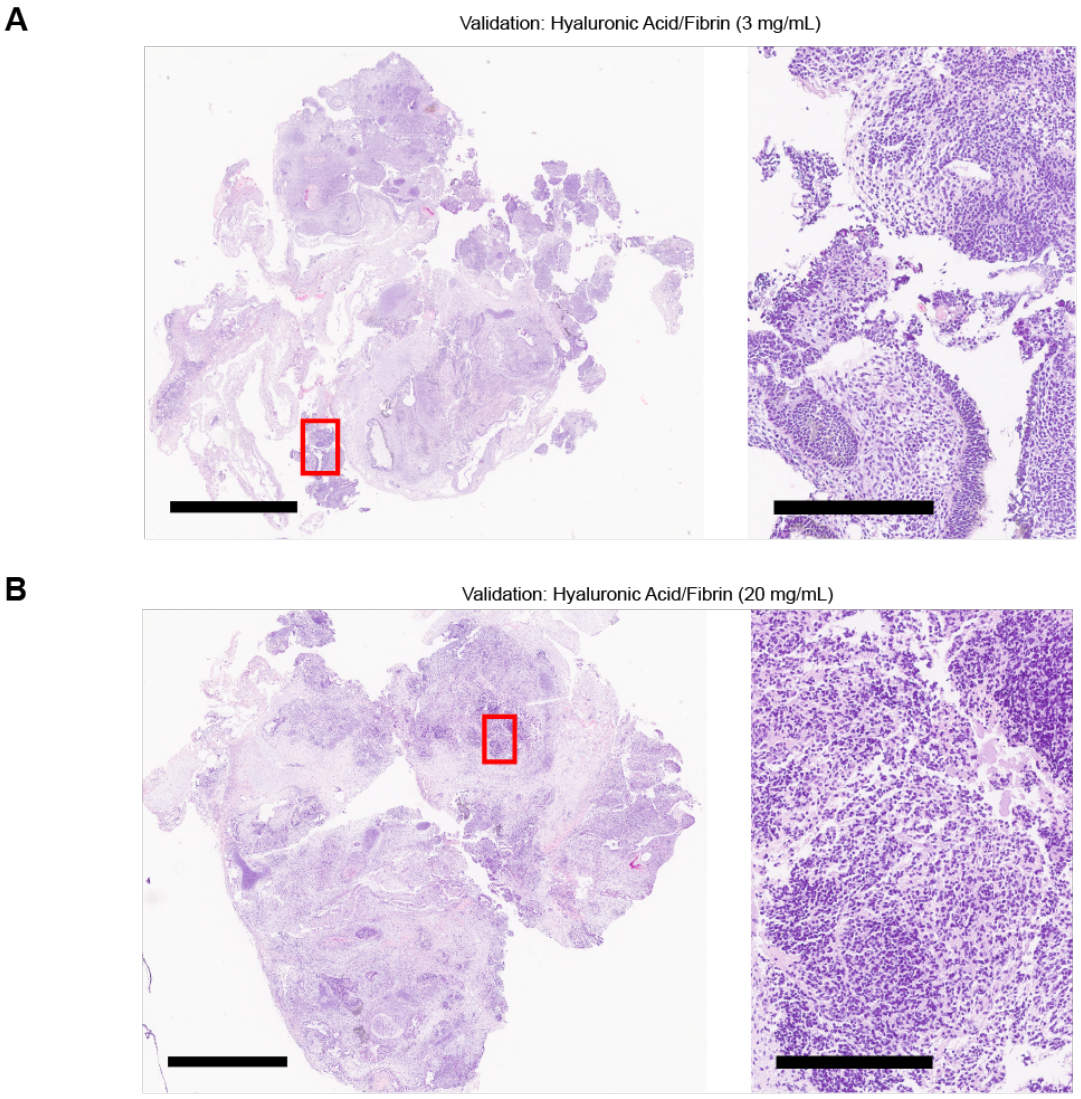

Figure 4.8: Hematoxylin and Eosin Staining of H1-ESC Validation Teratomas (II). (A) Teratoma grown in a blend of Hyaluronic Acid and Fibrin (3 mg/mL) with zoomed images of regions containing a high level of neural tissue. **(B)** Teratoma grown in a blend of Hyaluronic Acid and Fibrin (20 mg/mL) with zoomed image of region containing a high level of neural tissue. Scale bars: 2 mm (left) and 300 μm (right) for all.

Cibersort results for the HUES62 hESCs followed the same pattern, with neural cell types being enriched when grown in the Hyaluronan/Fibrin condition, while muscle cell types were again enriched when grown in the Fibrin condition (**Fig. 4.9A**). Of note, the degree of enrichment appeared to be slightly lower than what was seen for the H1 hESC validations.

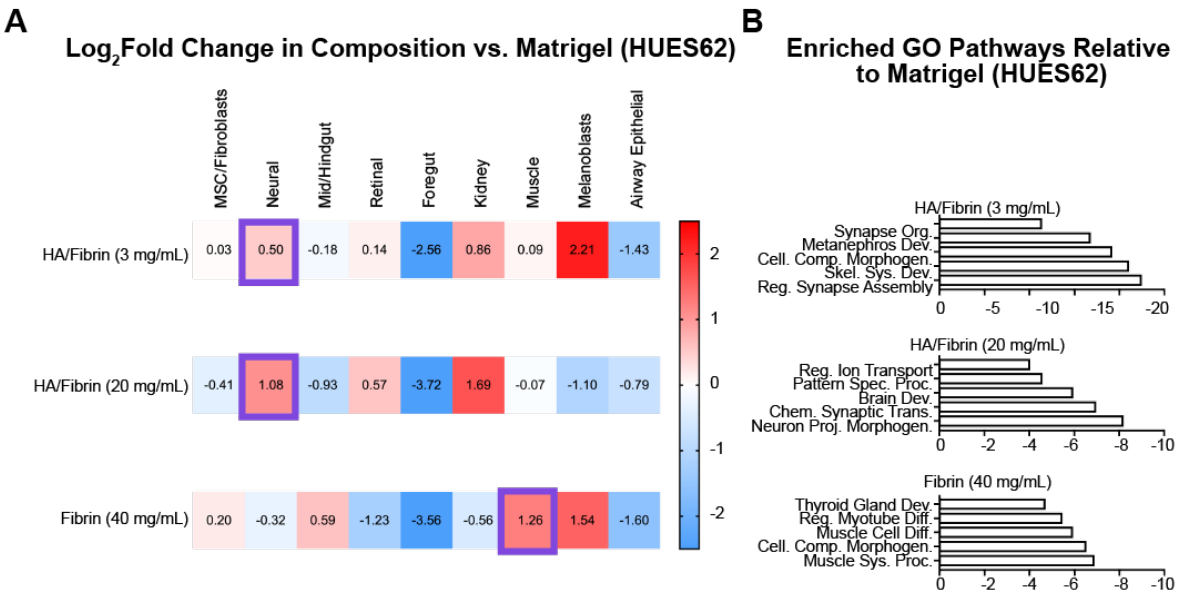

Figure 4.9: Cell Type Distributions and Pathway Enrichment Based on Material Environment for Validations in HUES62-ESC. (A) Table comparing the distribution of cell types of HUES62-ESC teratomas grown from various material transplants relative to Matrigel controls obtained via Cibersortx. Data shows log_2fold change values of the percent composition of each cell type relative to their percent composition in Matrigel. **(B)** Top-5 Metascape-generated enriched (left) Gene Ontology Biological Process Pathways in H1 teratomas of all conditions.

Again, histological images (**Fig. 4.10**) as well as enriched gene ontological pathways (**Fig. 4.9B**) reinforced these conclusions.

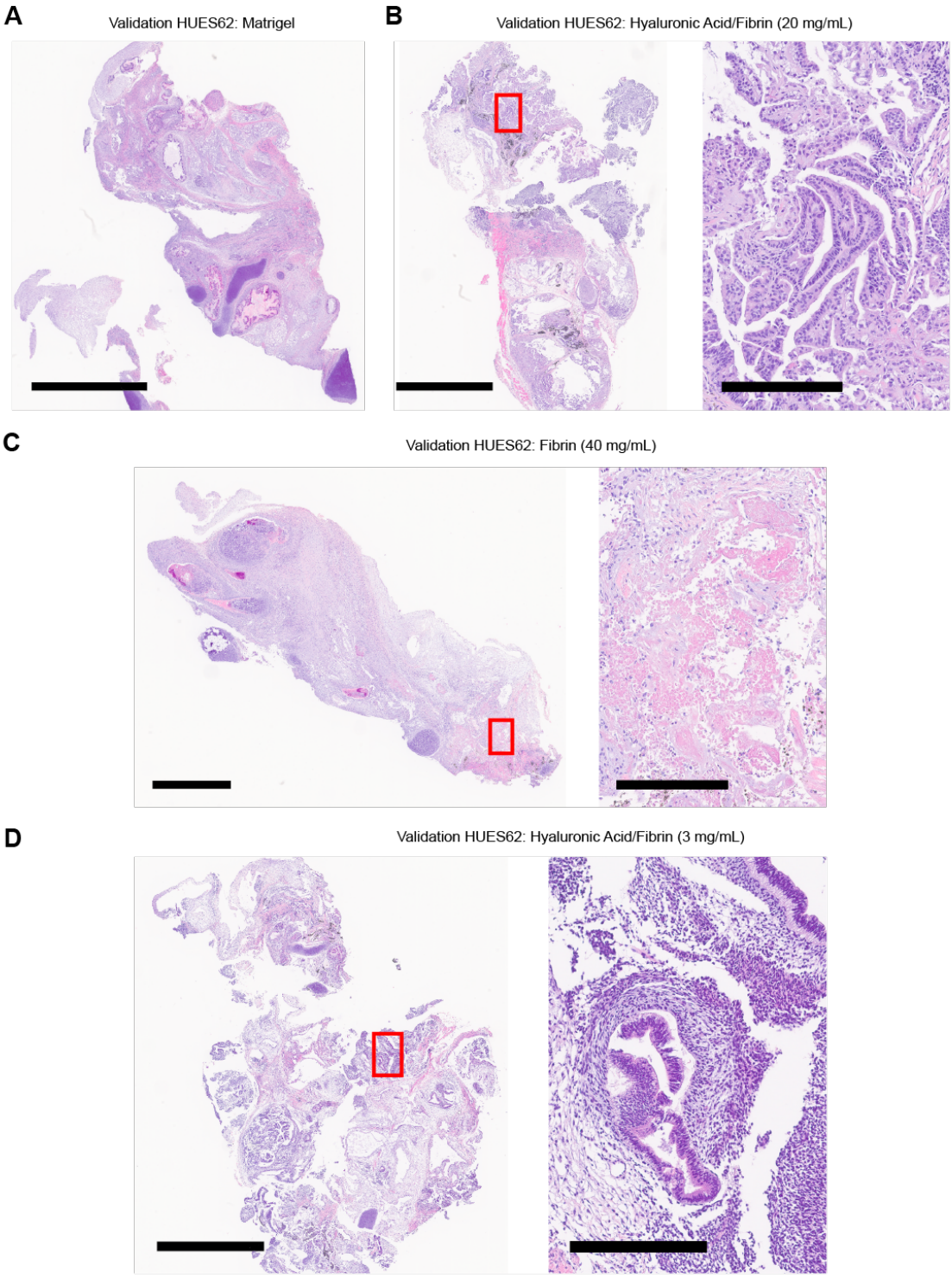

Figure 4.10: Hematoxylin and Eosin Staining of HUES62-ESC Validation Teratomas. (A) Teratoma grown in Matrigel. Scale bar: 2 mm **(B)** Teratoma grown in a blend of Hyaluronic Acid and Fibrin (20 mg/mL) with zoomed images of regions containing a high level of neural tissue. **(C)** Teratoma grown in Fibrin (40 mg/mL) with zoomed images of regions containing a high level of muscle tissue. **(D)** Teratoma grown in a blend of Hyaluronic Acid and Fibrin (3 mg/mL) with zoomed images of regions containing a high level of neural tissue. Scale bars: 2 mm (left) and 300 µm (right) for all except Matrigel.

4.5 Conclusion

Overall, we have clearly demonstrated the potential of tuning the native teratoma environment, with several key materials showing the capacity to bias differentiation towards muscular or neural lineages. While teratoma heterogeneity still remained, it is important to consider that the physical microenvironment is only a single parameter that could potentially impact teratoma development. Previous chapters focused on combining technologies from the separate fields of tissue and genetic engineering, and here, a similar principle can be applied. For instance, by tuning the material environment alongside delivery of micro-RNA responsive constructs that have previously demonstrated similar lineage-biasing capacities[208], there is the potential to further shift cell type heterogeneity in favor of specific cell types. As such, we believe the teratoma is a promising platform for resolving many of the issues present in organotypic tissue engineering.

4.6 Acknowledgements

Chapter 4, in part, is currently being prepared for submission for publication of the material. I, as the dissertation author, am one of three primary authors of this work, with the full authors list being: Michael Hu, Daniella McDonald, and Prashant Mali.

References

(1) Hayes, B.; Murphy, C.; Crawley, A.; O'Kennedy, R. Developments in Point-of-Care Diagnostic Technology for Cancer Detection. *Diagnostics* **2018**, *8* (2), 39. https://doi.org/10.3390/diagnostics8020039.

(2) Miller, K. D.; Nogueira, L.; Mariotto, A. B.; Rowland, J. H.; Yabroff, K. R.; Alfano, C. M.; Jemal, A.; Kramer, J. L.; Siegel, R. L. Cancer Treatment and Survivorship Statistics, 2019. *CA A Cancer J Clin* **2019**, *69* (5), 363–385. https://doi.org/10.3322/caac.21565.

(3) Islami, F.; Miller, K. D.; Siegel, R. L.; Zheng, Z.; Zhao, J.; Han, X.; Ma, J.; Jemal, A.; Yabroff, K. R. National and State Estimates of Lost Earnings From Cancer Deaths in the United States. *JAMA Oncol* **2019**, *5* (9), e191460. https://doi.org/10.1001/jamaoncol.2019.1460.

(4) Wong, C. H.; Siah, K. W.; Lo, A. W. Estimation of Clinical Trial Success Rates and Related Parameters. *Biostatistics* **2019**, *20* (2), 273–286. https://doi.org/10.1093/biostatistics/kxx069.

(5) Kleppe, M.; Levine, R. L. Tumor Heterogeneity Confounds and Illuminates: Assessing the Implications. *Nat Med* **2014**, *20* (4), 342–344. https://doi.org/10.1038/nm.3522.

(6) Alizadeh, A. A.; Aranda, V.; Bardelli, A.; Blanpain, C.; Bock, C.; Borowski, C.; Caldas, C.; Califano, A.; Doherty, M.; Elsner, M.; Esteller, M.; Fitzgerald, R.; Korbel, J. O.; Lichter, P.; Mason, C. E.; Navin, N.; Pe'er, D.; Polyak, K.; Roberts, C. W. M.; Siu, L.; Snyder, A.; Stower, H.; Swanton, C.; Verhaak, R. G. W.; Zenklusen, J. C.; Zuber, J.; Zucman-Rossi, J. Toward Understanding and Exploiting Tumor Heterogeneity. *Nat Med* **2015**, *21* (8), 846–853. https://doi.org/10.1038/nm.3915.

(7) Dagogo-Jack, I.; Shaw, A. T. Tumour Heterogeneity and Resistance to Cancer Therapies. *Nat Rev Clin Oncol* **2018**, *15* (2), 81–94. https://doi.org/10.1038/nrclinonc.2017.166.

(8) La Thangue, N. B.; Kerr, D. J. Predictive Biomarkers: A Paradigm Shift towards Personalized Cancer Medicine. *Nature Reviews Clinical Oncology* **2011**, *8*, 587–596.

(9) Ashley, E. A. Towards Precision Medicine. *Nat Rev Genet* **2016**, *17* (9), 507–522. https://doi.org/10.1038/nrg.2016.86.

(10) Tannock, I. F.; Hickman, J. A. Limits to Personalized Cancer Medicine. *N Engl J Med* **2016**, *375* (13), 1289–1294. https://doi.org/10.1056/NEJMsb1607705.

(11) Presley, C. J.; Tang, D.; Soulos, P. R.; Chiang, A. C.; Longtine, J. A.; Adelson, K. B.; Herbst, R. S.; Zhu, W.; Nussbaum, N. C.; Sorg, R. A.; Agarwala, V.; Abernethy, A. P.; Gross, C. P. Association of Broad-Based Genomic Sequencing With Survival Among Patients With Advanced Non–Small Cell Lung Cancer in the Community Oncology Setting. *JAMA* **2018**, *320* (5), 469. https://doi.org/10.1001/jama.2018.9824.

(12) Massard, C.; Michiels, S.; Ferté, C.; Le Deley, M.-C.; Lacroix, L.; Hollebecque, A.; Verlingue, L.; Ileana, E.; Rosellini, S.; Ammari, S.; Ngo-Camus, M.; Bahleda, R.; Gazzah, A.; Varga, A.; Postel-Vinay, S.; Loriot, Y.; Even, C.; Breuskin, I.; Auger, N.; Job, B.; De Baere, T.; Deschamps, F.; Vielh, P.; Scoazec, J.-Y.; Lazar, V.; Richon, C.; Ribrag, V.; Deutsch, E.; Angevin, E.; Vassal, G.; Eggermont, A.; André, F.; Soria, J.-C. High-Throughput Genomics and Clinical Outcome in Hard-to-Treat Advanced Cancers: Results of the MOSCATO 01 Trial. *Cancer Discov* **2017**, *7* (6), 586–595. https://doi.org/10.1158/2159-8290.CD-16-1396.

(13) Le Tourneau, C.; Delord, J.-P.; Gonçalves, A.; Gavoille, C.; Dubot, C.; Isambert, N.; Campone, M.; Trédan, O.; Massiani, M.-A.; Mauborgne, C.; Armanet, S.; Servant, N.; Bièche, I.; Bernard, V.; Gentien, D.; Jezequel, P.; Attignon, V.; Boyault, S.; Vincent-Salomon, A.; Servois, V.; Sablin, M.-P.; Kamal, M.; Paoletti, X. Molecularly Targeted Therapy Based on Tumour Molecular Profiling versus Conventional Therapy for Advanced Cancer (SHIVA): A Multicentre, Open-Label, Proof-of-Concept, Randomised, Controlled Phase 2 Trial. *The Lancet Oncology* **2015**, *16* (13), 1324–1334. https://doi.org/10.1016/S1470-2045(15)00188-6.

(14) Le Tourneau, C.; Borcoman, E.; Kamal, M. Molecular Profiling in Precision Medicine Oncology. *Nat Med* **2019**, *25* (5), 711–712. https://doi.org/10.1038/s41591-019-0442-2.

(15) Prasad, V. Perspective: The Precision-Oncology Illusion. *Nature* **2016**, *537* (7619), S63–S63. https://doi.org/10.1038/537S63a.

(16) Voest, E. E.; Bernards, R. DNA-Guided Precision Medicine for Cancer: A Case of Irrational Exuberance? *Cancer Discov* **2016**, *6* (2), 130–132. https://doi.org/10.1158/2159-8290.CD-15-1321.

(17) Friedman, A. A.; Letai, A.; Fisher, D. E.; Flaherty, K. T. Precision Medicine for Cancer with Next-Generation Functional Diagnostics. *Nat Rev Cancer* **2015**, *15* (12), 747–756. https://doi.org/10.1038/nrc4015.

(18) Devarasetty, M.; Mazzocchi, A. R.; Skardal, A. Applications of Bioengineered 3D Tissue and Tumor Organoids in Drug Development and Precision Medicine: Current and Future. *BioDrugs* **2018**, *32* (1), 53–68. https://doi.org/10.1007/s40259-017-0258-x.

(19) Lo, Y.-H.; Karlsson, K.; Kuo, C. J. Applications of Organoids for Cancer Biology and Precision Medicine. *Nat Cancer* **2020**, *1* (8), 761–773. https://doi.org/10.1038/s43018-020-0102-y.

(20) Morgens, D. W.; Deans, R. M.; Li, A.; Bassik, M. C. Systematic Comparison of CRISPR/Cas9 and RNAi Screens for Essential Genes. *Nat Biotechnol* **2016**, *34* (6), 634–636. https://doi.org/10.1038/nbt.3567.

(21) Schuster, A.; Erasimus, H.; Fritah, S.; Nazarov, P.; van Dyck, E.; Niclou, S.; Golebiewska, A. RNAi/CRISPR Screens: From a Pool to a Valid Hit. *Trends in Biotechnology* **2019**, *37* (1), 38–55.

(22) Shalem, O.; Sanjana, N. E.; Zhang, F. High-Throughput Functional Genomics Using CRISPR–Cas9. *Nat Rev Genet* **2015**, *16* (5), 299–311. https://doi.org/10.1038/nrg3899.

(23) Replogle, J. M.; Norman, T. M.; Xu, A.; Hussmann, J. A.; Chen, J.; Cogan, J. Z.; Meer, E. J.; Terry, J. M.; Riordan, D. P.; Srinivas, N.; Fiddes, I. T.; Arthur, J. G.; Alvarado, L. J.; Pfeiffer, K. A.; Mikkelsen, T. S.; Weissman, J. S.; Adamson, B. Combinatorial Single-Cell CRISPR Screens by Direct Guide RNA Capture and Targeted Sequencing. *Nat Biotechnol* **2020**. https://doi.org/10.1038/s41587-020-0470-y.

(24) Wong, A. S. L.; Choi, G. C. G.; Cui, C. H.; Pregernig, G.; Milani, P.; Adam, M.; Perli, S. D.; Kazer, S. W.; Gaillard, A.; Hermann, M.; Shalek, A. K.; Fraenkel, E.; Lu, T. K. Multiplexed Barcoded CRISPR-Cas9 Screening Enabled by CombiGEM. *Proc Natl Acad Sci USA* **2016**, *113* (9), 2544–2549. https://doi.org/10.1073/pnas.1517883113.

(25) Joung, J.; Konermann, S.; Gootenberg, J. S.; Abudayyeh, O. O.; Platt, R. J.; Brigham, M. D.; Sanjana, N. E.; Zhang, F. Genome-Scale CRISPR-Cas9 Knockout and Transcriptional Activation Screening. *Nat Protoc* **2017**, *12* (4), 828–863. https://doi.org/10.1038/nprot.2017.016.

(26) Adamson, B.; Norman, T. M.; Jost, M.; Cho, M. Y.; Nuñez, J. K.; Chen, Y.; Villalta, J. E.; Gilbert, L. A.; Horlbeck, M. A.; Hein, M. Y.; Pak, R. A.; Gray, A. N.; Gross, C. A.; Dixit, A.; Parnas, O.; Regev, A.; Weissman, J. S. A Multiplexed Single-Cell CRISPR Screening Platform Enables Systematic Dissection of the Unfolded Protein Response. *Cell* **2016**, *167* (7), 1867-1882.e21. https://doi.org/10.1016/j.cell.2016.11.048.

(27) Shen, J. P.; Zhao, D.; Sasik, R.; Luebeck, J.; Birmingham, A.; Bojorquez-Gomez, A.; Licon, K.; Klepper, K.; Pekin, D.; Beckett, A. N.; Sanchez, K. S.; Thomas, A.; Kuo, C.-C.; Du, D.; Roguev, A.; Lewis, N. E.; Chang, A. N.; Kreisberg, J. F.; Krogan, N.; Qi, L.; Ideker, T.; Mali, P. Combinatorial CRISPR–Cas9 Screens for

de Novo Mapping of Genetic Interactions. *Nat Methods* **2017**, *14* (6), 573–576. https://doi.org/10.1038/nmeth.4225.

(28) Mengwasser, K. E.; Adeyemi, R. O.; Leng, Y.; Choi, M. Y.; Clairmont, C.; D'Andrea, A. D.; Elledge, S. J. Genetic Screens Reveal FEN1 and APEX2 as BRCA2 Synthetic Lethal Targets. *Molecular Cell* **2019**, *73* (5), 885-899.e6. https://doi.org/10.1016/j.molcel.2018.12.008.

(29) Ringel, T.; Frey, N.; Ringnalda, F.; Janjuha, S.; Cherkaoui, S.; Butz, S.; Srivatsa, S.; Pirkl, M.; Russo, G.; Villiger, L.; Rogler, G.; Clevers, H.; Beerenwinkel, N.; Zamboni, N.; Baubec, T.; Schwank, G. Genome-Scale CRISPR Screening in Human Intestinal Organoids Identifies Drivers of TGF-β Resistance. *Cell Stem Cell* **2020**, *26* (3), 431-440.e8. https://doi.org/10.1016/j.stem.2020.02.007.

(30) Murakami, K.; Terakado, Y.; Saito, K.; Jomen, Y.; Takeda, H.; Oshima, M.; Barker, N. A Genome-Scale CRISPR Screen Reveals Factors Regulating Wnt-Dependent Renewal of Mouse Gastric Epithelial Cells. *Proc Natl Acad Sci USA* **2021**, *118* (4), e2016806118. https://doi.org/10.1073/pnas.2016806118.

(31) Mali, P.; Yang, L.; Esvelt, K. M.; Aach, J.; Guell, M.; DiCarlo, J. E.; Norville, J. E.; Church, G. M. RNA-Guided Human Genome Engineering via Cas9. *Science* **2013**, *339* (6121), 823–826. https://doi.org/10.1126/science.1232033.

(32) Cong, L.; Ran, F. A.; Cox, D.; Lin, S.; Barretto, R.; Habib, N.; Hsu, P. D.; Wu, X.; Jiang, W.; Marraffini, L. A.; Zhang, F. Multiplex Genome Engineering Using CRISPR/Cas Systems. *Science* **2013**, *339* (6121), 819–823. https://doi.org/10.1126/science.1231143.

(33) Cho, S. W.; Kim, S.; Kim, J. M.; Kim, J.-S. Targeted Genome Engineering in Human Cells with the Cas9 RNA-Guided Endonuclease. *Nat Biotechnol* **2013**, *31* (3), 230–232. https://doi.org/10.1038/nbt.2507.

(34) Luo, J. CRISPR/Cas9: From Genome Engineering to Cancer Drug Discovery. *Trends in Cancer* **2016**, *2* (6), 313–324. https://doi.org/10.1016/j.trecan.2016.05.001.

(35) Behan, F. M.; Iorio, F.; Picco, G.; Gonçalves, E.; Beaver, C. M.; Migliardi, G.; Santos, R.; Rao, Y.; Sassi, F.; Pinnelli, M.; Ansari, R.; Harper, S.; Jackson, D. A.; McRae, R.; Pooley, R.; Wilkinson, P.; van der Meer, D.; Dow, D.; Buser-Doepner, C.; Bertotti, A.; Trusolino, L.; Stronach, E. A.; Saez-Rodriguez, J.; Yusa, K.; Garnett, M. J. Prioritization of Cancer Therapeutic Targets Using CRISPR–Cas9 Screens. *Nature* **2019**, *568* (7753), 511–516. https://doi.org/10.1038/s41586-019-1103-9.

(36) Meyers, R. M.; Bryan, J. G.; McFarland, J. M.; Weir, B. A.; Sizemore, A. E.; Xu, H.; Dharia, N. V.; Montgomery, P. G.; Cowley, G. S.; Pantel, S.; Goodale, A.; Lee, Y.; Ali, L. D.; Jiang, G.; Lubonja, R.; Harrington, W. F.; Strickland, M.; Wu, T.; Hawes, D. C.; Zhivich, V. A.; Wyatt, M. R.; Kalani, Z.; Chang, J. J.; Okamoto, M.; Stegmaier, K.; Golub, T. R.; Boehm, J. S.; Vazquez, F.; Root, D. E.; Hahn, W. C.; Tsherniak, A. Computational Correction of Copy Number Effect Improves Specificity of CRISPR–Cas9 Essentiality Screens in Cancer Cells. *Nat Genet* **2017**, *49* (12), 1779–1784. https://doi.org/10.1038/ng.3984.

(37) Chen, S.; Sanjana, N. E.; Zheng, K.; Shalem, O.; Lee, K.; Shi, X.; Scott, D. A.; Song, J.; Pan, J. Q.; Weissleder, R.; Lee, H.; Zhang, F.; Sharp, P. A. Genome-Wide CRISPR Screen in a Mouse Model of Tumor Growth and Metastasis. *Cell* **2015**, *160* (6), 1246–1260. https://doi.org/10.1016/j.cell.2015.02.038.

(38) Manguso, R. T.; Pope, H. W.; Zimmer, M. D.; Brown, F. D.; Yates, K. B.; Miller, B. C.; Collins, N. B.; Bi, K.; LaFleur, M. W.; Juneja, V. R.; Weiss, S. A.; Lo, J.; Fisher, D. E.; Miao, D.; Van Allen, E.; Root, D. E.; Sharpe, A. H.; Doench, J. G.; Haining, W. N. In Vivo CRISPR Screening Identifies Ptpn2 as a Cancer Immunotherapy Target. *Nature* **2017**, *547* (7664), 413–418. https://doi.org/10.1038/nature23270.

(39) Chow, R. D.; Chen, S. Cancer CRISPR Screens In Vivo. *Trends in Cancer* **2018**, *4* (5), 349–358. https://doi.org/10.1016/j.trecan.2018.03.002.

(40) Doench, J. G. Am I Ready for CRISPR? A User's Guide to Genetic Screens. *Nat Rev Genet* **2018**, *19* (2), 67–80. https://doi.org/10.1038/nrg.2017.97.

(41) Kunz-Schughart, L. A.; Freyer, J. P.; Hofstaedter, F.; Ebner, R. The Use of 3-D Cultures for High-Throughput Screening: The Multicellular Spheroid Model. *J Biomol Screen* **2004**, *9* (4), 273–285. https://doi.org/10.1177/1087057104265040.

(42) Bracken, M. B. Why Animal Studies Are Often Poor Predictors of Human Reactions to Exposure. *J R Soc Med* **2009**, *102* (3), 120–122. https://doi.org/10.1258/jrsm.2008.08k033.

(43) Mak, I. W.; Evaniew, N.; Ghert, M. Lost in Translation: Animal Models and Clinical Trials in Cancer Treatment. 5.

(44) Praharaj, P. P.; Bhutia, S. K.; Nagrath, S.; Bitting, R. L.; Deep, G. Circulating Tumor Cell-Derived Organoids: Current Challenges and Promises in Medical Research and Precision Medicine. *Biochimica et Biophysica Acta (BBA) - Reviews on Cancer* **2018**, *1869* (2), 117–127. https://doi.org/10.1016/j.bbcan.2017.12.005.

(45) Dobrolecki, L. E.; Airhart, S. D.; Alferez, D. G.; Aparicio, S.; Behbod, F.; Bentires-Alj, M.; Brisken, C.; Bult, C. J.; Cai, S.; Clarke, R. B.; Dowst, H.; Ellis, M. J.; Gonzalez-Suarez, E.; Iggo, R. D.; Kabos, P.; Li, S.; Lindeman, G. J.; Marangoni, E.; McCoy, A.; Meric-Bernstam, F.; Piwnica-Worms, H.; Poupon, M.-F.; Reis-Filho, J.; Sartorius, C. A.; Scabia, V.; Sflomos, G.; Tu, Y.; Vaillant, F.; Visvader, J. E.; Welm, A.; Wicha, M. S.; Lewis, M. T. Patient-Derived Xenograft (PDX) Models in Basic and Translational Breast Cancer Research. *Cancer Metastasis Rev* **2016**, *35* (4), 547–573. https://doi.org/10.1007/s10555-016-9653-x.

(46) Han, K.; Pierce, S. E.; Li, A.; Spees, K.; Anderson, G. R.; Seoane, J. A.; Lo, Y.-H.; Dubreuil, M.; Olivas, M.; Kamber, R. A.; Wainberg, M.; Kostyrko, K.; Kelly, M. R.; Yousefi, M.; Simpkins, S. W.; Yao, D.; Lee, K.; Kuo, C. J.; Jackson, P. K.; Sweet-Cordero, A.; Kundaje, A.; Gentles, A. J.; Curtis, C.; Winslow, M. M.; Bassik, M. C. CRISPR Screens in Cancer Spheroids Identify 3D Growth-Specific Vulnerabilities. *Nature* **2020**, *580* (7801), 136–141. https://doi.org/10.1038/s41586-020-2099-x.

(47) Takahashi, N.; Cho, P.; Selfors, L. M.; Kuiken, H. J.; Kaul, R.; Fujiwara, T.; Harris, I. S.; Zhang, T.; Gygi, S. P.; Brugge, J. S. 3D Culture Models with CRISPR Screens Reveal Hyperactive NRF2 as a Prerequisite for Spheroid Formation via Regulation of Proliferation and Ferroptosis. *Molecular Cell* **2020**.

(48) Hoarau-Véchot, J.; Rafii, A.; Touboul, C.; Pasquier, J. Halfway between 2D and Animal Models: Are 3D Cultures the Ideal Tool to Study Cancer-Microenvironment Interactions? *IJMS* **2018**, *19* (1), 181. https://doi.org/10.3390/ijms19010181.

(49) Hutmacher, D. W. Biomaterials Offer Cancer Research the Third Dimension. *nature materials* **2010**, *9*, 4.

(50) Dutta, R. C.; Dutta, A. K. Cell-Interactive 3D-Scaffold; Advances and Applications. *Biotechnology Advances* **2009**, *27* (4), 334–339. https://doi.org/10.1016/j.biotechadv.2009.02.002.

(51) Ott, H. C.; Matthiesen, T. S.; Goh, S.-K.; Black, L. D.; Kren, S. M.; Netoff, T. I.; Taylor, D. A. Perfusion-Decellularized Matrix: Using Nature's Platform to Engineer a Bioartificial Heart. *Nat Med* **2008**, *14* (2), 213–221. https://doi.org/10.1038/nm1684.

(52) Lancaster, M. A.; Knoblich, J. A. Organogenesis in a Dish: Modeling Development and Disease Using Organoid Technologies. *Science* **2014**, *345* (6194), 1247125–1247125. https://doi.org/10.1126/science.1247125.

(53) Yui, S.; Nakamura, T.; Sato, T.; Nemoto, Y.; Mizutani, T.; Zheng, X.; Ichinose, S.; Nagaishi, T.; Okamoto, R.; Tsuchiya, K.; Clevers, H.; Watanabe, M. Functional

Engraftment of Colon Epithelium Expanded in Vitro from a Single Adult Lgr5+ Stem Cell. *Nat Med* **2012**, *18* (4), 618–623. https://doi.org/10.1038/nm.2695.

(54) Lawlor, K. T.; Vanslambrouck, J. M.; Higgins, J. W.; Chambon, A.; Bishard, K.; Arndt, D.; Er, P. X.; Wilson, S. B.; Howden, S. E.; Tan, K. S.; Li, F.; Hale, L. J.; Shepherd, B.; Pentoney, S.; Presnell, S. C.; Chen, A. E.; Little, M. H. Cellular Extrusion Bioprinting Improves Kidney Organoid Reproducibility and Conformation. *Nat. Mater.* **2021**, *20* (2), 260–271. https://doi.org/10.1038/s41563-020-00853-9.

(55) Ren, Y.; Yang, X.; Ma, Z.; Sun, X.; Zhang, Y.; Li, W.; Yang, H.; Qiang, L.; Yang, Z.; Liu, Y.; Deng, C.; Zhou, L.; Wang, T.; Lin, J.; Li, T.; Wu, T.; Wang, J. Developments and Opportunities for 3D Bioprinted Organoids. *Int J Bioprint* **2021**, *7* (3), 364. https://doi.org/10.18063/ijb.v7i3.364.

(56) Little, M. H.; Combes, A. N. Kidney Organoids: Accurate Models or Fortunate Accidents. *Genes and Development 33*, 1319–1345.

(57) Huch, M.; Dorrell, C.; Boj, S. F.; van Es, J. H.; Li, V. S. W.; van de Wetering, M.; Sato, T.; Hamer, K.; Sasaki, N.; Finegold, M. J.; Haft, A.; Vries, R. G.; Grompe, M.; Clevers, H. In Vitro Expansion of Single Lgr5+ Liver Stem Cells Induced by Wnt-Driven Regeneration. *Nature* **2013**, *494* (7436), 247–250. https://doi.org/10.1038/nature11826.

(58) Larsen, B. M.; Kannan, M.; Langer, L. F.; Leibowitz, B. D.; Bentaieb, A.; Cancino, A.; Dolgalev, I.; Drummond, B. E.; Dry, J. R.; Ho, C.-S.; Khullar, G.; Krantz, B. A.; Mapes, B.; McKinnon, K. E.; Metti, J.; Perera, J. F.; Rand, T. A.; Sanchez-Freire, V.; Shaxted, J. M.; Stein, M. M.; Streit, M. A.; Tan, Y.-H. C.; Zhang, Y.; Zhao, E.; Venkataraman, J.; Stumpe, M. C.; Borgia, J. A.; Masood, A.; Catenacci, D. V. T.; Mathews, J. V.; Gursel, D. B.; Wei, J.-J.; Welling, T. H.; Simeone, D. M.; White, K. P.; Khan, A. A.; Igartua, C.; Salahudeen, A. A. A Pan-Cancer Organoid Platform for Precision Medicine. *Cell Reports* **2021**, *36* (4), 109429. https://doi.org/10.1016/j.celrep.2021.109429.

(59) Tuveson, D.; Clevers, H. Cancer Modeling Meets Human Organoid Technology. *Science* **2019**, *364* (6444), 952–955. https://doi.org/10.1126/science.aaw6985.

(60) Boj, S. F.; Hwang, C.-I.; Baker, L. A.; Chio, I. I. C.; Engle, D. D.; Corbo, V.; Jager, M.; Ponz-Sarvise, M.; Tiriac, H.; Spector, M. S.; Gracanin, A.; Oni, T.; Yu, K. H.; van Boxtel, R.; Huch, M.; Rivera, K. D.; Wilson, J. P.; Feigin, M. E.; Öhlund, D.; Handly-Santana, A.; Ardito-Abraham, C. M.; Ludwig, M.; Elyada, E.; Alagesan, B.; Biffi, G.; Yordanov, G. N.; Delcuze, B.; Creighton, B.; Wright, K.; Park, Y.; Morsink, F. H. M.; Molenaar, I. Q.; Borel Rinkes, I. H.; Cuppen, E.; Hao, Y.; Jin, Y.; Nijman, I. J.; Iacobuzio-Donahue, C.; Leach, S. D.; Pappin, D. J.; Hammell, M.; Klimstra, D. S.; Basturk, O.; Hruban, R. H.; Offerhaus, G. J.; Vries, R. G. J.;

Clevers, H.; Tuveson, D. A. Organoid Models of Human and Mouse Ductal Pancreatic Cancer. *Cell* **2015**, *160* (1–2), 324–338. https://doi.org/10.1016/j.cell.2014.12.021.

(61) Broutier, L.; Mastrogiovanni, G.; Verstegen, M. M.; Francies, H. E.; Gavarró, L. M.; Bradshaw, C. R.; Allen, G. E.; Arnes-Benito, R.; Sidorova, O.; Gaspersz, M. P.; Georgakopoulos, N.; Koo, B.-K.; Dietmann, S.; Davies, S. E.; Praseedom, R. K.; Lieshout, R.; IJzermans, J. N. M.; Wigmore, S. J.; Saeb-Parsy, K.; Garnett, M. J.; van der Laan, L. J.; Huch, M. Human Primary Liver Cancer–Derived Organoid Cultures for Disease Modeling and Drug Screening. *Nat Med* **2017**, *23* (12), 1424–1435. https://doi.org/10.1038/nm.4438.

(62) van de Wetering, M.; Francies, H. E.; Francis, J. M.; Bounova, G.; Iorio, F.; Pronk, A.; van Houdt, W.; van Gorp, J.; Taylor-Weiner, A.; Kester, L.; McLaren-Douglas, A.; Blokker, J.; Jaksani, S.; Bartfeld, S.; Volckman, R.; van Sluis, P.; Li, V. S. W.; Seepo, S.; Sekhar Pedamallu, C.; Cibulskis, K.; Carter, S. L.; McKenna, A.; Lawrence, M. S.; Lichtenstein, L.; Stewart, C.; Koster, J.; Versteeg, R.; van Oudenaarden, A.; Saez-Rodriguez, J.; Vries, R. G. J.; Getz, G.; Wessels, L.; Stratton, M. R.; McDermott, U.; Meyerson, M.; Garnett, M. J.; Clevers, H. Prospective Derivation of a Living Organoid Biobank of Colorectal Cancer Patients. *Cell* **2015**, *161* (4), 933–945. https://doi.org/10.1016/j.cell.2015.03.053.

(63) Skardal, A.; Shupe, T.; Atala, A. Organoid-on-a-Chip and Body-on-a-Chip Systems for Drug Screening and Disease Modeling. *Drug Discovery Today* **2016**, *21* (9), 1399–1411. https://doi.org/10.1016/j.drudis.2016.07.003.

(64) Zhang, B.; Korolj, A.; Lai, B. F. L.; Radisic, M. Advances in Organ-on-a-Chip Engineering. *Nat Rev Mater* **2018**, *3* (8), 257–278. https://doi.org/10.1038/s41578-018-0034-7.

(65) Thakare, K.; Jerpseth, L.; Pei, Z.; Elwany, A.; Quek, F.; Qin, H. Bioprinting of Organ-on-Chip Systems: A Literature Review from a Manufacturing Perspective. *JMMP* **2021**, *5* (3), 91. https://doi.org/10.3390/jmmp5030091.

(66) Caballero, D.; Kaushik, S.; Correlo, V. M.; Oliveira, J. M.; Reis, R. L.; Kundu, S. C. Organ-on-Chip Models of Cancer Metastasis for Future Personalized Medicine: From Chip to the Patient. *Biomaterials* **2017**, *149*, 98–115. https://doi.org/10.1016/j.biomaterials.2017.10.005.

(67) Nguyen, M.; De Ninno, A.; Mencattini, A.; Mermet-Meillon, F.; Fornabaio, G.; Evans, S. S.; Cossutta, M.; Khira, Y.; Han, W.; Sirven, P.; Pelon, F.; Di Giuseppe, D.; Bertani, F. R.; Gerardino, A.; Yamada, A.; Descroix, S.; Soumelis, V.; Mechta-Grigoriou, F.; Zalcman, G.; Camonis, J.; Martinelli, E.; Businaro, L.; Parrini, M. C. Dissecting Effects of Anti-Cancer Drugs and Cancer-Associated

Fibroblasts by On-Chip Reconstitution of Immunocompetent Tumor Microenvironments. *Cell Reports* **2018**, *25* (13), 3884-3893.e3. https://doi.org/10.1016/j.celrep.2018.12.015.

(68) Murphy, S. V.; Atala, A. 3D Bioprinting of Tissues and Organs. *Nat Biotechnol* **2014**, *32* (8), 773–785. https://doi.org/10.1038/nbt.2958.

(69) Gu, B. K.; Choi, D. J.; Park, S. J.; Kim, M. S.; Kang, C. M.; Kim, C.-H. 3-Dimensional Bioprinting for Tissue Engineering Applications. *Biomater Res* **2016**, *20* (1), 12. https://doi.org/10.1186/s40824-016-0058-2.

(70) Zhu, W.; Qu, X.; Zhu, J.; Ma, X.; Patel, S.; Liu, J.; Wang, P.; Lai, C. S. E.; Gou, M.; Xu, Y.; Zhang, K.; Chen, S. Direct 3D Bioprinting of Prevascularized Tissue Constructs with Complex Microarchitecture. *Biomaterials* **2017**, *124*, 106–115. https://doi.org/10.1016/j.biomaterials.2017.01.042.

(71) Kolesky, D. B.; Homan, K. A.; Skylar-Scott, M. A.; Lewis, J. A. Three-Dimensional Bioprinting of Thick Vascularized Tissues. *Proc Natl Acad Sci USA* **2016**, *113* (12), 3179–3184. https://doi.org/10.1073/pnas.1521342113.

(72) Lee, V. K.; Kim, D. Y.; Ngo, H.; Lee, Y.; Seo, L.; Yoo, S.-S.; Vincent, P. A.; Dai, G. Creating Perfused Functional Vascular Channels Using 3D Bio-Printing Technology. *Biomaterials* **2014**, *35* (28), 8092–8102. https://doi.org/10.1016/j.biomaterials.2014.05.083.

(73) Miller, J. S.; Stevens, K. R.; Yang, M. T.; Baker, B. M.; Nguyen, D.-H. T.; Cohen, D. M.; Toro, E.; Chen, A. A.; Galie, P. A.; Yu, X.; Chaturvedi, R.; Bhatia, S. N.; Chen, C. S. Rapid Casting of Patterned Vascular Networks for Perfusable Engineered Three-Dimensional Tissues. *Nature Mater* **2012**, *11* (9), 768–774. https://doi.org/10.1038/nmat3357.

(74) Jain, R. K.; Au, P.; Tam, J.; Duda, D. G.; Fukumura, D. Engineering Vascularized Tissue. *Nat Biotechnol* **2005**, *23* (7), 821–823. https://doi.org/10.1038/nbt0705-821.

(75) Mandrycky, C.; Wang, Z.; Kim, K.; Kim, D.-H. 3D Bioprinting for Engineering Complex Tissues. *Biotechnology Advances* **2016**, *34* (4), 422–434. https://doi.org/10.1016/j.biotechadv.2015.12.011.

(76) Elson, E. L.; Genin, G. M. Tissue Constructs: Platforms for Basic Research and Drug Discovery. *Interface Focus.* **2016**, *6* (1), 20150095. https://doi.org/10.1098/rsfs.2015.0095.

(77) Benam, K. H.; Dauth, S.; Hassell, B.; Herland, A.; Jain, A.; Jang, K.-J.; Karalis, K.; Kim, H. J.; MacQueen, L.; Mahmoodian, R.; Musah, S.; Torisawa, Y.; van der

Meer, A. D.; Villenave, R.; Yadid, M.; Parker, K. K.; Ingber, D. E. Engineered In Vitro Disease Models. *Annu. Rev. Pathol. Mech. Dis.* **2015**, *10* (1), 195–262. https://doi.org/10.1146/annurev-pathol-012414-040418.

(78) Elliott, N. T.; Yuan, F. A Review of Three-Dimensional In Vitro Tissue Models for Drug Discovery and Transport Studies. *Journal of Pharmaceutical Sciences* **2011**, *100* (1), 59–74. https://doi.org/10.1002/jps.22257.

(79) Kimlin, L.; Kassis, J.; Virador, V. 3D in Vitro Tissue Models and Their Potential for Drug Screening. *Expert Opinion on Drug Discovery* **2013**, *8* (12), 1455–1466. https://doi.org/10.1517/17460441.2013.852181.

(80) Folkman, J. Angiogenesis in Cancer, Vascular, Rheumatoid and Other Disease. *Nature Medicine* **1995**, *1* (1), 27–31.

(81) Wang, Z.; Abdulla, R.; Parker, B.; Samanipour, R.; Ghosh, S.; Kim, K. A Simple and High-Resolution Stereolithography-Based 3D Bioprinting System Using Visible Light Crosslinkable Bioinks. *Biofabrication* **2015**, *7* (4), 045009. https://doi.org/10.1088/1758-5090/7/4/045009.

(82) Kang, H.-W.; Lee, S. J.; Ko, I. K.; Kengla, C.; Yoo, J. J.; Atala, A. A 3D Bioprinting System to Produce Human-Scale Tissue Constructs with Structural Integrity. *Nat Biotechnol* **2016**, *34* (3), 312–319. https://doi.org/10.1038/nbt.3413.

(83) Pedde, R. D.; Mirani, B.; Navaei, A.; Styan, T.; Wong, S.; Mehrali, M.; Thakur, A.; Mohtaram, N. K.; Bayati, A.; Dolatshahi-Pirouz, A.; Nikkhah, M.; Willerth, S. M.; Akbari, M. Emerging Biofabrication Strategies for Engineering Complex Tissue Constructs. *Adv. Mater.* **2017**, *29* (19), 1606061. https://doi.org/10.1002/adma.201606061.

(84) Hinton, T. J.; Jallerat, Q.; Palchesko, R. N.; Park, J. H.; Grodzicki, M. S.; Shue, H.-J.; Ramadan, M. H.; Hudson, A. R.; Feinberg, A. W. Three-Dimensional Printing of Complex Biological Structures by Freeform Reversible Embedding of Suspended Hydrogels. *Sci. Adv.* **2015**, *1* (9), e1500758. https://doi.org/10.1126/sciadv.1500758.

(85) Park, J.; Lee, S. J.; Chung, S.; Lee, J. H.; Kim, W. D.; Lee, J. Y.; Park, S. A. Cell-Laden 3D Bioprinting Hydrogel Matrix Depending on Different Compositions for Soft Tissue Engineering: Characterization and Evaluation. *Materials Science and Engineering: C* **2017**, *71*, 678–684. https://doi.org/10.1016/j.msec.2016.10.069.

(86) Zhang, K.; Fu, Q.; Yoo, J.; Chen, X.; Chandra, P.; Mo, X.; Song, L.; Atala, A.; Zhao, W. 3D Bioprinting of Urethra with PCL/PLCL Blend and Dual Autologous Cells in Fibrin Hydrogel: An in Vitro Evaluation of Biomimetic Mechanical

Property and Cell Growth Environment. *Acta Biomaterialia* **2017**, *50*, 154–164. https://doi.org/10.1016/j.actbio.2016.12.008.

(87) Jia, W.; Gungor-Ozkerim, P. S.; Zhang, Y. S.; Yue, K.; Zhu, K.; Liu, W.; Pi, Q.; Byambaa, B.; Dokmeci, M. R.; Shin, S. R.; Khademhosseini, A. Direct 3D Bioprinting of Perfusable Vascular Constructs Using a Blend Bioink. *Biomaterials* **2016**, *106*, 58–68. https://doi.org/10.1016/j.biomaterials.2016.07.038.

(88) Ouyang, L.; Highley, C. B.; Sun, W.; Burdick, J. A. A Generalizable Strategy for the 3D Bioprinting of Hydrogels from Nonviscous Photo-crosslinkable Inks. *Adv. Mater.* **2017**, *29* (8), 1604983. https://doi.org/10.1002/adma.201604983.

(89) Markstedt, K.; Mantas, A.; Tournier, I.; Martínez Ávila, H.; Hägg, D.; Gatenholm, P. 3D Bioprinting Human Chondrocytes with Nanocellulose–Alginate Bioink for Cartilage Tissue Engineering Applications. *Biomacromolecules* **2015**, *16* (5), 1489–1496. https://doi.org/10.1021/acs.biomac.5b00188.

(90) Pati, F.; Jang, J.; Ha, D.-H.; Won Kim, S.; Rhie, J.-W.; Shim, J.-H.; Kim, D.-H.; Cho, D.-W. Printing Three-Dimensional Tissue Analogues with Decellularized Extracellular Matrix Bioink. *Nat Commun* **2014**, *5* (1), 3935. https://doi.org/10.1038/ncomms4935.

(91) Bercea, M.; Darie, R. N.; Niţă, L. E.; Morariu, S. Temperature Responsive Gels Based on Pluronic F127 and Poly(Vinyl Alcohol). *Ind. Eng. Chem. Res.* **2011**, *50* (7), 4199–4206. https://doi.org/10.1021/ie1024408.

(92) Gilbert, J. C.; Washington, C.; Davies, M. C.; Hadgraft, J. The Behaviour of Pluronic F127 in Aqueous Solution Studied Using Fluorescent Probes. *International Journal of Pharmaceutics* **1987**, *40* (1–2), 93–99. https://doi.org/10.1016/0378-5173(87)90052-4.

(93) Orban, J. M.; Wilson, L. B.; Kofroth, J. A.; El-Kurdi, M. S.; Maul, T. M.; Vorp, D. A. Crosslinking of Collagen Gels by Transglutaminase. *J. Biomed. Mater. Res.* **2004**, *68A* (4), 756–762. https://doi.org/10.1002/jbm.a.20110.

(94) Yung, C. W.; Wu, L. Q.; Tullman, J. A.; Payne, G. F.; Bentley, W. E.; Barbari, T. A. Transglutaminase Crosslinked Gelatin as a Tissue Engineering Scaffold. *J. Biomed. Mater. Res.* **2007**, *83A* (4), 1039–1046. https://doi.org/10.1002/jbm.a.31431.

(95) Ranga, A.; Lutolf, M. P.; Hilborn, J.; Ossipov, D. A. Hyaluronic Acid Hydrogels Formed in Situ by Transglutaminase-Catalyzed Reaction. *Biomacromolecules* **2016**, *17* (5), 1553–1560. https://doi.org/10.1021/acs.biomac.5b01587.

(96) Li, P.-S.; -Liang Lee, I.; Yu, W.-L.; Sun, J.-S.; Jane, W.-N.; Shen, H.-H. A Novel Albumin-Based Tissue Scaffold for Autogenic Tissue Engineering Applications. *Sci Rep* **2015**, *4* (1), 5600. https://doi.org/10.1038/srep05600.

(97) Jose, R. R.; Rodriguez, M. J.; Dixon, T. A.; Omenetto, F.; Kaplan, D. L. Evolution of Bioinks and Additive Manufacturing Technologies for 3D Bioprinting. *ACS Biomater. Sci. Eng.* **2016**, *2* (10), 1662–1678. https://doi.org/10.1021/acsbiomaterials.6b00088.

(98) Li, S.; Liu, Y.-Y.; Liu, L.-J.; Hu, Q.-X. A Versatile Method for Fabricating Tissue Engineering Scaffolds with a Three-Dimensional Channel for Prevasculature Networks. *ACS Appl. Mater. Interfaces* **2016**, *8* (38), 25096–25103. https://doi.org/10.1021/acsami.6b07725.

(99) Pimentel C., R.; Ko, S. K.; Caviglia, C.; Wolff, A.; Emnéus, J.; Keller, S. S.; Dufva, M. Three-Dimensional Fabrication of Thick and Densely Populated Soft Constructs with Complex and Actively Perfused Channel Network. *Acta Biomaterialia* **2018**, *65*, 174–184. https://doi.org/10.1016/j.actbio.2017.10.047.

(100) Chia, H. N.; Wu, B. M. Recent Advances in 3D Printing of Biomaterials. *J Biol Eng* **2015**, *9* (1), 4. https://doi.org/10.1186/s13036-015-0001-4.

(101) Goyanes, A.; Buanz, A. B. M.; Basit, A. W.; Gaisford, S. Fused-Filament 3D Printing (3DP) for Fabrication of Tablets. *International Journal of Pharmaceutics* **2014**, *476* (1–2), 88–92. https://doi.org/10.1016/j.ijpharm.2014.09.044.

(102) Prasad, L. K.; Smyth, H. 3D Printing Technologies for Drug Delivery: A Review. *Drug Development and Industrial Pharmacy* **2016**, *42* (7), 1019–1031. https://doi.org/10.3109/03639045.2015.1120743.

(103) Levato, R.; Visser, J.; Planell, J. A.; Engel, E.; Malda, J.; Mateos-Timoneda, M. A. Biofabrication of Tissue Constructs by 3D Bioprinting of Cell-Laden Microcarriers. *Biofabrication* **2014**, *6* (3), 035020. https://doi.org/10.1088/1758-5082/6/3/035020.

(104) Sawkins, M. J.; Mistry, P.; Brown, B. N.; Shakesheff, K. M.; Bonassar, L. J.; Yang, J. Cell and Protein Compatible 3D Bioprinting of Mechanically Strong Constructs for Bone Repair. *Biofabrication* **2015**, *7* (3), 035004. https://doi.org/10.1088/1758-5090/7/3/035004.

(105) Fleming, J. M.; Miller, T. C.; Meyer, M. J.; Ginsburg, E.; Vonderhaar, B. K. Local Regulation of Human Breast Xenograft Models. *J. Cell. Physiol.* **2010**, *224* (3), 795–806. https://doi.org/10.1002/jcp.22190.

(106) Kocatürk, B.; Versteeg, H. H. Orthotopic Injection of Breast Cancer Cells into the Mammary Fat Pad of Mice to Study Tumor Growth. *JoVE* **2015**, No. 96, 51967. https://doi.org/10.3791/51967.

(107) Meng, Z.; Qiu, Y.; Lin, K. C.; Kumar, A.; Placone, J. K.; Fang, C.; Wang, K.-C.; Lu, S.; Pan, M.; Hong, A. W.; Moroishi, T.; Luo, M.; Plouffe, S. W.; Diao, Y.; Ye, Z.; Park, H. W.; Wang, X.; Yu, F.-X.; Chien, S.; Wang, C.-Y.; Ren, B.; Engler, A. J.; Guan, K.-L. RAP2 Mediates Mechanoresponses of the Hippo Pathway. *Nature* **2018**, *560* (7720), 655–660. https://doi.org/10.1038/s41586-018-0444-0.

(108) Qiu, Y.; Ahn, B.; Sakurai, Y.; Hansen, C. E.; Tran, R.; Mimche, P. N.; Mannino, R. G.; Ciciliano, J. C.; Lamb, T. J.; Joiner, C. H.; Ofori-Acquah, S. F.; Lam, W. A. Microvasculature-on-a-Chip for the Long-Term Study of Endothelial Barrier Dysfunction and Microvascular Obstruction in Disease. *Nat Biomed Eng* **2018**, *2* (6), 453–463. https://doi.org/10.1038/s41551-018-0224-z.

(109) Müller, A. M.; Hermanns, M. I.; Skrzynski, C.; Nesslinger, M.; Müller, K.-M.; Kirkpatrick, C. J. Expression of the Endothelial Markers PECAM-1, VWf, and CD34 in Vivo and in Vitro. *Experimental and Molecular Pathology* **2002**, *72* (3), 221–229. https://doi.org/10.1006/exmp.2002.2424.

(110) Maleki, M.; Ghanbarvand, F.; Behvarz, M. R.; Ejtemaei, M.; Ghadirkhomi, E. Comparison of Mesenchymal Stem Cell Markers in Multiple Human Adult Stem Cells. *Int J Stem Cells* **2014**, *7* (2), 118–126. https://doi.org/10.15283/ijsc.2014.7.2.118.

(111) Justice, B. A.; Badr, N. A.; Felder, R. A. 3D Cell Culture Opens New Dimensions in Cell-Based Assays. *Drug Discovery Today* **2009**, *14* (1–2), 102–107. https://doi.org/10.1016/j.drudis.2008.11.006.

(112) Tibbitt, M. W.; Anseth, K. S. Hydrogels as Extracellular Matrix Mimics for 3D Cell Culture. *Biotechnol. Bioeng.* **2009**, *103* (4), 655–663. https://doi.org/10.1002/bit.22361.

(113) Hughes, C. S.; Postovit, L. M.; Lajoie, G. A. Matrigel: A Complex Protein Mixture Required for Optimal Growth of Cell Culture. *Proteomics* **2010**, *10* (9), 1886–1890. https://doi.org/10.1002/pmic.200900758.

(114) Calderon, G. A.; Thai, P.; Hsu, C. W.; Grigoryan, B.; Gibson, S. M.; Dickinson, M. E.; Miller, J. S. Tubulogenesis of Co-Cultured Human IPS-Derived Endothelial Cells and Human Mesenchymal Stem Cells in Fibrin and Gelatin Methacrylate Gels. *Biomater. Sci.* **2017**, *5* (8), 1652–1660. https://doi.org/10.1039/C7BM00223H.

(115) Levato, R.; Jungst, T.; Scheuring, R. G.; Blunk, T.; Groll, J.; Malda, J. From Shape to Function: The Next Step in Bioprinting. *Adv. Mater.* **2020**, *32* (12), 1906423. https://doi.org/10.1002/adma.201906423.

(116) Dasgupta, Q.; Black, L. D. A FRESH SLATE for 3D Bioprinting. *Science* **2019**, *365* (6452), 446–447. https://doi.org/10.1126/science.aay0478.

(117) Drost, J.; Clevers, H. Organoids in Cancer Research. *Nat Rev Cancer* **2018**, *18* (7), 407–418. https://doi.org/10.1038/s41568-018-0007-6.

(118) Sontheimer-Phelps, A.; Hassell, B. A.; Ingber, D. E. Modelling Cancer in Microfluidic Human Organs-on-Chips. *Nat Rev Cancer* **2019**, *19* (2), 65–81. https://doi.org/10.1038/s41568-018-0104-6.

(119) Wolf, K. J.; Chen, J.; Coombes, J. D.; Aghi, M. K.; Kumar, S. Dissecting and Rebuilding the Glioblastoma Microenvironment with Engineered Materials. *Nat Rev Mater* **2019**, *4* (10), 651–668. https://doi.org/10.1038/s41578-019-0135-y.

(120) Song, H.-H. G.; Rumma, R. T.; Ozaki, C. K.; Edelman, E. R.; Chen, C. S. Vascular Tissue Engineering: Progress, Challenges, and Clinical Promise. *Cell Stem Cell* **2018**, *22* (3), 340–354. https://doi.org/10.1016/j.stem.2018.02.009.

(121) Prendergast, M. E.; Burdick, J. A. Recent Advances in Enabling Technologies in 3D Printing for Precision Medicine. *Adv. Mater.* **2020**, *32* (13), 1902516. https://doi.org/10.1002/adma.201902516.

(122) Langhans, S. A. Three-Dimensional in Vitro Cell Culture Models in Drug Discovery and Drug Repositioning. *Front. Pharmacol.* **2018**, *9*, 6. https://doi.org/10.3389/fphar.2018.00006.

(123) Ma, X.; Liu, J.; Zhu, W.; Tang, M.; Lawrence, N.; Yu, C.; Gou, M.; Chen, S. 3D Bioprinting of Functional Tissue Models for Personalized Drug Screening and in Vitro Disease Modeling. *Advanced Drug Delivery Reviews* **2018**, *132*, 235–251. https://doi.org/10.1016/j.addr.2018.06.011.

(124) Neal, J. T.; Li, X.; Zhu, J.; Giangarra, V.; Grzeskowiak, C. L.; Ju, J.; Liu, I. H.; Chiou, S.-H.; Salahudeen, A. A.; Smith, A. R.; Deutsch, B. C.; Liao, L.; Zemek, A. J.; Zhao, F.; Karlsson, K.; Schultz, L. M.; Metzner, T. J.; Nadauld, L. D.; Tseng, Y.-Y.; Alkhairy, S.; Oh, C.; Keskula, P.; Mendoza-Villanueva, D.; De La Vega, F. M.; Kunz, P. L.; Liao, J. C.; Leppert, J. T.; Sunwoo, J. B.; Sabatti, C.; Boehm, J. S.; Hahn, W. C.; Zheng, G. X. Y.; Davis, M. M.; Kuo, C. J. Organoid Modeling of the Tumor Immune Microenvironment. *Cell* **2018**, *175* (7), 1972-1988.e16. https://doi.org/10.1016/j.cell.2018.11.021.

(125) Li, X.; Nadauld, L.; Ootani, A.; Corney, D. C.; Pai, R. K.; Gevaert, O.; Cantrell, M. A.; Rack, P. G.; Neal, J. T.; Chan, C. W.-M.; Yeung, T.; Gong, X.; Yuan, J.; Wilhelmy, J.; Robine, S.; Attardi, L. D.; Plevritis, S. K.; Hung, K. E.; Chen, C.-Z.; Ji, H. P.; Kuo, C. J. Oncogenic Transformation of Diverse Gastrointestinal Tissues in Primary Organoid Culture. *Nat Med* **2014**, *20* (7), 769–777. https://doi.org/10.1038/nm.3585.

(126) Takebe, T.; Sekine, K.; Enomura, M.; Koike, H.; Kimura, M.; Ogaeri, T.; Zhang, R.-R.; Ueno, Y.; Zheng, Y.-W.; Koike, N.; Aoyama, S.; Adachi, Y.; Taniguchi, H. Vascularized and Functional Human Liver from an IPSC-Derived Organ Bud Transplant. *Nature* **2013**, *499* (7459), 481–484. https://doi.org/10.1038/nature12271.

(127) Kim, S.; Lee, H.; Chung, M.; Jeon, N. L. Engineering of Functional, Perfusable 3D Microvascular Networks on a Chip. *Lab Chip* **2013**, *13* (8), 1489. https://doi.org/10.1039/c3lc41320a.

(128) Hsu, Y.-H.; Moya, M. L.; Hughes, C. C. W.; George, S. C.; Lee, A. P. A Microfluidic Platform for Generating Large-Scale Nearly Identical Human Microphysiological Vascularized Tissue Arrays. *Lab Chip* **2013**, *13* (15), 2990. https://doi.org/10.1039/c3lc50424g.

(129) Choi, Y.; Hyun, E.; Seo, J.; Blundell, C.; Kim, H. C.; Lee, E.; Lee, S. H.; Moon, A.; Moon, W. K.; Huh, D. A Microengineered Pathophysiological Model of Early-Stage Breast Cancer. *Lab Chip* **2015**, *15* (16), 3350–3357. https://doi.org/10.1039/C5LC00514K.

(130) Hassell, B. A.; Goyal, G.; Lee, E.; Sontheimer-Phelps, A.; Levy, O.; Chen, C. S.; Ingber, D. E. Human Organ Chip Models Recapitulate Orthotopic Lung Cancer Growth, Therapeutic Responses, and Tumor Dormancy In Vitro. *Cell Reports* **2017**, *21* (2), 508–516. https://doi.org/10.1016/j.celrep.2017.09.043.

(131) Bersini, S.; Jeon, J. S.; Dubini, G.; Arrigoni, C.; Chung, S.; Charest, J. L.; Moretti, M.; Kamm, R. D. A Microfluidic 3D in Vitro Model for Specificity of Breast Cancer Metastasis to Bone. *Biomaterials* **2014**, *35* (8), 2454–2461. https://doi.org/10.1016/j.biomaterials.2013.11.050.

(132) Grigoryan, B.; Paulsen, S. J.; Corbett, D. C.; Sazer, D. W.; Fortin, C. L.; Zaita, A. J.; Greenfield, P. T.; Calafat, N. J.; Gounley, J. P.; Ta, A. H.; Johansson, F.; Randles, A.; Rosenkrantz, J. E.; Louis-Rosenberg, J. D.; Galie, P. A.; Stevens, K. R.; Miller, J. S. Multivascular Networks and Functional Intravascular Topologies within Biocompatible Hydrogels. *Science* **2019**, *364* (6439), 458–464. https://doi.org/10.1126/science.aav9750.

(133) Bhattacharjee, T.; Zehnder, S. M.; Rowe, K. G.; Jain, S.; Nixon, R. M.; Sawyer, W. G.; Angelini, T. E. Writing in the Granular Gel Medium. *Sci. Adv.* **2015**, *1* (8), e1500655. https://doi.org/10.1126/sciadv.1500655.

(134) Wang, Z.; Mithieux, S. M.; Weiss, A. S. Fabrication Techniques for Vascular and Vascularized Tissue Engineering. *Adv. Healthcare Mater.* **2019**, *8* (19), 1900742. https://doi.org/10.1002/adhm.201900742.

(135) Kinstlinger, I. S.; Saxton, S. H.; Calderon, G. A.; Ruiz, K. V.; Yalacki, D. R.; Deme, P. R.; Rosenkrantz, J. E.; Louis-Rosenberg, J. D.; Johansson, F.; Janson, K. D.; Sazer, D. W.; Panchavati, S. S.; Bissig, K.-D.; Stevens, K. R.; Miller, J. S. Generation of Model Tissues with Dendritic Vascular Networks via Sacrificial Laser-Sintered Carbohydrate Templates. *Nat Biomed Eng* **2020**. https://doi.org/10.1038/s41551-020-0566-1.

(136) Kim, W.; Lee, H.; Lee, J.; Atala, A.; Yoo, J. J.; Lee, S. J.; Kim, G. H. Efficient Myotube Formation in 3D Bioprinted Tissue Construct by Biochemical and Topographical Cues. *Biomaterials* **2020**, *230*, 119632. https://doi.org/10.1016/j.biomaterials.2019.119632.

(137) Nguyen, D.-H. T.; Stapleton, S. C.; Yang, M. T.; Cha, S. S.; Choi, C. K.; Galie, P. A.; Chen, C. S. Biomimetic Model to Reconstitute Angiogenic Sprouting Morphogenesis in Vitro. *Proceedings of the National Academy of Sciences* **2013**, *110* (17), 6712–6717. https://doi.org/10.1073/pnas.1221526110.

(138) Song, K. H.; Highley, C. B.; Rouff, A.; Burdick, J. A. Complex 3D-Printed Microchannels within Cell-Degradable Hydrogels. *Adv. Funct. Mater.* **2018**, *28* (31), 1801331. https://doi.org/10.1002/adfm.201801331.

(139) Lee, A.; Hudson, A. R.; Shiwarski, D. J.; Tashman, J. W.; Hinton, T. J.; Yerneni, S.; Bliley, J. M.; Campbell, P. G.; Feinberg, A. W. 3D Bioprinting of Collagen to Rebuild Components of the Human Heart. *Science* **2019**, *365* (6452), 482–487. https://doi.org/10.1126/science.aav9051.

(140) Skylar-Scott, M. A.; Uzel, S. G. M.; Nam, L. L.; Ahrens, J. H.; Truby, R. L.; Damaraju, S.; Lewis, J. A. Biomanufacturing of Organ-Specific Tissues with High Cellular Density and Embedded Vascular Channels. *Sci. Adv.* **2019**, *5* (9), eaaw2459. https://doi.org/10.1126/sciadv.aaw2459.

(141) Kampmann, M.; Bassik, M. C.; Weissman, J. S. Functional Genomics Platform for Pooled Screening and Generation of Mammalian Genetic Interaction Maps. *Nat Protoc* **2014**, *9* (8), 1825–1847. https://doi.org/10.1038/nprot.2014.103.

(142) Koike-Yusa, H.; Li, Y.; Tan, E.-P.; Velasco-Herrera, M. D. C.; Yusa, K. Genome-Wide Recessive Genetic Screening in Mammalian Cells with a Lentiviral

CRISPR-Guide RNA Library. *Nat Biotechnol* **2014**, *32* (3), 267–273. https://doi.org/10.1038/nbt.2800.

(143) Liberali, P.; Snijder, B.; Pelkmans, L. Single-Cell and Multivariate Approaches in Genetic Perturbation Screens. *Nat Rev Genet* **2015**, *16* (1), 18–32. https://doi.org/10.1038/nrg3768.

(144) Gilbert, L. A.; Horlbeck, M. A.; Adamson, B.; Villalta, J. E.; Chen, Y.; Whitehead, E. H.; Guimaraes, C.; Panning, B.; Ploegh, H. L.; Bassik, M. C.; Qi, L. S.; Kampmann, M.; Weissman, J. S. Genome-Scale CRISPR-Mediated Control of Gene Repression and Activation. *Cell* **2014**, *159* (3), 647–661. https://doi.org/10.1016/j.cell.2014.09.029.

(145) Sanjana, N. E.; Shalem, O.; Zhang, F. Improved Vectors and Genome-Wide Libraries for CRISPR Screening. *Nat Methods* **2014**, *11* (8), 783–784. https://doi.org/10.1038/nmeth.3047.

(146) Hu, M.; Dailamy, A.; Lei, X. Y.; Parekh, U.; McDonald, D.; Kumar, A.; Mali, P. Facile Engineering of Long-Term Culturable Ex Vivo Vascularized Tissues Using Biologically Derived Matrices. *Adv. Healthcare Mater.* **2018**, *7* (23), 1800845. https://doi.org/10.1002/adhm.201800845.

(147) Zhang, G.-L.; Zhang, Y.; Cao, K.-X.; Wang, X.-M. Orthotopic Injection of Breast Cancer Cells into the Mice Mammary Fat Pad. *JoVE* **2019**, No. 143, 58604. https://doi.org/10.3791/58604.

(148) Doench, J. G.; Fusi, N.; Sullender, M.; Hegde, M.; Vaimberg, E. W.; Donovan, K. F.; Smith, I.; Tothova, Z.; Wilen, C.; Orchard, R.; Virgin, H. W.; Listgarten, J.; Root, D. E. Optimized SgRNA Design to Maximize Activity and Minimize Off-Target Effects of CRISPR-Cas9. *Nat Biotechnol* **2016**, *34* (2), 184–191. https://doi.org/10.1038/nbt.3437.

(149) Dobin, A.; Davis, C. A.; Schlesinger, F.; Drenkow, J.; Zaleski, C.; Jha, S.; Batut, P.; Chaisson, M.; Gingeras, T. R. STAR: Ultrafast Universal RNA-Seq Aligner. *Bioinformatics* **2013**, *29* (1), 15–21. https://doi.org/10.1093/bioinformatics/bts635.

(150) Kluin, R. J. C.; Kemper, K.; Kuilman, T.; de Ruiter, J. R.; Iyer, V.; Forment, J. V.; Cornelissen-Steijger, P.; de Rink, I.; ter Brugge, P.; Song, J.-Y.; Klarenbeek, S.; McDermott, U.; Jonkers, J.; Velds, A.; Adams, D. J.; Peeper, D. S.; Krijgsman, O. XenofilteR: Computational Deconvolution of Mouse and Human Reads in Tumor Xenograft Sequence Data. *BMC Bioinformatics* **2018**, *19* (1), 366. https://doi.org/10.1186/s12859-018-2353-5.

(151) Zhou, Y.; Zhou, B.; Pache, L.; Chang, M.; Khodabakhshi, A. H.; Tanaseichuk, O.; Benner, C.; Chanda, S. K. Metascape Provides a Biologist-Oriented Resource

for the Analysis of Systems-Level Datasets. *Nat Commun* **2019**, *10* (1), 1523. https://doi.org/10.1038/s41467-019-09234-6.

(152) Fong, E. L. S.; Harrington, D. A.; Farach-Carson, M. C.; Yu, H. Heralding a New Paradigm in 3D Tumor Modeling. *Biomaterials* **2016**, *108*, 197–213. https://doi.org/10.1016/j.biomaterials.2016.08.052.

(153) Martin, F. T.; Dwyer, R. M.; Kelly, J.; Khan, S.; Murphy, J. M.; Curran, C.; Miller, N.; Hennessy, E.; Dockery, P.; Barry, F. P.; O'Brien, T.; Kerin, M. J. Potential Role of Mesenchymal Stem Cells (MSCs) in the Breast Tumour Microenvironment: Stimulation of Epithelial to Mesenchymal Transition (EMT). *Breast Cancer Res Treat* **2010**, *124* (2), 317–326. https://doi.org/10.1007/s10549-010-0734-1.

(154) Betapudi, V.; Licate, L. S.; Egelhoff, T. T. Distinct Roles of Nonmuscle Myosin II Isoforms in the Regulation of MDA-MB-231 Breast Cancer Cell Spreading and Migration. *Cancer Res* **2006**, *66* (9), 4725–4733. https://doi.org/10.1158/0008-5472.CAN-05-4236.

(155) Love, M. I.; Huber, W.; Anders, S. Moderated Estimation of Fold Change and Dispersion for RNA-Seq Data with DESeq2. *Genome Biol* **2014**, *15* (12), 550. https://doi.org/10.1186/s13059-014-0550-8.

(156) Ashburner, M.; Ball, C. A.; Blake, J. A.; Botstein, D.; Butler, H.; Cherry, J. M.; Davis, A. P.; Dolinski, K.; Dwight, S. S.; Eppig, J. T.; Harris, M. A.; Hill, D. P.; Issel-Tarver, L.; Kasarskis, A.; Lewis, S.; Matese, J. C.; Richardson, J. E.; Ringwald, M.; Rubin, G. M.; Sherlock, G. Gene Ontology: Tool for the Unification of Biology. *Nat Genet* **2000**, *25* (1), 25–29. https://doi.org/10.1038/75556.

(157) The Gene Ontology Consortium. The Gene Ontology Resource: 20 Years and Still GOing Strong. *Nucleic Acids Research* **2019**, *47* (D1), D330–D338. https://doi.org/10.1093/nar/gky1055.

(158) Sanson, K. R.; Hanna, R. E.; Hegde, M.; Donovan, K. F.; Strand, C.; Sullender, M. E.; Vaimberg, E. W.; Goodale, A.; Root, D. E.; Piccioni, F.; Doench, J. G. Optimized Libraries for CRISPR-Cas9 Genetic Screens with Multiple Modalities. *Nat Commun* **2018**, *9* (1), 5416. https://doi.org/10.1038/s41467-018-07901-8.

(159) Li, W.; Xu, H.; Xiao, T.; Cong, L.; Love, M. I.; Zhang, F.; Irizarry, R. A.; Liu, J. S.; Brown, M.; Liu, X. S. MAGeCK Enables Robust Identification of Essential Genes from Genome-Scale CRISPR/Cas9 Knockout Screens. **2014**, 12.

(160) Heppner, G. H.; Miller, B. E. Tumor Heterogeneity: Biological Implications and Therapeutic Consequences. *Cancer Metast Rev* **1983**, *2* (1), 5–23. https://doi.org/10.1007/BF00046903.

(161) Flashner-Abramson, E.; Vasudevan, S.; Adejumobi, I. A.; Sonnenblick, A.; Kravchenko-Balasha, N. Decoding Cancer Heterogeneity: Studying Patient-Specific Signaling Signatures towards Personalized Cancer Therapy. *Theranostics* **2019**, *9* (18), 5149–5165. https://doi.org/10.7150/thno.31657.

(162) van 't Veer, L. J.; Bernards, R. Enabling Personalized Cancer Medicine through Analysis of Gene-Expression Patterns. *Nature* **2008**, *452* (7187), 564–570. https://doi.org/10.1038/nature06915.

(163) Aboulkheyr Es, H.; Montazeri, L.; Reza Aref, A.; Vosough, M.; Baharvand, H. Personalized Cancer Medicine: An Organoid Approach. *Trends in Biotechnology* **2018**, *36* (4), 358–371.

(164) Aparicio, S.; Hidalgo, M.; Kung, A. L. Examining the Utility of Patient-Derived Xenograft Mouse Models. *Nat Rev Cancer* **2015**, *15* (5), 311–316. https://doi.org/10.1038/nrc3944.

(165) Shi, J.; Li, Y.; Jia, R.; Fan, X. The Fidelity of Cancer Cells in PDX Models: Characteristics, Mechanism and Clinical Significance. *Int. J. Cancer* **2020**, *146* (8), 2078–2088. https://doi.org/10.1002/ijc.32662.

(166) Namekawa, T.; Ikeda, K.; Horie-Inoue, K.; Inoue, S. Application of Prostate Cancer Models for Preclinical Study: Advantages and Limitations of Cell Lines, Patient-Derived Xenografts, and Three-Dimensional Culture of Patient-Derived Cells. *Cells* **2019**, *8* (1), 74. https://doi.org/10.3390/cells8010074.

(167) Kesselheim, A. S.; Avorn, J. The Most Transformative Drugs of the Past 25 Years: A Survey of Physicians. *Nat Rev Drug Discov* **2013**, *12* (6), 425–431. https://doi.org/10.1038/nrd3977.

(168) Martino, S. D.; Rainone, A.; Troise, A.; Paolo, M. D.; Pugliese, S.; Zappavigna, S.; Grimaldi, A.; Valente, D. OVERVIEW OF FDA-APPROVED ANTI CANCER DRUGS USED FOR TARGETED THERAPY. *Multiple myeloma* 8.

(169) Pei, Y.; Liu, K.-W.; Wang, J.; Garancher, A.; Tao, R.; Esparza, L. A.; Maier, D. L.; Udaka, Y. T.; Murad, N.; Morrissy, S.; Seker-Cin, H.; Brabetz, S.; Qi, L.; Kogiso, M.; Schubert, S.; Olson, J. M.; Cho, Y.-J.; Li, X.-N.; Crawford, J. R.; Levy, M. L.; Kool, M.; Pfister, S. M.; Taylor, M. D.; Wechsler-Reya, R. J. HDAC and PI3K Antagonists Cooperate to Inhibit Growth of MYC- Driven Medulloblastoma. *Cancer Cell* **2016**, *29* (3), 311–323. https://doi.org/10.1016/j.ccell.2016.02.011.

(170) Brabetz, S.; Leary, S. E. S.; Gröbner, S. N.; Nakamoto, M. W.; Şeker-Cin, H.; Girard, E. J.; Cole, B.; Strand, A. D.; Bloom, K. L.; Hovestadt, V.; Mack, N. L.; Pakiam, F.; Schwalm, B.; Korshunov, A.; Balasubramanian, G. P.; Northcott, P. A.; Pedro, K. D.; Dey, J.; Hansen, S.; Ditzler, S.; Lichter, P.; Chavez, L.; Jones,

D. T. W.; Koster, J.; Pfister, S. M.; Kool, M.; Olson, J. M. A Biobank of Patient-Derived Pediatric Brain Tumor Models. *Nat Med* **2018**, *24* (11), 1752–1761. https://doi.org/10.1038/s41591-018-0207-3.

(171) Girard, E.; Ditzler, S.; Lee, D.; Richards, A.; Yagle, K.; Park, J.; Eslamy, H.; Bobilev, D.; Vrignaud, P.; Olson, J. Efficacy of Cabazitaxel in Mouse Models of Pediatric Brain Tumors. *Neuro-Oncology* **2015**, *17* (1), 107–115. https://doi.org/10.1093/neuonc/nou163.

(172) Morfouace, M.; Shelat, A.; Jacus, M.; Freeman, B. B.; Turner, D.; Robinson, S.; Zindy, F.; Wang, Y.-D.; Finkelstein, D.; Ayrault, O.; Bihannic, L.; Puget, S.; Li, X.-N.; Olson, J. M.; Robinson, G. W.; Guy, R. K.; Stewart, C. F.; Gajjar, A.; Roussel, M. F. Pemetrexed and Gemcitabine as Combination Therapy for the Treatment of Group3 Medulloblastoma. *Cancer Cell* **2014**, *25* (4), 516–529. https://doi.org/10.1016/j.ccr.2014.02.009.

(173) Zou, J.; Maeder, M. L.; Mali, P.; Pruett-Miller, S. M.; Thibodeau-Beganny, S.; Chou, B.-K.; Chen, G.; Ye, Z.; Park, I.-H.; Daley, G. Q.; Porteus, M. H.; Joung, J. K.; Cheng, L. Gene Targeting of a Disease-Related Gene in Human Induced Pluripotent Stem and Embryonic Stem Cells. *Cell Stem Cell* **2009**, *5* (1), 97–110. https://doi.org/10.1016/j.stem.2009.05.023.

(174) Liu, X.; Krawczyk, E.; Suprynowicz, F. A.; Palechor-Ceron, N.; Yuan, H.; Dakic, A.; Simic, V.; Zheng, Y.-L.; Sripadhan, P.; Chen, C.; Lu, J.; Hou, T.-W.; Choudhury, S.; Kallakury, B.; Tang, D. G.; Darling, T.; Thangapazham, R.; Timofeeva, O.; Dritschilo, A.; Randell, S. H.; Albanese, C.; Agarwal, S.; Schlegel, R. Conditional Reprogramming and Long-Term Expansion of Normal and Tumor Cells from Human Biospecimens. *Nat Protoc* **2017**, *12* (2), 439–451. https://doi.org/10.1038/nprot.2016.174.

(175) Friedman, H. S.; Burger, P. C.; Bigner, S. H.; Trojanowski, J. Q.; Wikstrand, C. J.; Halperin, E. C.; Bigner, D. D. Establishment and Characterization of the Human Medulloblastoma Cell Line and Transplantable Xenograft D283 Med. *Journal of Neuropathology & Experimental Neurology* **1985**, *44* (6), 592–605.

(176) Jacobsen, P. F.; Jenkyn, D. J.; Papadimitriou, J. M. Establishment of a Human Medulloblastoma Cell Line and Its Heterotransplantation into Nude Mice. *Journal of Neuropathology & Experimental Neurology* **1985**, *44* (5), 472–485.

(177) McAllister, R. M.; Isaacs, H.; Rongey, R.; Peer, M.; Au, W.; Soukup, S. W.; Gardner, M. B. Establishment of a Human Medulloblastoma Cell Line. *International Journal of Cancer* **1977**, *20* (2), 206–212.

(178) Northcott, P. A.; Dubuc, A. M.; Pfister, S.; Taylor, M. D. Molecular Subgroups of Medulloblastoma. *Expert Review of Neurotherapeutics* **2012**, *12* (7), 871–884. https://doi.org/10.1586/ern.12.66.

(179) Menyhárt, O.; Giangaspero, F.; Győrffy, B. Molecular Markers and Potential Therapeutic Targets in Non-WNT/Non-SHH (Group 3 and Group 4) Medulloblastomas. *J Hematol Oncol* **2019**, *12* (1), 29. https://doi.org/10.1186/s13045-019-0712-y.

(180) Pawlowski, J.; Kraft, A. S. Bax-Induced Apoptotic Cell Death. *Proceedings of the National Academy of Sciences* **2000**, *97* (2), 529–531. https://doi.org/10.1073/pnas.97.2.529.

(181) Sheikh, M. S.; Hollander, M. C.; Fornace, A. J. Role of Gadd45 in Apoptosis. *Biochemical Pharmacology* **2000**, *59* (1), 43–45. https://doi.org/10.1016/S0006-2952(99)00291-9.

(182) Chi, Q.; Xu, H.; Song, D.; Wang, Z.; Wang, Z.; Ma, G. α-E-Catenin (CTNNA1) Inhibits Cell Proliferation, Invasion and EMT of Bladder Cancer. *CMAR* **2020**, *Volume 12*, 12747–12758. https://doi.org/10.2147/CMAR.S259269.

(183) Bai, R.-Y.; Staedtke, V.; Rudin, C. M.; Bunz, F.; Riggins, G. J. Effective Treatment of Diverse Medulloblastoma Models with Mebendazole and Its Impact on Tumor Angiogenesis. *Neuro-Oncology* **2015**, *17* (4), 545–554. https://doi.org/10.1093/neuonc/nou234.

(184) Cook Sangar, M. L.; Genovesi, L. A.; Nakamoto, M. W.; Davis, M. J.; Knobluagh, S. E.; Ji, P.; Millar, A.; Wainwright, B. J.; Olson, J. M. Inhibition of CDK4/6 by Palbociclib Significantly Extends Survival in Medulloblastoma Patient-Derived Xenograft Mouse Models. *Clin Cancer Res* **2017**, *23* (19), 5802–5813. https://doi.org/10.1158/1078-0432.CCR-16-2943.

(185) Buonamici, S.; Williams, J.; Morrissey, M.; Wang, A.; Guo, R.; Vattay, A.; Hsiao, K.; Yuan, J.; Green, J.; Ospina, B.; Yu, Q.; Ostrom, L.; Fordjour, P.; Anderson, D. L.; Monahan, J. E.; Kelleher, J. F.; Peukert, S.; Pan, S.; Wu, X.; Maira, S.-M.; Garcia-Echeverria, C.; Briggs, K. J.; Watkins, D. N.; Yao, Y. -m.; Lengauer, C.; Warmuth, M.; Sellers, W. R.; Dorsch, M. Interfering with Resistance to Smoothened Antagonists by Inhibition of the PI3K Pathway in Medulloblastoma. *Science Translational Medicine* **2010**, *2* (51), 51ra70-51ra70. https://doi.org/10.1126/scitranslmed.3001599.

(186) Hashimoto, Y.; Penas-Prado, M.; Zhou, S.; Wei, J.; Khatua, S.; Hodges, T. R.; Sanai, N.; Xiu, J.; Gatalica, Z.; Kim, L.; Kesari, S.; Rao, G.; Spetzler, D.; Heimberger, A. Rethinking Medulloblastoma from a Targeted Therapeutics

Perspective. *J Neurooncol* **2018**, *139* (3), 713–720. https://doi.org/10.1007/s11060-018-2917-2.

(187) Stevens, L. The Biology of Teratomas Including Evidence Indicating Their Origin from Primordial Germ Cells. *Annee Biol.* **1962**, *1*, 585–610.

(188) Stevens, L. The Biology of Teratomas. *Advanced Morphology* **1967**, *6*, 1–31.

(189) Cunningham, J. J.; Ulbright, T. M.; Pera, M. F.; Looijenga, L. H. J. Lessons from Human Teratomas to Guide Development of Safe Stem Cell Therapies. *Nat Biotechnol* **2012**, *30* (9), 849–857. https://doi.org/10.1038/nbt.2329.

(190) Fong, C.-Y.; Gauthaman, K.; Bongso, A. Teratomas from Pluripotent Stem Cells: A Clinical Hurdle. *J. Cell. Biochem.* **2010**, *111* (4), 769–781. https://doi.org/10.1002/jcb.22775.

(191) Hentze, H.; Soong, P. L.; Wang, S. T.; Phillips, B. W.; Putti, T. C.; Dunn, N. R. Teratoma Formation by Human Embryonic Stem Cells: Evaluation of Essential Parameters for Future Safety Studies. *Stem Cell Research* **2009**, *2* (3), 198–210. https://doi.org/10.1016/j.scr.2009.02.002.

(192) Müller, F.-J.; Goldmann, J.; Löser, P.; Loring, J. F. A Call to Standardize Teratoma Assays Used to Define Human Pluripotent Cell Lines. *Cell Stem Cell* **2010**, *6* (5), 412–414. https://doi.org/10.1016/j.stem.2010.04.009.

(193) Willis, R. The Structure of Teratoma. *Journal of Pathology and Bacteriology* **1935**, *XL* (1).

(194) Willis, R. The Histogenesis of Neural Tissue in Teratomas. *Journal of Pathology and Bacteriology* **1936**, *42*, 411–416.

(195) Wang, X. Stem Cells in Tissues, Organoids, and Cancers. *Cell. Mol. Life Sci.* **2019**, *76* (20), 4043–4070. https://doi.org/10.1007/s00018-019-03199-x.

(196) Liu, G.; David, B. T.; Trawczynski, M.; Fessler, R. G. Advances in Pluripotent Stem Cells: History, Mechanisms, Technologies, and Applications. *Stem Cell Rev and Rep* **2020**, *16* (1), 3–32. https://doi.org/10.1007/s12015-019-09935-x.

(197) Wichterle, H.; Lieberam, I.; Porter, J. A.; Jessell, T. M. Directed Differentiation of Embryonic Stem Cells into Motor Neurons. *Cell* **2002**, *110* (3), 385–397. https://doi.org/10.1016/S0092-8674(02)00835-8.

(198) Spence, J. R.; Mayhew, C. N.; Rankin, S. A.; Kuhar, M. F.; Vallance, J. E.; Tolle, K.; Hoskins, E. E.; Kalinichenko, V. V.; Wells, S. I.; Zorn, A. M.; Shroyer, N. F.; Wells, J. M. Directed Differentiation of Human Pluripotent Stem Cells into

Intestinal Tissue in Vitro. *Nature* **2011**, *470* (7332), 105–109. https://doi.org/10.1038/nature09691.

(199) Watanabe, K.; Kamiya, D.; Nishiyama, A.; Katayama, T.; Nozaki, S.; Kawasaki, H.; Watanabe, Y.; Mizuseki, K.; Sasai, Y. Directed Differentiation of Telencephalic Precursors from Embryonic Stem Cells. *Nat Neurosci* **2005**, *8* (3), 288–296. https://doi.org/10.1038/nn1402.

(200) Cai, J.; Zhao, Y.; Liu, Y.; Ye, F.; Song, Z.; Qin, H.; Meng, S.; Chen, Y.; Zhou, R.; Song, X.; Guo, Y.; Ding, M.; Deng, H. Directed Differentiation of Human Embryonic Stem Cells into Functional Hepatic Cells. *Hepatology* **2007**, *45* (5), 1229–1239. https://doi.org/10.1002/hep.21582.

(201) Oldershaw, R. A.; Baxter, M. A.; Lowe, E. T.; Bates, N.; Grady, L. M.; Soncin, F.; Brison, D. R.; Hardingham, T. E.; Kimber, S. J. Directed Differentiation of Human Embryonic Stem Cells toward Chondrocytes. *Nat Biotechnol* **2010**, *28* (11), 1187–1194. https://doi.org/10.1038/nbt.1683.

(202) Idelson, M.; Alper, R.; Obolensky, A.; Ben-Shushan, E.; Hemo, I.; Yachimovich-Cohen, N.; Khaner, H.; Smith, Y.; Wiser, O.; Gropp, M.; Cohen, M. A.; Even-Ram, S.; Berman-Zaken, Y.; Matzrafi, L.; Rechavi, G.; Banin, E.; Reubinoff, B. Directed Differentiation of Human Embryonic Stem Cells into Functional Retinal Pigment Epithelium Cells. *Cell Stem Cell* **2009**, *5* (4), 396–408. https://doi.org/10.1016/j.stem.2009.07.002.

(203) Antoni, D.; Burckel, H.; Josset, E.; Noel, G. Three-Dimensional Cell Culture: A Breakthrough in Vivo. *IJMS* **2015**, *16* (12), 5517–5527. https://doi.org/10.3390/ijms16035517.

(204) Rossi, G.; Manfrin, A.; Lutolf, M. P. Progress and Potential in Organoid Research. *Nat Rev Genet* **2018**, *19* (11), 671–687. https://doi.org/10.1038/s41576-018-0051-9.

(205) Dutta, D.; Heo, I.; Clevers, H. Disease Modeling in Stem Cell-Derived 3D Organoid Systems. *Trends in Molecular Medicine* **2017**, *23* (5), 393–410. https://doi.org/10.1016/j.molmed.2017.02.007.

(206) Yin, X.; Mead, B. E.; Safaee, H.; Langer, R.; Karp, J. M.; Levy, O. Engineering Stem Cell Organoids. *Cell Stem Cell* **2016**, *18* (1), 25–38. https://doi.org/10.1016/j.stem.2015.12.005.

(207) Eiraku, M.; Takata, N.; Ishibashi, H.; Kawada, M.; Sakakura, E.; Okuda, S.; Sekiguchi, K.; Adachi, T.; Sasai, Y. Self-Organizing Optic-Cup Morphogenesis in Three-Dimensional Culture. *Nature* **2011**, *472* (7341), 51–56. https://doi.org/10.1038/nature09941.

(208) McDonald, D.; Wu, Y.; Dailamy, A.; Tat, J.; Parekh, U.; Zhao, D.; Hu, M.; Tipps, A.; Zhang, K.; Mali, P. Defining the Teratoma as a Model for Multi-Lineage Human Development. *Cell* **2020**, *183* (5), 1402-1419.e18. https://doi.org/10.1016/j.cell.2020.10.018.

(209) Tsou, Y.-H.; Khoneisser, J.; Huang, P.-C.; Xu, X. Hydrogel as a Bioactive Material to Regulate Stem Cell Fate. *Bioactive Materials* **2016**, *1* (1), 39–55. https://doi.org/10.1016/j.bioactmat.2016.05.001.

(210) Bertucci, T. B.; Dai, G. Biomaterial Engineering for Controlling Pluripotent Stem Cell Fate. *Stem Cells International* **2018**, *2018*, 1–12. https://doi.org/10.1155/2018/9068203.

(211) Ruoslahti, E. Brain Extracellular Matrix. *Glycobiology* **1996**, *6* (5), 489–492. https://doi.org/10.1093/glycob/6.5.489.

(212) Ozasa, Y.; Gingery, A.; Amadio, P. C. Muscle-Derived Stem Cell Seeded Fibrin Gel Interposition Produces Greater Tendon Strength and Stiffness than Collagen Gel in Vitro. *J Hand Surg Eur Vol* **2015**, *40* (7), 747–749. https://doi.org/10.1177/1753193414568780.

(213) Litvinov, R. I.; Weisel, J. W. Fibrin Mechanical Properties and Their Structural Origins. *Matrix Biology* **2017**, *60–61*, 110–123. https://doi.org/10.1016/j.matbio.2016.08.003.

(214) Even-Ram, S.; Artym, V.; Yamada, K. M. Matrix Control of Stem Cell Fate. *Cell* **2006**, *126* (4), 645–647. https://doi.org/10.1016/j.cell.2006.08.008.

(215) Engler, A. J.; Sen, S.; Sweeney, H. L.; Discher, D. E. Matrix Elasticity Directs Stem Cell Lineage Specification. *Cell* **2006**, *126* (4), 677–689. https://doi.org/10.1016/j.cell.2006.06.044.

(216) Newman, A. M.; Steen, C. B.; Liu, C. L.; Gentles, A. J.; Chaudhuri, A. A.; Scherer, F.; Khodadoust, M. S.; Esfahani, M. S.; Luca, B. A.; Steiner, D.; Diehn, M.; Alizadeh, A. A. Determining Cell Type Abundance and Expression from Bulk Tissues with Digital Cytometry. *Nat Biotechnol* **2019**, *37* (7), 773–782. https://doi.org/10.1038/s41587-019-0114-2.